Numerical Simulations of Jellyfish Galaxies

Nikolaos Sagias
Institute of Physics and Astronomy
University of Potsdam

A thesis submitted for the degree of
Master of Science
in Asrophysics

February 1, 2023

First reader: Prof. Dr. Christoph Pfrommer

Second reader: Dr. Martin Sparre

University of Potsdam

Leibniz Institute for Astrophysics Potsdam

Statement of originality

I hereby declare that the work presented in this thesis is my own original work conducted at the Leibniz-Institut fur Astrophysik Potsdam. All thoughts taken directly or indirectly from external sources are properly denoted as such.

Copyright © 2022 by Nikolaos Sagias. “The copyright of this thesis rests with the author. No quotations from it should be published without the author’s prior written consent and information derived from it should be acknowledged”.

Abstract

Ram pressure stripping has been proposed as a major environmental-driven evolutionary channel able to disrupt the intrinsic properties of a galaxy. This instance occurs when a gas-rich field galaxy is gravitationally attracted from a galaxy cluster. As the galaxy enters the host potential well, develops a high-velocity orbit as propagates through the inter-cluster medium (ICM). The interface with the ICM would exert significant pressure (i.e ram-pressure) on the gaseous component of the infalling galaxy. If this pressure exceeds the binding force of the galactic disc, the interstellar medium (ISM) will be stripped, resulting in spectacular tail morphologies which give rise to the so-called jellyfish galaxies. Theoretical considerations denote that during the infall the galaxy sweeps up the ambient ICM magnetic field lines, constituting a magnetic layer which eventually is draped over the object. The draping layer exerts magnetic tension able to suppress small-scale Kelvin–Helmholtz instabilities and thus inhibit the mixing of ISM clouds into the ICM. In this thesis, we aim to reproduce the ram pressure stripping case and compare the impact of the magnetic fields on the subsequent evolution. We performed wind tunnel experiments with a constant wind model using the moving-mesh code AREPO, according to the observables of jellyfish galaxy JO206. While the addition of magnetic fields weakly affects the gas stripping rate, we find that drastically changes the morphology and survival scheme of the stripped ISM clouds. In contrast to the hydrodynamic analogue, the MHD tail gas is more prone to fragmentation constituting smaller-scale clouds, which however maintain their intrinsic star-forming morphology. These clouds are accelerated to greater distances, leading to the formation of an elongated, long-lived filamentary tail. We note that the prolonged survival scheme of the stripped clouds and the adopted edge-on orientation results in significant fallback cycles of initially stripped ISM gas.

Zusammenfassung

Ram Pressure Stripping wurde als ein wichtiger umweltbedingter Evolutionsweg vorgeschlagen, der in der Lage ist, die inneren Eigenschaften einer Galaxie zu beeinträchtigen. Dieser Fall tritt auf, wenn eine gasreiche Feldgalaxie von einem Galaxienhaufen gravitativ angezogen wird. Wenn die Galaxie in das Gravitationspotential des Galaxienhaufens eintritt, entwickelt sie eine Hochgeschwindigkeitsbahn, während sie sich durch das Inter-Cluster-Medium (ICM) bewegt. Die Schnittstelle mit dem ICM würde erheblichen Druck (i.e ram-pressure) auf die gasförmige Komponente der einströmenden Galaxie ausüben. Wenn dieser Druck die Bindungskraft der galaktischen Scheibe übersteigt, wird das interstellar medium (ISM) getrennt, was zu spektakulären Gasschweifmorphologien führt, die zu sogenannten Jellyfish-Galaxien führen. Theoretische Schätzungen deuten darauf hin, dass die Galaxie während des Einfalls, die bereits bestehenden ICM-Magnetfeldlinien überstreicht und eine magnetische Schicht bildet, die sich schließlich um das Objekt wickelt. Das draping layer übt eine magnetische Spannung aus, die in der Lage ist, kleine Wirbelbewegungen zu behindern und somit das Einmischen von ISM-Wolken in das ICM zu verhindern. In diesem Projekt zielen wir darauf ab, die ram-pressure-stripping Hypothese zu reproduzieren und die Wirkung von Magnetfeldern auf die nachfolgende Evolution zu vergleichen. Wir haben wind-tunnel-Experimente mit einem stetigen Windmodell unter Verwendung des Moving-Mesh-Codes AREPO gemäß den Observablen der Jellyfish Galaxy JO206 durchgeführt. Während die Hinzufügung von Magnetfeldern die Gas-Stripping-Rate schwach beeinflusst, finden wir eine deutliche Veränderung in der Morphologie und dem Überleben der gestrippten ISM-Wolken. Im Gegensatz zum hydrodynamischen Pendant ist das MHD-Schweifgas anfälliger für Fragmentierung und bildet kleinere Wolken, die jedoch ihre eigene sternbildende Morphologie beibehalten. Diese Wolken werden über längere Strecken

beschleunigt, was zur Bildung eines verlängerten, langlebigen fadenförmigen Schweifs führt. Wir bemerken, dass das verlängerte Überleben der gestrippten Wolken und die angenommene edge-on-Ausrichtung zu signifikanten Fallback-zyklen des ursprünglich entfernten interstellaren Mediums führen.

Acknowledgements

I would like to express my gratitude to the Leibniz Institute for Astrophysics (AIP) for providing the resources and support that made this research possible. I would like to thank Prof. Dr. Christoph Pfrommer for the unique opportunity to be part of the Cosmology department at AIP. Finally, I am very grateful to Dr. Martin Sparre for his scientific insights and guidance throughout this thesis.

List of Figures

1.1 The evolution of the dark matter density field 8

1.2 The mechanisms that regulate the star formation efficiency for different halo mass ranges 12

1.3 Color bimodality of galactic populations 16

1.4 The jellyfish galaxy ESO 137-001 26

2.1 Sketch showing the geometry of the flux calculation 34

2.2 The surface gas density of the model isolated galaxy 39

2.3 The surface gas density after unification with the linear background density . . . 42

3.1 Projected slices of the $x - y$ midplane showing the gas structure for the MHD simulation 50

3.2 Same quantities as 3.1 but now showing the HD simulation 52

3.3 The gas density–temperature phase diagram and the differential gas mass contents 55

3.4 The evolution of ISM gas and stellar mass during the simulation 57

3.5 The evolution of the stripping radius and stellar half-mass radius 59

3.6 The mass density, temperature and thermal pressure of gas for all the simulation particles within a cylinder of radius $r = 30$ kpc oriented along the wind direction 61

3.7 The enclosed ISM mass below the stellar disc and the tail 62

3.8 The star formation rate as a function of time 64

3.9 The evolutionary path of the three simulation runs through the evolution of sSFR 65

3.10 The gas magnetic field B_x and B_y projected on the $x - y$ midplace 69

3.11 The Kennicutt-Schmidt phase diagram for the jellyfish galaxy at 1.3 Gyr 71

3.12 The surface density of SFR for a time range from 1.0 to 1.3 Gyr 73
3.13 The correlation for the number of FoF groups and the mean mass of each group for different values of *linking length*. 76
3.14 The morphology of the stipped ISM clouds in the tail 77
3.15 An analogue of 3.14 for ISM clouds that are not bound to the potential of the galaxy 79

A.1 The star formation rate as a function of resolution for the MHD run 105
A.2 FoF analysis for linking length $\ell_{\text{link}} = 0.6$ 106
A.3 FoF analysis for linking length $\ell_{\text{link}} = 2.0$ 107

List of Tables

2.1 The used initial conditions employed for the simulation of the isolated galaxy . . 40
2.2 The ICM properties that we apply on the wind tunnel setup 42

Contents

1 Introduction **1**

1.1 Cosmological framework for galaxy formation 3

1.1.1 Structure Formation 6

1.2 Galaxy evolution 9

1.2.1 Feedback 11

1.2.2 Structure of galaxies 13

1.2.3 Galaxy Population Bimodality 15

1.2.4 Internal and External quenching 17

1.2.5 Enviromental quenching in galaxy clusters 20

1.3 Jellyfish Galaxies 24

2 Methodology **29**

2.1 Numerical Aspects 29

2.1.1 AREPO 32

2.1.2 Modelling ISM 35

2.2 Simulations 38

2.2.1 Initial Conditions 38

2.2.2 Galaxy in wind tunnel setup 41

3 Analysis **46**

3.1 Evolution of the jellyfish galaxy 46

3.2 The impact of ram pressure stripping on the galaxy 54

3.2.1 Galaxy Properties 54

3.2.2 Stripping radius 58
3.2.3 Star formation rate 63
3.3 Tail evolution 67
3.3.1 Magnetic fields 67
3.3.2 Surface density 70
3.3.3 Tail clumps morphology 75

4 Discussion 82

5 Conclusions 87

References 90

A Appendix Chapter 105

A.1 Resolution test 105
A.2 Supplamentary FoF 106

Chapter 1

Introduction

Structures in the universe emerge through the amplification of the primordial density waves. The constructive interference of those that overcome the Jeans length first formed small dark matter haloes, which collapsed into larger haloes over time, under the hierarchical clustering framework. The initially uniform distributed baryons ”slipped” into the dominating dark matter potential wells, radiatively cooled and fell towards the centre of the halo’s potential settling a rotationally supported disc, which eventually further condensed and formed stars. Throughout this accumulative process, large-scale haloes continue to merge dragging over their baryonic content, forming the so-called *cosmic web*. At the knots of the web, we observe the largest and most massive gravitationally bound structures, the galaxy clusters.

Galaxies either part of clusters or in the ”field” reveal rich variety, implying an also dynamic evolution. The main feature that regulates the fate of galaxies is the gas reservoir and the subsequent star formation rate (SFR). Any source able to disrupt the gas content could result in a starburst or quenching event. In general, it is well observed that galaxies follow morphological-color bimodality. The *main sequence* which constituted by blue star-forming spiral galaxies and the *red sequence*, where higher mass quenched ellipticals are located. While, the transition area between these populations (i.e, the green valley) is considered the region, where galaxies have to cross as they evolve (Schawinski et al., 2014). The responsible mechanisms able to trigger such an event are subdivided into two broad categories (Peng et al., 2010): the internal mechanisms which halt star formation based on self-regulating feedback processes and environmental quenching.

A representative case of environmental quenching is the Jellyfish galaxies. Such galaxies emerge when a satellite galaxy is acquired from the potential wells of a galaxy cluster. Since the galaxy develops a high-velocity eccentric orbit through the ICM, significant ram pressure is exerted on the galactic disc. The equilibrium between the ram pressure and force per unit area defines the truncation radius, where every ISM gas located outside of it, is stripped in the wake of the galaxy. Observations suggest that the stripped process could result in long multi-phase gas tails, extending up to more than 100 kpc from the disc (Jaffé et al., 2015; Cramer et al., 2019). The tail's multi-wavelength emissivity (CO, UV, Hα) denote an evolutionary sequence of star-forming regions stripped gas, implying in-situ star-forming events within stripped clouds (Poggianti et al., 2019a,Poggianti et al., 2019b and references therein). Furthermore, radio observations (Müller et al., 2021a; Ignesti et al., 2022) revealed a steep spectral index and high fractional polarisation in the tail, indicating an aligned large-scale magnetic field along the length of the tail in the stripping direction. This morphology is attributed to the *draping effect* (Dursi and Pfrommer, 2008). In particular, during the infall the galaxy sweeps up the ambient ICM magnetic field lines, constituting a magnetic layer which eventually is draped over the object. The associated magnetic field tension can have the power to suppress small-scale modes of the Kelvin–Helmholtz instability, permitting the stripped ISM clouds to survive during the entrainment.

The structure of this is organised as follows. In section 1 we discuss the cosmological framework of galaxy formation and what are the main aspects of galactic formation and evolution. In section 2, we introduce the employed numerical code AREPO and why is suitable for our experiments, the subgrid recipe used to model the ISM, the adopted initial conditions and how we establish the wind tunnel runs. In section 3, we present our simulation results and the analysis. We discuss our results and suggest possible future extensions in section 4. Finally, we summarise our main conclusions in section 5.

1.1 Cosmological framework for galaxy formation

Cosmology provides the framework within which the Cosmos can be described, including all the underlying structures, and consists of our current perception of how the Universe began and evolved to its present state. Modern science has widely accepted the so-called Lambda Cold Dark Matter model, which is able to describe the cosmos by reproducing observations and estimating cosmological parameters with a remarkable accuracy (Komatsu et al., 2011). The whole structure of the ΛCDM model is founded upon two assumptions:
The Universe is *Homogeneous* and *Isotropic* on large scales (the Cosmological Principle) and *Einstein's theory of General Relativity*, which describe the Universe as the structure of space-time that is determined by its mass and energy content.

The Cosmological Principle emerged from the combination of the *Copernican Principle*, i.e. our position in the Universe is not unique, and the observed isotropy. In particular, observations of the Cosmic Microwave Background (CMB) have shown remarkable isotropy, when the dipole component (relative motion of the Local Group relative to CMB) and the contribution of the galactic plane were subtracted (Planck Collaboration et al., 2014). This strong evidence of an isotropic Universe with the Copernican Principle could imply homogeneity as well. However, galaxies tend to be clustered in structures on scales of a few Mpc, with high-velocity random motions. So, the search for homogeneity should be focused on higher scales, where the random velocities seem homogeneous. Large volume surveys that aim to create three dimension maps of the Universe like SDSS showed that the scale of the homogeneity is reached for scales greater than 70 $\mathrm{Mpc\,h^{-1}}$ (Sarkar et al., 2009).

The *Cosmological Principle* provides a direct symmetry of Universe geometry. Hence, including it into Einstein's field equations can reveal the nature of the ΛCDM Universe. More specifically, the Cosmological Principle implies a simpler tensor form of the space-time geometry that leads to the Robertson-Walker (RW) metric. This can be used to determine cosmological distances into different Universe curvatures. Feeding this metric together with the energy-momentum tensor into the Einstein field equation results in Friedmann equations (Friedmann, 1922), which gives the evolution of the scale factor of the universe over time. It is usually written as:

$$\left(\frac{\dot{a}}{a}\right)^3 = H^2(a) = \Omega_{r,0}a^{-4} + \Omega_{m,0}a^{-3} + \Omega_{k,0}a^{-2} + \Omega_{\Lambda,0}$$

Here, $H(a)$ stands for the Hubble parameter (Hubble and Humason, 1931). Observations on clusters or groups of nebulae reveal a linear correlation between velocity and distance, implying the vast majority of the observational targets are redshifted. This can be attributed to an expanding space-time, where farther astronomical objects move away from us faster than the closer ones. Hubble's finding consists of the first cosmological observation, which directly implies that the primitive less expanded Universe originated from a single starting point, i.e the Big Bang. This led to the idea of an extremely hot and dense initial state, the *Hot Big Bang* (Gamow, 1946), which explains the formation of the light elements in the universe and the existence of CMB as later confirmed (Penzias and Wilson, 1965). The dimensionless quantity $\Omega_i \equiv \rho_i/\rho_c$ is the cosmic density parameter, where i denotes different energy components (radiation, matter, curvature and dark energy in respect). The subscript 0 stands for the present time values and the critical density ρ_c is defined as the amount of mass needed to halt the expansion of a matter-only Universe at some infinitely distant time in the future.

Further cosmological observations, in particular of the cosmic microwave background radiation and the luminosity distances of Type Ia supernovae, showed that the Universe is geometrically flat and is composed of four energy density components (Riess et al., 1998). Firstly, the *radiation* component Ω_r, which accounts for a tiny portion of today's energy density budget (order of 10^{-5}) and corresponds to the CMB with temperature $T = 2.73$ K. The matter Ω_m, which is further divided into *baryonic matter* and *non-baryonic matter* and accounts for only about $\sim 30\%$ of its total energy density. *Non-baryonic matter* or Dark matter constitutes the larger fraction $\sim 83\%$ of the matter. The rest fraction and the higher amount ($\sim 70\%$) of the Universe energy budget is called *dark energy* and can be identified with Einstein's cosmological constant Λ (Spergel et al., 2007; Planck Collaboration, 2020). As the Friedmann equations indicate, all the components are correlated with the scale factor, which means that there is a chronicle separation in the Universe epochs. However, the cosmological constant Λ seems independent of it. Thus, the expected constant energy density together with the expansion of the Universe reveals a type of energy density within the cosmos, the *dark energy.*

While *baryonic matter*, which consists of the normal atomic and nuclear matter that make up stars, gas, and heavy elements, is well studied. The definition of *Cold Dark Matter* resonates strange, although its role in the cosmic structure formation has been delimited up to a point. Notably, $\Omega_{\rm dm}$ whose origin is unknown and which is called “cold” because behaves non-relativistically corresponding to a pressureless fluid and is called “dark matter” because it does not couple to light but only to gravity. That it was perceived at the beginning of the 20th century, when observations showed a mass excess, unlike the known theory. More specifically, Zwicky, 1937 study and compare the velocity dispersion of galaxies in the Coma cluster with the virial theorem, showing that it required a much higher fraction of mass than the inferred from stars. Furthermore, the internal dynamics of galaxies reveal a discrepancy in the rotational curves for close galaxies and Milky Way (Rubin and Ford, 1970). The unexpected flattering feature at large radii of the galactic disc, which does not correspond to the distribution of stars and gas, can be only explained by the presence of a significant amount of non-luminous matter. Even for larger scales, the gravitational lensing method, which is very sensitive to the total gravitational mass, on Bullet Cluster (Clowe et al., 2006) stands as one of the strongest evidence. The particle nature of dark matter is a very active research field and various candidates have been proposed, among them WIMPs, superWIMPs, light gravitinos, sterile neutrinos, and axions (Feng, 2010), but their analysis is out of scope, and thus we will account only for the gravitational effects and its contribution in the structure formation. Therefore, Cold Dark Matter-CDM is considered to be *dissipationless* (does not radiate photons as it cools) and *collisionless* (dark matter particles interact weakly only through gravity) (Blumenthal et al., 1984).

The evidence of dark energy was obtained with indirect methods as well. It is already mentioned that the Universe is nearly flat, implying the mean energy density must be close to ρ_c. Studies on the kinematics of galaxies and of large-scale structures in the Universe give energy density around ~ 0.3 (Efstathiou et al., 1990), which is consistent with the CMB measurements for $\Omega_{m,0}$. This sets the ground for a homogenous component that currently dominates the energy budget of the universe, but does not follow the structure of baryonic and dark matter. The establishment of the idea is based on the observed redshift of high redshift Type Ia supernovae (SNIa) that were used as ”standard candles”, due to their standard luminosity peak profile, to test the expansion history of the Universe (Riess et al., 1998). The measured distances from SNIa were significantly larger than a non-Λ Universe, instituting the accelerating expansion of the Universe. The constant energy density Λ through cosmic time makes its contribution to the early Universe negligible and appears as the dominant energy density at later times. It is characterized by negative pressure $P = -\rho_\Lambda c^2$, has the feature of exerting repulsive gravitational forces and thus accelerates the expansion of the universe (Carroll, 2001).

1.1.1 Structure Formation

The expansion of the Universe is accompanied by cooling. This defines phase transitions [1], as the mean energy density of the Universe decreases. As an initial condition (on Plank scales), it is believed that the Universe underwent a phase of rapid expansion, known as *inflation*. This short phase of exponential growth caused the primordial quantum fluctuations of the early universe to be inflated to macroscopic scales (Liddle and Lyth, 1993), and these would lead to the Gaussian, adiabatic, scale-invariant density perturbations (Zel'dovich, 1970). Subsequently, the theoretical description of such a random gaussian field requires the introduction of power spectrum $P(k) = Ak^n$ as the Fourier transform of the correlation function from the decomposed primordial density perturbations. Indeed, these perturbations can be detected in the CMB as small fluctuations, on the order of 10^{-5}, of the black-body temperature $T_{\rm cmb}$. According to current findings, these temperature anisotropies have revealed an almost scale-invariant perturbation power spectrum with spectral index $n_s \sim 0.965$ (Planck Collaboration, 2020), which is also known as "Harrison-Zel'Dovich" power spectrum.

During the early Universe, the perturbations remain small and thus can be described well by the linear regime. As the Universe expanded, the dark matter decoupled from the thermal heat bath, which allowed the perturbations to be amplified according to $\delta(t) \propto t^a$(in the matter-dominated era), due to the gravitational instability. According to this theory, density enhancements start to accrete surrounding material and amplify further, as pressure forces are not able to counteract the gravitational accretion. The mass of the collapsed structures directly correlated to the scale of the perturbations. When perturbations ($\delta = \frac{\rho - \bar{\rho}}{\rho}$) have grown to $\delta > 1$, their evolution reach the *non-linear* regime of collapse, producing the known *cosmic web* with the filamentary structures and galaxy clusters (Planelles et al., 2015), as Figure 1.1 shows. Hence, the power spectrum for large and small scales is characterized by $P(k) \propto k$ and $P(k) \propto k^{-3}$, because small scales were suppressed during the radiation era. Further, it has been found that small scales show higher amplitude to achieve non-linear mass than large scales, thus causing them to collapse first. Resulting in a "bottom-up" scenario for the structure formation, where low mass structures emerge first (White and Rees, 1978).

---

[1] Such as hadron, lepton epochs and Big Bang nucleosynthesis

Constructive interference of the primordial density waves led to overdensities, which became larger through gravity, while destructive interference created under-density patches. The only condition that has to be fulfilled is the overcome of the Jeans length (Jeans, 1902). Perturbations smaller than this critical length will oscillate and only the larger will grow or decay. The Jeans length naturally depends on the sound speed of the environment. However, for dark matter particles, which behave collisionlessly, the Jeans length is correlated to the velocity dispersion. Therefore, to reproduce the structure formation in the Universe as observed, it is required the velocity of dark matter at decoupling to be non-relativistic, i.e cold (Davis et al., 1985). Other models of hot (HDM) and warm dark matter (WDM) have been proposed (Dodelson and Widrow, 1994; Bode et al., 2001). However, both models predict suppression of structure formation on small scales, as dark matter particles and thus density perturbations remained weak. As a result, only the CDM model predicts the smaller scales structure formation, which will further collapse according to the *hierarchical clustering* and produce the larger scales (Peebles, 1965), as we observe them.

During the *non-linear* regime perturbations decouple from the expansion of the Universe and form gravitationally bound structures known as a *dark matter haloes*. These regions are identified as an approximately stable, near-equilibrium state supported against its own self-gravity by the random motions of its constituent particles, i.e virialised haloes (Gunn and Gott, 1972). The collisionless nature of the collapsed material does not allow the creation of shocks, thus the system undergoes *violent relaxation*. Under the manner of the hieratical growth, haloes become increasingly more massive with time. This can be achieved *smoothly* by accreting mass from their surroundings or *merging* with other smaller haloes (Genel et al., 2010; Wang et al., 2011). More specifically, all resolved mergers contribute 60% (20% comes from major mergers)

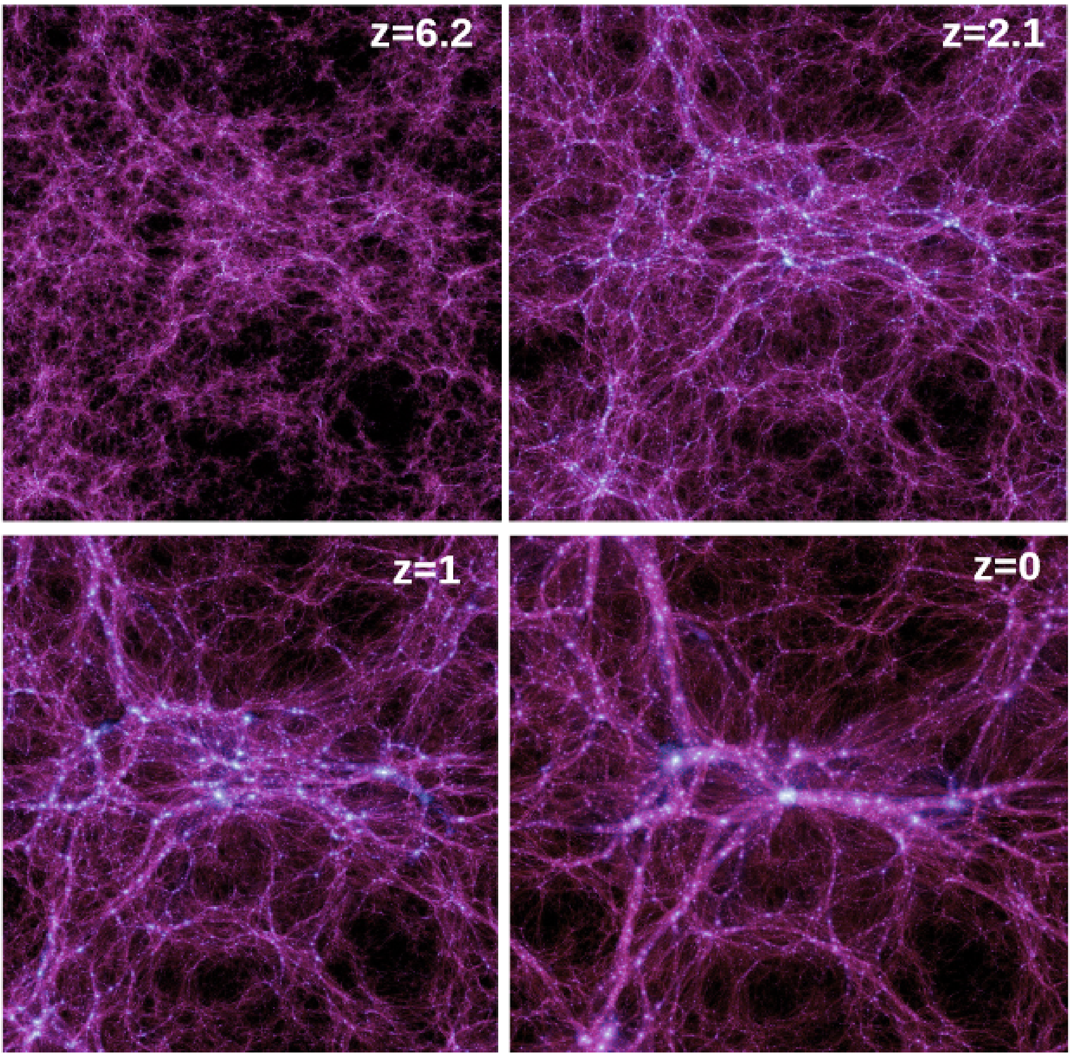

Figure 1.1: Evolution of the dark matter density field in a slab of length L = 100 Mpc h^{-1} and thickness 15 Mpc h^{-1} from the Millennium II simulation (Boylan-Kolchin et al., 2009)

to the total halo mass growth. The rest is 40% of the mass in halos comes from genuinely smooth accretion of dark matter that was never bound in smaller halos. Notably, the haloes grow gradually in the outer part, as only major mergers impact the central regions. As a result, correlations of the survival time of the infalling halos to the merger size showed that haloes are extremely substructured, containing smaller haloes (Moore et al., 1999a), where the rotational energy is acquired due to tidal torques in interactions with the neighbouring systems (White, 1984).

It has been set clear, that the study of non-linear evolution has to be tracked numerically. Physically-based models of galaxy formation relying on N-body simulations were developed, to explain and visualise cosmological content by solving the relative differential equations. These models display the cosmic web morphology including voids, filaments and galaxy clusters as Figure 1.1 (Navarro et al., 1996; V. Springel et al., 2005b; Klypin et al., 2011) in agreement to observations (Colless et al., 2001). These types of simulations consist of dark matter particles that obey the physics that describe above. Baryons follow the flow of the gravitationally dominating dark matter and fall into dark matter haloes, and these haloes cluster to the new potential minimum, as gravity demands. The bound baryonic part locked to the potential minimum reveals the galaxies, which respectively evolve.

1.2 Galaxy evolution

Initially, baryons are distributed almost uniformly. They follow the gravitation potential of the mass dominating dark matter. So, it is expected to cluster as dark matter during the early evolution, and later when the non-linear regime emerges to collapse. Subsequently, the evolution of the baryons is associated with shock-heating up to the virial temperature $T_{\text{vir}} = \frac{2\mu m_H}{3k_\beta}\frac{GM_{\text{vir}}}{r_{\text{vir}}}$, the temperature at which a bound system satisfy virial theorem, set by the gravitational potential of the collapsed dark matter halo. Then, the gas radiatively cools (White and Rees, 1978) and falls towards the centre of the halo's potential settling a rotationally supported disc (Fall and Efstathiou, 1980), where eventually it will collapse further to stars.

The nature of the primordial accreted gas would determine the fate of the pre-formed galaxy. The dark matter large-scale filaments settle the primordial gas, which will penetrate massive dark matter halos located at the nodes of this filamentary structure (Bond et al., 1996). This type of accretion can be happened in *hot-mode accretion* and *cold-mode accretion* or partially both. The first case refers to shock-heated gas to the virial temperature before cooling in the central region, meaning a higher cooling timescale, accounting for the most massive galaxies (Rees and J. P. Ostriker, 1977). However, there is a critical halo mass value $\sim 10^{12} M_\odot$ below which no shock can form. This brings cold mode gas to fall in the centre on free-fall timescales, thus forming low mass galaxies (Kereš et al., 2005; Nelson et al., 2013). Indeed, simulations predict these results but reveal a far more multi-phase structure suggesting the co-existence of both infalling channels. More massive haloes at $z > 2$ that are able to support virial shock are also shown to constantly undergo ”cold flow” (Dekel et al., 2009).

The infalling gas penetrates the structure via *Intergalactic Medium* (IGM), the region outside the virial radius. Then, the gas condenses, as it moves towards the central regions at timescales depending on the accretion mode and radiative cool feeding the *Interstellar Medium* (ISM), the gas within the galactic region (Rees and J. P. Ostriker, 1977). The extended spherical shell between IGM and ISM is called *Circumgalactic Medium* (CGM) and consists of gas with various temperatures between $10^4\,\mathrm{K} - 10^7\,\mathrm{K}$, which can cool respectively to the ISM, but in different timescales. The multi-phase structure of CGM set up a complex interaction among the gas, as CGM is associated with positive (infalling gas) and negative (galactic winds) feedbacks, in terms of gas population and subsequently star formation events (Tumlinson et al., 2017; Suresh et al., 2019).

Commonly, observational surveys measure the star formation rate with the surface density of the gas, via the Kennicutt-Schmidt law (Kennicutt, 1998), because as the gas is cooling, structure fragments emerge. The cooling rate per unit volume of gas is described by: $L = n_H^2 \Lambda(T, Z)$, where n_H is the density of hydrogen and $\Lambda(T, Z)$ is the cooling function, which depends on temperature and metallicity (Wiersma et al., 2009). Given this dependence of the cooling rate on these three variables, the cooling processes can be divided into three regimes. Gas with temperature $\gtrsim 10^7\,\mathrm{K}$ is fully ionized and bremsstrahlung free-free emission is the main cooling mechanism. In the temperature range $10^4\,\mathrm{K} < T < 10^6\,\mathrm{K}$ radiative losses are mainly due to collisions between electrons and atoms or ions, therefore can decay to their ground state. However, different atomic species have different excitation energies, which indicates a strong correlation with the metallicity of the gas (Gnat and Sternberg, 2007). For a temperature range below $10^4\,\mathrm{K}$ the gas is almost completely neutral, which suppresses the processes referred above. The only case for cooling in such temperatures is due to heavy metals and molecules.

The star formation efficiency can be quantified by the fraction between the thermal energy of the gas and the energy loss rate, due to cooling, or the so-called *cooling timescale*:

$$t_{\mathrm{cool}} = \frac{\frac{3}{2} n k T}{n_H^2 \Lambda(T, Z)}$$

A direct consequence is that cold-dense gas constitutes the star-forming regions. Connecting this with the previous considerations about the condense of baryonic matter towards the dark matter gravitational potential minimum and the formation of a gaseous disc, the cooling timescale seems to decrease further, as the density increases. Further cooling eventually leads to a dominance of self-gravity and catastrophic collapse. This results in cold-dense clouds, which under the run-away cooling further collapse to higher-density regions leading to the first stars.

In absence of heavy elements, the only cooling way is restricted to the formation of hydrogen molecules (Wise, 2012). Thereby, once fragments of *Giant Molecular Clouds* (GMCs) overcome a high number density threshold, enough to ignite nuclear fusion, the conditions are suitable to formate the first generation of metal-free stars. These Population III.1 stars are considered to be extremely massive ($10^2 < M/M_\odot < 10^3$), equivalently short-lived, ending their evolution as black holes or supernovae (Ohkubo et al., 2009). Population III.2 consists of lower mass stars ($\sim 40 M_\odot$) that evolved right after within the pre-existing UV environment (McKee and Tan, 2008). To date, Population III stars have not been observed, nevertheless, the energy feedback as they complete their stellar cycle is crucial for the enrichment of ISM with heavier metals, which enables sufficient cooling at lower temperatures, configuring the condition for the next generation of stars.

1.2.1 Feedback

The mismatch between the observed galactic stellar mass function or luminosity function and the expected values for CDM haloes, under the assumption that each halo is associated with a specific baryon mass relevant to the luminosity of the galaxy, introduces the need for feedback mechanisms during the galactic evolution. Notably, ΛCDM predicts an overestimate of baryonic mass per halo mass ($M_\star/M_h$), up to the point that most of the present-day gas would have been cooled and formed stars (Somerville and Davé, 2015). However, as the observations reveal the star formation efficiency with respect to M_h is much lower. There is a star formation peak at $M \sim 10^{12} M_\odot$ (Guo et al., 2010), but beyond it dwarfs and typical galaxies quickly deviate. This peak efficiency point stands for the maximum rate for converting baryons to stars, as haloes close to this mass contain the highest proportion of baryons, and seems independent from redshift (Behroozi et al., 2013). Consequently, further suppression of cooling is required

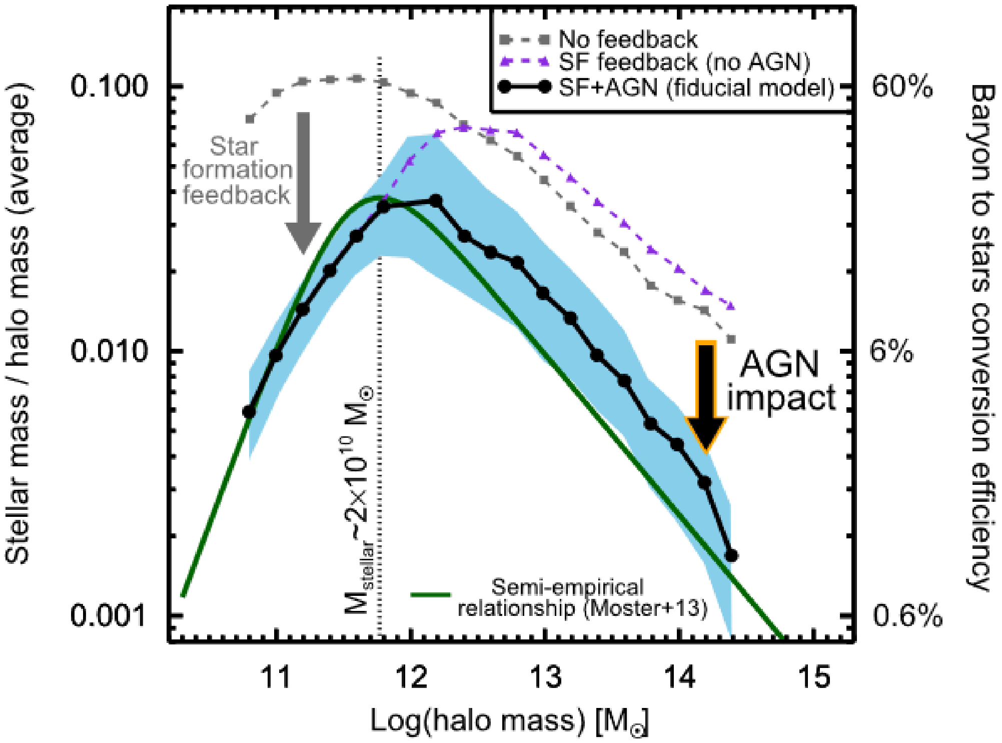

Figure 1.2: The mechanisms that regulate the star formation efficiency for different halo mass ranges. It is illustrated three different simulation runs by (Somerville et al., 2008) and for the semi-empirical model by (Moster et al., 2013). The shaded region shows the 16th and 84th percentiles of the fiducial model that includes energy injection from AGN and star formation. The right y-axis shows the star formation efficiency and the vertical dashed line is the peak point. The figure is from (Harrison, 2017)

for halo masses above and below the peak point, to interpret the excess and adapt the model to observations (Figure 1.2).

For lower stellar mass galaxies, and thus halo mass, feedback from stars and *supernovae* act crucially for the fate of galaxy (Larson, 1974). At the end of stellar evolution, most massive stars undergo violent eruptions channelling their interiors to great distances. Such an event is able to excite the diffuse gas to high temperatures/velocities and even expel significant amounts from galaxy (Hopkins et al., 2012). The galactic wind composed of the warm expelled gas seems irrelevant to the direct star formation efficiency, although the decreasing of the gas reservoir will impact next generation forming rate. The spatial removal of gas and the stellar winds are associated with shock heating of ISM combined with photoionization and radiation pressure, due to radiation of the star during its stellar evolution (Murray et al., 2005), further suppressing the star formation rate.

On the other hand, *supernovae* energetic range seems inefficient to provide the necessary heating rate in larger scale galaxies above $M_{\rm h} \sim 10^{12} M_{\odot}$. As such galaxies are most of the time ellipticals (discussed in 1.2.2), it is expected to include central massive black holes. Indeed, this region suggests a plausible source to quench the galaxy by generating the requisite heating (Silk, 1998; Bower et al., 2006a). This is known as *active galactic nuclei* (AGN) feedback and relies on high-velocity outflows (associated with the initial accretion onto the black hole), which couple with cold ISM gas or even expel it, leading to the star formation regulation of the galaxy and the black hole itself (Croton et al., 2006). Typically, there are two modes of feedback. *Quasar mode*, is relevant with a high accreting fraction of material onto to black hole, close to the Eddington limit[2], and is associated with a large range injection of energy to cold ISM proportional to the infalling gas. The second case called *Radio mode*, is connected with lower accretion rates, which arise radio jets of relativistic particles and lobes heating the surrounding hot halo gas (Fabian, 2012; Heckman and Best, 2014).

1.2.2 Structure of galaxies

Galaxies reveal various intrinsic properties, as the evolutionary processes impact the baryonic component in different magnitudes and timescales. That was first noticed by Hubble, who attempted to classify the galactic systems according to morphological features. The Hubble sequence (Hubble, 1926; Hubble, 1927; Hubble, 1936) separates galaxy population into spirals (early-type), ellipticals (late-type), lenticulars and irregulars. The early-late type notation seems confusing today, because probably the evolutionary track follows the opposite direction, however is maintained for historical reasons. Further subdivision of each galaxy group into sub-types is based on the ellipticity for early-type (from E0 to E7), and the morphology of the disc for late-types, the existence of galactic bar (S & SB) and the wideness of spiral arms (from Sa to Sc). Lenticulars correspond to an intermediate, mixing characteristics of spirals and ellipticals. Galaxies which do not appear specific morphology are classified as irregulars.

Elliptical galaxies present spheroidal stellar distribution with bulge concentrated surface brightness profile, which corresponds to $n = 4$ Sérsic index (Sérsic, 1963) (higher degrees of n for steeper profiles) or equivalently by de Vaucouleurs profile (de Vaucouleurs, 1948). The central concentrated stellar population is comprised of old passively evolving stars, indicating a metal-rich environment. Hence, ellipticals are spectroscopically classified as red, passive high mass systems. The kinematics of stars support anisotropic velocity dispersion around the central region motion and generally *slow rotators*(Cappellari et al., 2011), which is tightly correlated with the photometric properties through the Faber-Jackson relation (Faber and Jackson, 1976). Massive ellipticals generally show low rotational velocity (boxy shape) due to the anisotropy motion, while only lower mass ellipticals present discy shape as they are flattened by their rotation. Their general property of low cold gas content defines them as stable non-star-forming systems. Indeed, the ISM mainly consist hot X-ray emitting gas system inefficient to allow star-forming activities, however individual cold gas regions induced from external sources, kinematically misaligned signatures, are observed (Davis et al., 2011; O'Sullivan et al., 2015).

---

[2] Maximum luminosity an object can achieve, at hydrostatic equilibrium

On the contrary, spiral galaxies display a rotationally supported disc with spiral arms, where stellar populations reside, following a shallower surface brightness profile in the outskirts (de Vaucouleurs, 1956). The galactic disc is composed of a less extended *thin disc*, which is mainly populated by young/blue stars and HII regions, and a *thick disc* of older stars with higher velocity dispersion. Such a structure strengthens scenarios of radial migration of stars from thin to thick disc, as the latter consist of more metal-poor stars originating from lower scale-height areas (Solway et al., 2012). At the centre of these galaxies appear a bulge with surface brightness as ellipticals but less extended, composed of old metal-poor stars similar to the thick disc. It is expected spirals to be bluer and more active in terms of star-forming than ellipticals, as they contain a higher abundance of cold gas. A color gradient is also observed across the radial profile, where the outskirts are bluer than the inner regions (Mihos et al., 2013), suggesting gas encounters from the environment contribute further to the active star-forming profile of spirals. Complementary to the Hubble scheme, late-type spirals (Sc) have a wider opening of arms, more granular morphology, a higher fraction of cold stars and thus bluer, smaller bulge contribution and rotate faster (Cappellari et al., 2011), while statistical approaches indicate that half of them show bar structure (Marinova and Jogee, 2007).

1.2.3 Galaxy Population Bimodality

The morphological bimodality described above is accompanied by color bimodality (Strateva et al., 2001; Baldry et al., 2004), as stellar populations regulate the resulting colors. While massive stars exhibit blue colors and shorter lifespans, reddish stars present smaller masses and more passive profiles as their lifespan is significantly higher. A statistical approach is shown in Figure 1.2, where the colors of a large sample of star-forming galaxies are plotted. Generally, two distinct sequences can be visually identified: the upper *red sequence* where red higher mass galaxies are placed, and the lower mass sequence known as *blue cloud*. The intersection plane between green lines contains a lower number density of galaxies and is referred as *green valley*. The majority of late-type galaxies (spirals and irregulars) with higher star formation rates populate the *blue cloud*, while *red sequence* is mainly dominated by passive early-type galaxies. However, the color bimodality is not strictly morphological driven, as a minority of red-sequence spirals and blue-could ellipticals appear in the sample (less than 10% for both types) (Schawinski et al., 2014). In that sense, *green valley* consists of a superposition of both populations and thus can be assumed as a transition region for the morphological transformation of galaxies between the two sequences (Salim, 2014). Therefore, the color bimodality can be extrapolated as a star formation bimodality, where the *green valley* is the critical region of galaxy evolution.

The star formation bimodality is further studied by applying similar methods. More specifically, by decomposing a large SDSS sample of local galaxies on star formation rate - stellar mass (SFR-$M_\star$) plane, a similar bimodal trend becomes visible as in Figure 1.3 (Noeske et al., 2007; Salim et al., 2007; Renzini and Peng, 2015). A great example can be found at (Renzini and Peng, 2015) in which it is set clear a double peak distribution. The first peak corresponds to active SF galaxies, as it accounts for higher SFRs, and the majority of blue cloud galaxies lie on this plane known as the *main sequence* (MS). The MS evolution for different redshifts reveals that the SFR-$M_\star$ plane follows a similar power-law relation, but exact indexes are hard to determine (Speagle et al., 2014). The second peak, well below the MS, exhibits a lower level of star formation activity and as expected red sequence population is placed there. Such galaxies are defined as “quenched” since they appear about two orders of magnitude less SFRs than MS. Similarly to color diagram, the green valley lies between the red sequence and the blue cloud,

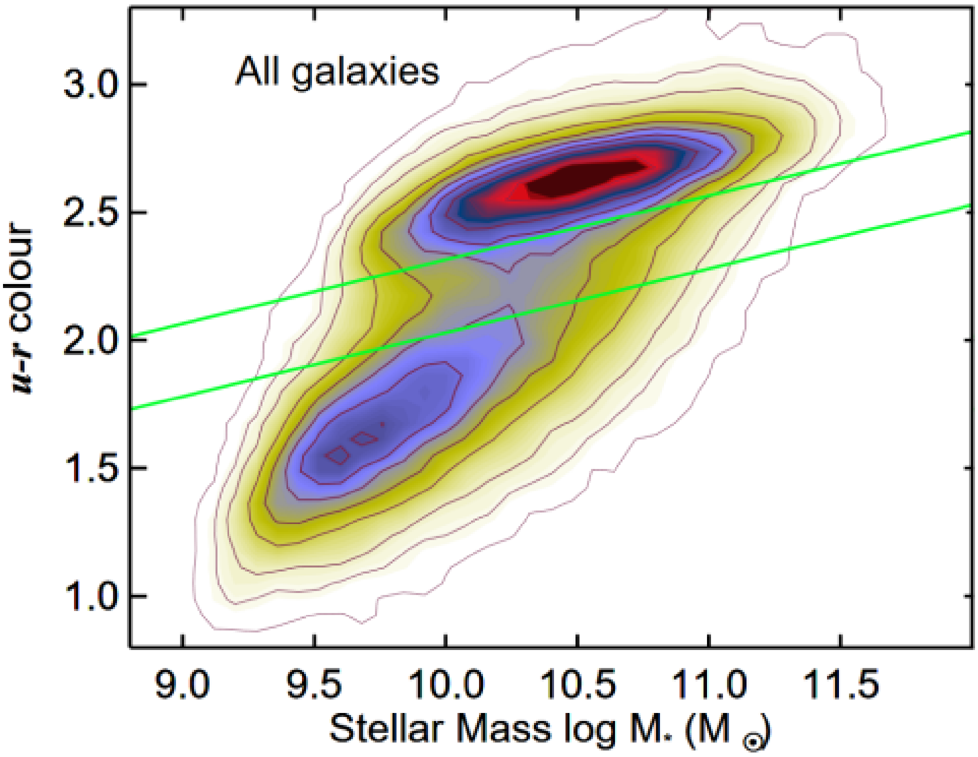

Figure 1.3: The $u-r$ colour-mass diagram on SDSS DR7 (Abazajian et al., 2009) sample of local galaxies ($z < 0.05$). Contours show the linear number density of galaxies. The density diagram indicates three planes: The upper density plane is typically referred to as the red sequence, the lower as the blue cloud, while the transition region between the green lines is referred as the green valley. The figure obtained from (Schawinski et al., 2014)

showing intermediate SFRs.

The green valley seems as the action region, where galaxies have to cross as they evolve. This transition area contains galaxies which have experienced suppression of star formation. Equivalently a "quenching" process, as proposed by Peng et al., 2010, involves the cessation of star formation, as galaxies migrate from the active blue-cloud regime towards the red sequence where SFR is suppressed as to be negligible. Such a process implies that the transformed galaxy will entirely alter its morphological features from late-type (young stellar population) to early-type (older stellar population), which is accepted in hierarchical growth. Generally, the formation of the red sequence can be assumed as the sum of star formation suppressing the process of late-type galaxies and mergers. However, the timescale of such a transition event has to be rapid on the order of $\sim 1\,\text{Gyr}$, otherwise, there would be no bimodality as galaxies would stack at green valley (Martin et al., 2007). On the other hand, quenching tracks do not necessarily follow the late-type to early-type direction, as there is a fraction of green valley galaxies that are not currently quenching, but undergoing a process of *rejuvenation* (see more in 1.2.4 chapter). Generally, several scenarios are presented responsible for the declination of galaxies from the main sequence. Each case acts with a different timescale constituting three quenching timescales regimes, as they pass through the green valley (Schawinski et al., 2014): (i) Late-type galaxies quench rapidly following major mergers $\tau < 1$ Gyr. (ii) Both smooth and disc-like morphologies consist of an intermediate morphology and are characterised by intermediate timescales, which are attributed to minor mergers and galaxy interactions $1 < \tau < 2$ Gyr. (iii) disc-like galaxies quench on slow timescales caused by secular evolution $\tau > 2$ Gyr. The green valley is dominated by very slowly evolving disc-like galaxies along with intermediate and late-type galaxies which pass across it with intermediate timescales within $\tau \sim 1.0 - 1.5$ Gyr (Smethurst et al., 2015).

1.2.4 Internal and External quenching

Quenching is defined as the cessation process of star formation in a galaxy. Such a process can be accomplished in two ways, either by exhausting the cold gas reservoir through the baryon cycle or by the spatial removal of star-forming gas from the galaxy. The quenching mechanisms responsible for that are divided to ***Internal or Mass quenching*** and ***External or Environmental quenching*** (Peng et al., 2010). The first quenching channel is dependent on the galaxy's structure, more specifically on the stellar mass proportion, and it is identified as self-quenching (no strong dependence on the environment). The latter is connected with the surrounding environment and galaxy interactions, mainly correlated to evolutionary tracks of late-type galaxies.

The internal mechanisms can halt star formation without changing the galaxy's environment. In Figure 1.2 is presented the necessity of feedback mechanisms that prevent the cooling of gas and eventually form stars, in low and high halo mass systems. Therefore, AGN Feedback or ***AGN quenching*** is associated with outflows of energetic particles and radiation from the black hole able to heat or expel gas regulating the star formation efficiency and thus matching the high mass end of galaxy luminosity function according to CDM theory. Generally, AGN feedback is possible to quence massive galaxies in various ways: by preventing gas from cooling (Bower et al., 2006b; Croton et al., 2006), halting the cold gas from forming stars via turbulence injection to the galaxy (Alatalo et al., 2015) or even triggering positive star formation event (Ishibashi and Fabian, 2012), which leads to rapid consumption of the available cold gas. Since the black hole is fed by ISM and regulates the cold gas fraction, there would be a co-evolution between the black holes and their host galaxies. This was further investigated by several works, where they reveal tight relation between the bulge mass, stellar mass, the stellar velocity dispersion of the host galaxy and the black hole's mass (Magorrian et al., 1998; Häring and Rix, 2004; Kormendy and Ho, 2013). An indirect hint can be obtained from cosmic star formation history and the black hole growth history, where both follow a similar trend and peak around redshift $z \approx 2$ (Silverman et al., 2008; Madau and Dickinson, 2014). All these results suggest a sensitive balance between the SFR and the morphology of the galaxy that emerged from the central black hole. Subsequently, it is expected a larger AGN activity as a blue cloud galaxy crosses the green valley towards the red-sequence (Schawinski et al., 2010).

However, the increased activity of AGN in the green valley, as a blue cloud galaxy moves away from the main sequence, cannot be attributed as a cause. It has been proposed that the higher AGN activity in these galaxies might be an after-effect (Schawinski et al., 2014), as other quenching mechanisms trigger it by feeding the centre of the galaxy with gas. This indicates alternative mechanisms responsible for the initial quenching event[3]. For example, another Mass quenching mechanism is due to supernovae explosions and stellar winds capable to inject kinetic energy and momentum driving outflows (Figure 1.2). The shallower potential wells of low-mass galaxies imply that the gas is less bound to the system and thus define an important blue cloud quenching process. A supplementary scenario to this has been proposed as the "halo mass quenching" (Kereš et al., 2005; Dekel and Birnboim, 2006), where the infalling cool gas is either cut off or prevented from cooling when the halo mass is above $M_h \sim 10^{12} M_{\odot}$, letting the galaxy with a specific amount of gas reservoir available to form stars according to Kennicutt–Schmidt law (Kennicutt, 1998). This is consistent with the relatively larger quenching timescales, as the depletion of the gas reservoir will continue to form stars for a long time, gradually shifting the galaxy towards to the green valley.

In addition, ***morphological quenching*** can either prevent cold gas from collapsing to stars or increase the pace of consumption of gas. The former can be found in literature as 'gravitational quenching' and describe the case where the large gravitational potential of the bulge stabilizes the gas disc from fragmentation[4] (Martig et al., 2009), given that star formation takes place gravitationally unstable gas discs. The latter is related to galaxies hosting stellar bars (Athanassoula, 1992), which shorten the star-forming timescales by driving gas into the central regions of galaxies, where it can be consumed more quickly (Khoperskov et al., 2018).

---

[3] The disruption of external gas supply to the galaxy and the central cease of consuming gas, resulting in the declination from the galactic main sequence, as SFR steeply decrease

On the other hand, ***merger quenching*** constitutes an important environmental driven evolutionary track. Initial studies on the topic propose that late-type encounters might convert to massive early-type galaxies. Such a scenario involves stellar bridges and tidal tails (Toomre, 1972) able to dissipate the angular momentum and randomise the orbits of stars within a galaxy, modifying the disc morphology into a bulge (Toomre, 1977; L. Hernquist, 1992; Cox et al., 2006). Tidal torques are induced during the merger leading the gas rapidly into the centres of galaxies, resulting in a burst of star formation (starburst), due to the high concentrated gas densities (Mihos and L. Hernquist, 1996). This could effectively quench the post-merger remnant via rapid exhaustion of the gas, suggesting a direct link with the AGN accretion (Di Matteo et al., 2005). Indeed, merger simulations that include starburst with the relevant AGN triggering from black hole growth and the underlying supernova-driven winds (V. Springel et al., 2005a; Hopkins et al., 2008), reproduce red early-type systems in rapid timescales ~ 1 Gyr. The starburst-AGN induced model provides the necessary star formation rate for the morphological change, as it is expected a violent baryon recycle to eventually end up in a red passive stellar population in short timescales.

Nevertheless, this is not a one-way scenario, as major mergers do not necessarily result in an early-type galaxy. Simulations have shown (V. Springel and L. Hernquist, 2005; Robertson et al., 2006), if the progenitor discs are gas-dominated with high enough angular momentum, it could enable the prominent disc to survive. Similarly, a weak interaction between the gas and the AGN activity could potentially lead to recovery of SFR back to post-merger rates (Pontzen et al., 2017). Hence, a post-merger galaxy is possible to have disc morphology if either the disc structure survives or there is a significant amount of gas to reform a disc. Accordingly,

---

[4] i.e its Toomre parameter $Q > 1$

Sparre and V. Springel, 2017 have performed high resolution[5] cosmological simulation for the merging scenario of gas-rich disc galaxies, underlying that a rejuvenation event is quite possible for post-merger remnants with virial mass less than $10^{12} M_{\odot}$. Above, it is mentioned that this order of mass galaxies will experience quenching via various internal mechanisms. This suggests that evolutionary paths can not be described from a single mechanism, as the baryonic matter could undergo an interplay of quenching.

1.2.5 Enviromental quenching in galaxy clusters

Following the hieratical growth model, galaxies tend to be gathered in higher scales structures, as dark matter halos are continuously attracted gravitationally. Those high-density environments are located at the knots of the cosmic web (Figure 1.1) and they are connected to each other with cosmic filaments. Such a galaxy group, namely a galaxy cluster constitute the most massive, virialized structure in the Universe. Typically, they are characterized with mass of $(10^{14} - 10^{15}) M_{\odot}$ and their sizes are approximately a few Mpc (Voit, 2005; C. Pfrommer, 2022). They contain up to several hundreds of galaxies with velocities around 1000 $\mathrm{km\,s^{-1}}$. Within the potential wells reside dilute ($n_e \sim 10^{-3}$ $\mathrm{cm^{-3}}$) and hot ($T \sim 10^7 - 10^8$ K) gas, respectively to the virial temperature (Sarazin, 1986). This X-ray emitting gas assembles the inter-cluster medium (ICM) and contributes around 1/7 of the total mass budget. Whilst, the optically visible baryonic component, i.e the galaxies, accounts only for the $1 - 3\%$ and the rest of mass is attributed to dark matter (Markevitch and Vikhlinin, 2007).

The distribution of galaxies lying in the ICM reveals significant differences in morphology and color than the relative sample of galaxies in the field[6]. Notably, low density field is composed of late-type spirals, while denser cluster regions are mainly populated by early-types (Oemler, 1974). In other words, clusters rich in ellipticals seem centrally condensed, presenting a central cD galaxy[7], in comparison to the spiral-rich clusters that have compositions similar to that of the field. This was further extended by Dressler, 1980 who establish the so-called *morphology-density* relation between the local galaxy density and galaxy type. This expression indicates an increasing early-type fraction with increasing density, i.e towards the cores of massive galaxy clusters, whilst spirals follow the opposite trend. The environmental conditions decisively determine the morphological type of galaxies, implying transitional quenching events. This became clear through the so-called *Butcher-Oemler effect* (Butcher and Oemler, 1978; Butcher and Oemler, 1984), which states that the spirals were more abundant at higher redshifts ($z \sim 0.5$) and the fraction of early-type galaxies is steadily growing, as galaxy clusters evolve to the present time. The observed increment in blue galaxies at higher redshifts is proportionally associated with less abundant (2-3 times) lenticulars (S0), than the present galaxy clusters (Dressler et al., 1997).

---

[5] High mass resolution levels are required to sufficient resolve star-bursting gas (Sparre and V. Springel, 2016)

[6] Referred to the isolated galaxies, which do not share their dark matter halo with another system

[7] cD stands for a giant elliptical galaxy and is identified with the *brightest cluster galaxy* (BCG), which is located at the bottom of the cluster's potential.

Together the properties of the galactic population inside a cluster indicate that galaxies are evolving differently in denser environments. A typical measure to quantify the evolution of galaxies is the SFR. Even spirals in such higher density environments tend to appear redder and present lower SFRs than field late-type galaxies (Kennicutt, 1983), as atomic and molecular gas content appears deficient in clusters (Haynes and Giovanelli, 1984; Catinella et al., 2013). Subsequently, the SFR-density relation reveals an anti-correlation, which becomes even stronger towards the centre of clusters, as massive elliptical systems with old stellar populations are expected to be located there (Gómez et al., 2003; Kauffmann et al., 2004). The star formation transition according to the local properties implies that galaxies undergo a morphological transformation, or equivalently the conversion of blue cloud to the red sequence. The existence of a large number of post-starbursts galaxies (Poggianti et al., 1999) further strengthens this, as they are connected with a high gas consumption rate. Also, the authors attempted to link such events with the progenitors, concluding that there would be two distinctive quenching channels with different timescales. The first one is related to a rapid cessation (order of 1 Gyr), while the other one refers to a slower transformation, concerning the growing population of S0 (Dressler et al., 1997). The above results support environmental driven effects might be superior in the recent epoch ($z \leq 1$), while internal processes governed the galaxy evolution in earlier times (Peng et al., 2010; Jian et al., 2018). However, both quenching channels can be favoured when a galaxy is embedded in a denser environment. As the likelihood of a major merger event increases (Gnedin, 2003; Fakhouri and Ma, 2009), due to the higher number of candidate encounters, it is expected enlargement of internal feedback processes, which in turn explains the higher efficiency of the mass quenching mechanism in denser environments (Martini et al., 2009). Hence, the overall fraction of quenched galaxies seems to increase over the cosmic time (Fang et al., 2018), where more massive galaxies appear an enhanced quenching efficiency until $z \sim 1$ and then remain almost constant, while for lower mass galaxies the mass quenching efficiency continues to the present time (Darvish et al., 2016).

As yet, we have focused on the environmental dependency of galaxies and the emerged properties, but not on the responsible transformation mechanisms. So far, it has been proposed that internal or mass quenching mechanisms are linked with the regulation of higher mass galaxies, whilst external or environmental quenching processes are connected to the lower mass regime. The environmental processes most likely are affecting galaxies that either reside inside a cluster or are going to attach. Such galaxies constitute a higher fraction than the field (Eke et al., 2005). Generally, there are two classes regarding the transformation of galaxies, which would result in the morphology-density and SFR-density relation. The first one is related to gravitational interactions, and all types of tidal interactions, such as galaxy-galaxy, galaxy-cluster, and harassment. While, the second class describes the hydrodynamical interactions between the cold ISM of a gas-rich galaxy and the hot ICM of the cluster (Boselli and Gavazzi, 2006). Unlike the gravitational case, which acts on all galactic components (gas, stars, dark matter), the hydrodynamical interactions mainly affect the galaxy's diffuse ISM in all its phases. Asymmetries in each galactic component are indicating the observational signature for the relevant acting mechanism. However, there are cases that combine gravitational with hydrodynamic mechanisms, such as gas starvation and pre-processing.

Tidal interactions among galaxy-galaxy consist of merger events within the cluster (Merritt, 1983; Byrd and Valtonen, 1990). The induced tidal forces are able to remove matter from the outer parts of the galaxies and drive disc instabilities that funnel gas from the disc towards the centre, thus increasing nuclear activity. A key parameter to perceive how severe the tidal stripping might be is the encounter timescale $t_{\rm enc}$ versus the required time for a tide to rise $t_{\rm tide}$. The $t_{\rm enc}$ is intrinsically correlated with the relative velocity of the encounters. Slow encounters lead to a net transfer of orbital energy to the mutual binding energy, causing the two systems to become bound. While fast encounters do have not enough time to adiabatically adjust, they instead generate tidal shocks able to heat the systems (Mo et al., 2010). Indeed, real clusters are described by high velocity dispersion, which favours fast encounters [8]. The cumulative effect of multiple high-speed galaxy-galaxy is called *harassment* (Moore et al., 1996; Moore et al., 1998). The close flybys interactions will lead the outskirts of the galaxy to a shallow potential well (less bound) or even out of it, due to further encounters and the galaxy-cluster interaction. While the gradual heating of the disc will convert to spheroidal. Hence, harassment is able to alter more effectively diffuse (Sc-Sd) than compact (Sa-Sb) disc galaxies (Moore et al., 1999b). On the other hand, as galaxies orbit the cluster centre, they slowly lose energy and momentum, due to a *dynamical friction* (Chandrasekhar, 1943), sinking them towards the centre of the cluster's potential. This drag force can be interpreted as energy transfer from the galaxy to the background dark matter particles in the wake of the galaxy, and thus is only dependent on the galaxy's mass. This leads to an overdensity of dark matter particles, which eventually will slow down the galaxy. The forthcoming consequence of the high concentration of galaxies in the centre is the growing or feeding of the massive cD galaxy, through merger events. This is known as *galactic cannibalism* (Oemler, 1976; Hausman and J. P. Ostriker, 1978).

The potential wells of galaxy clusters would continuously attract gas or even galaxies from the field. According to morphology-density density, field galaxies most of the time consist of gas-rich discs. When such a galaxy enters the host halo develops a high-velocity eccentric orbit, as it encounters the hot-dense ICM. This is able to trigger *ram-pressure stripping* (Gunn and Gott, 1972), due to permeating of dense ICM by the cold ISM. From the reference system of the galaxy, a sudden wind hot is blowing with velocity V relative to the infalling, which transfers momentum to the disc per unit time as $\sigma_d P_{\mathrm{ram}}$, where the σ_d stands for the disc's cross-section and $P_{\mathrm{ram}} = \rho_{\mathrm{ICM}} V^2$ is the ram-pressure. The high-velocity infall could result in a significant amount of ram-pressure on the galaxy's front. Once the binding force is not able to sustain the galactic morphology against the ram-pressure, the ISM gas will be stripped from the disc. Summarizing, ram-pressure stripping occurs when:

$$\rho_{\mathrm{ICM}} V^2 > 2\pi G \Sigma_\star \Sigma_{\mathrm{ISM}}$$

---

[8] Slow encounters can occur in galaxies that reside in smaller galaxy groups prior to the infall to the cluster, i.e *pre-processing* (Fujita, 2004; Donnari et al., 2021)

where the right hand of the equation stands for the force per unit area $\frac{F_{\rm grav}}{A}$ that binds the disc (Gunn and Gott, 1972; Yamagami and Fujita, 2011). Adopting the relative order of magnitude values, it has been shown that ram-pressure stripping events are frequent within clusters. When the ram-pressure condition is fulfilled, a significant hydrodynamical compression is produced in front of the galaxy, associated with a bow shock, and the formation of large tails as the galactic disc is stripped. However, there is a critical radius value where the ram pressure is taking place due to the time dependency from the eccentric orbit ($\rho_{\rm ICM}$,V) and the continuous decline of the surface densities. Moreover, ram-pressure is closely associated with other hydrodynamical processes such as: *viscous stripping* removal of gas from the outer parts of the galactic disc, due to the viscosity with the ICM (Nulsen, 1982) and *thermal evaporation* of cold ISM gas (Cowie and Songaila, 1977). The quenching efficiency is able to reproduce the Butcher-Oemler effect, as the ISM crucially affected up to a critical radius, converting a disc galaxy to S0 (Quilis et al., 2000). Finally, the cessation of gas infall in the galaxy could be vital for the fate of the SFR. A mild ram-pressure scenario would be able to cut off the external gas accretion, limiting the galaxy to consume its gas reservoir, causing *starvation or strangulation* of the galaxy (Larson et al., 1980; Peng et al., 2015).

1.3 Jellyfish Galaxies

Jellyfish galaxies involve various physical processes, as the exerted ram pressure on the galaxy generates one-sided cometary tails of stripped ISM material. The extended gaseous tail or 'tentacles' of multi-phase gas is associated with the luminous part of the system, the disc, where the outskirts of it are gradually stripped "outside-in". This fact inspired the scientific community to attribute the name of *jellyfish* galaxies (Bekki, 2009; Ebeling et al., 2014). One of the first observational evidence was in HI (Kenney et al., 2004; Chung et al., 2007; Jaffé et al., 2015), where it was noticed that those types of galaxies are HI deficient, as the neutral gas is spatially moved to extraplanar regions. Subsequent narrow-band observations on Hα wavelengths (Yoshida et al., 2002; Yagi et al., 2010; Fossati et al., 2016; Fossati et al., 2018) confirm the existence of ionized gas tails, which extend up to 100 kpc from the parent disc. Moreover, the tail morphology is well-identified across a range of wavelengths for different gas phases. CO observations reveal a less disrupted tail structure compared to Hα, because cold molecular gas is locked in dense molecular clouds located mainly in the inner regions of the stellar disc, and thus more gravitational bound (Vollmer et al., 1999; Jáchym et al., 2017). The detection of the hot gas can be carried out through x-ray observations (Randall et al., 2008; Su et al., 2017), giving insights about the transport processes, such as viscosity and heat conduction, as the cooler galactic front approach the magnetized and high ionized ICM. While radio continuum observations (Murphy et al., 2009; Müller et al., 2021a) provide a direct measure of the intensity and the direction of magnetic fields during a ram-pressure event, as ICM wind sweeping away cosmic-ray electrons, and thus forming synchrotron tails.

The Jellyfish galaxy quenching pathway involves the interplay of several physical processes as the galaxy infalling into the hot ICM, leading to the characteristic tail morphology of the stripped gas. Eventually, after a few Gyrs, the system has stripped a significant proportion of its gas and therefore the initial criterion for stripping cannot be satisfied anymore. By this time, the SFR is almost negligible and thus it can be classified as quenched. This can be assumed as the general picture of how ram-pressure stripping can lead to the excitation of a galaxy from the main sequence. However, the observations (Poggianti et al., 2017a) reveal a plethora of such galaxies, as the interaction scale relies on the intrinsic properties of the cluster and the relevant galaxy prior to the infall. The simulation treatment of the infalling scenario is accomplished with wind-tunnel setup (Tonnesen and Bryan, 2010; Tonnesen and Bryan, 2012; Heß and V. Springel, 2012; Ruszkowski et al., 2014; Steinhauser et al., 2016), in other words, a high-velocity wind with ICM features. Rather than simulating both environments directly and letting the galaxy fall into a massive cluster, is preferred to focus the computational effort on the galaxy and the gas interactions. Thereby, a model galaxy is located within the simulation volume where a continuous gas stream is blown with prescribed features of the ICM, depicting the infalling scheme as one would experience it from the reference system of the galaxy. These types of simulations are able to reproduce essential aspects of the jellyfish galaxies, such as the mass loss and evolution of the star formation rate for different ranges of galaxy masses and inclinations. Furthermore, the observed long tails of dense stripped material into the ICM (Cramer et al., 2019) implies that hydrodynamical effects might support the survival of such structures at large distances from the parent galaxy. Indeed, several authors use MHD simulations (Gronke and

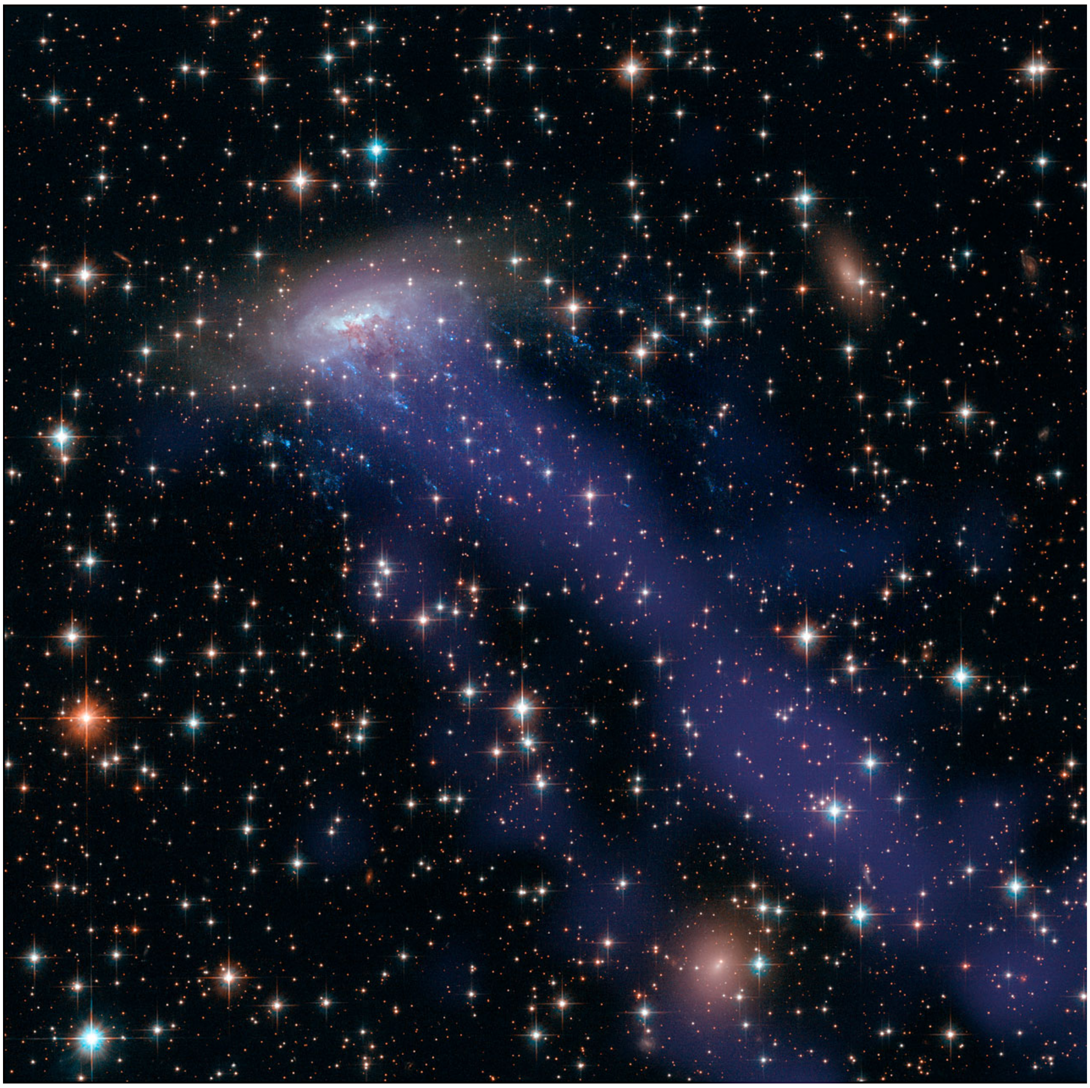

Figure 1.4: The jellyfish galaxy ESO 137-001 as it moves through the galaxy cluster Abell 3627. The image obtained by HST with data for the multi-phase gaseous tail from the Chandra X-ray Observatory. Credits: NASA, ESA, CXC.

Oh, 2018; Li et al., 2020; Sparre et al., 2020), to investigate the interaction of cold clouds in the hot wind. They comment that if the radiative cooling timescale is shorter than the hydrodynamical instabilities timescale, the stripped tail cold material will survive against the Kelvin-Helmholtz instabilities or even grow due to gas accretion from the hot wind. Notably, Sparre et al., 2020 showed the importance of magnetic fields in such simulation setups. The addition of a turbulent magnetic field ICM wind could further suppress the Kelvin-Helmholtz instabilities, due to magnetic draping (Dursi and Pfrommer, 2008) as the magnetic field lines in the wind are wrapped up upstream from the galaxy. This could lead to filamentary density distribution (instead of clumpy) tail morphology, which probably would be associated with a high mass proportion of cold gas. Polarized radio synchrotron observations of the jellyfish galaxy JO206 (Müller et al., 2021a) confirm this evidence, revealing an unexplored scope of such galaxies. In particular, it was shown that the draped magnetic field lines are aligned with the wind direction, suggesting that the cold clouds in the tail might be shielded against small-scale turbulent motions, e.g Kelvin-Helmholtz instabilities.

Chapter 2

Methodology

In this chapter, we discuss the numerical methods used in our simulations 2.1 and the developed wind tunnel setup 2.2 which enables us to reproduce the ram pressure stripping case.

2.1 Numerical Aspects

Observations of individual galaxies have shaped our general impression of the stages of galactic evolution. However, it is not possible to extract a fully structured physical theory, since the evolution of galaxies and especially the jellyfish paradigm can be characterized as highly non-linear. Furthermore, recent studies have proposed that various physical processes, such as magnetic fields, might play a critical role during the galaxy's interaction with the intracluster medium. Numerical simulations could provide a direct evolutionary tracking of such parameters with a direct correlation to the intrinsic properties of the system.

Over the past decades, numerical simulations have proved a valuable tool in modeling and testing various astrophysical concepts on a large range of scales. Accordingly, cosmological simulations are described from large simulation volumes that aim to reproduce the statistical properties of the Universe, initiated from initial conditions obtained from the power spectrum of the initial density perturbations. By contrast, simulations of individual or interacting galaxies can be conducted either using ”zoom-in” techniques, which focus resolution on subvolumes of cosmological simulations, or by building the system directly from an initial equilibrium state.

Generally, numerical simulations discretize the simulation volume into a large number of smaller spatial elements with respect to the underlying physical processes. Each of these elements represents a different type of simulation matter (dark matter, stars, or gas), while its numerical evolution follows the non-linear models. A major concern regarding the ”numerical depth” of the simulation is the so-called *resolution*. It depicts the number of elements on which the system is described and consists of a measure between the accuracy and the computational cost. For example, higher resolution levels aim to resolve small-scale processes, since the underlying discretization elements become smaller. The numerical evolution of a physical process is carried from more pseudo-particles, resulting in a more accurate description. However, the calculations are also increased, and thus the simulation becomes ”computationally expensive”. The optimum selection is hard to achieve, and hence modellers tend to determine resolving power according to their object research.

N-body codes or gravity solvers provide the basis of galaxy simulations, where hydrodynamical treatment or semi-analytical models of baryonic matter will be applied. Gravity establishes the dynamics for dark matter and star particles and subsequently provides the dynamical frame for the gas. Since the first astrophysical simulations attempt to model the dark matter distribution in the Universe, which responds only to the gravitational force, various successful implementations have been developed. Typically, dark matter is treated as a collisionless fluid. In N-body simulations, this fluid is sampled into finite particles of a given mass [1]. Therefore, the final force on each mass particle is calculated by solving Poisson’s equation accounting for the contributions from the rest particles, where a necessary gravitational *softening length* has to be introduced as a minimum separation between particles to avoid numerical artifacts from small-scale gravitational measurements (Plummer, 1911; Price and Monaghan, 2007). A direct sum of the Newtonian potential could provide quite accurate results, however, due to the high computational cost that scales as N^2, several other methods have been developed. Such methods can be particle-based, mesh-based, or hybrid. The former is known as tree codes (Barnes and Hut, 1986) which calculates the contributions of the nearby particles individually and handle the force from distant groups collectively. While the particle-mesh (Hockney and Eastwood, 1988) method manages the particles as a density field, where the gravitational force is approached through a Fourier transform. A hybrid Tree-PM approach is very common in modern simulations like *AREPO* (Springel, 2010). It embodies the advantages of both methods mentioned above, calculating the short-range gravitational force with the tree algorithm whereas the long-range with PM. In general, N-body algorithms seem to work quite precisely for collisionless particles (dark matter and stars), thus the selection criterion is mainly limited to the reduction of the computational cost.

---

[1] A system can be defined as collisionless when its relaxation time exceeds the age of the Universe

On the other hand, the numerical treatment of baryonic matter appears to be a much more challenging task. The interactions between the gas particles occur on much shorter timescales, which leads it to be modeled as an ideal continuum fluid. Its evolution is governed by the hydrodynamical framework along with the relevant gravitational force. To solve the motion of an ideal fluid, one has to consider *Euler equations*:

$$\frac{\partial \rho}{\partial t} + \nabla(\rho \mathbf{v}) = 0 \tag{2.1}$$

$$\frac{\partial}{\partial t}(\rho \mathbf{v}) + \nabla(\rho \mathbf{v}\mathbf{v}^T + P) = 0 \tag{2.2}$$

$$\frac{\partial}{\partial t}(\rho e) + \nabla[(\rho e + P)\mathbf{v}] = 0 \tag{2.3}$$

where the mass, momentum and energy conservation are presented and $e = u + \mathbf{v}^2/2$ stands for the total energy per unit mass. The above set of differential equations can be assumed closed with the addition of the equation of state $P = (\gamma - 1)\rho u$, as a description of pressure in function with the other thermodynamical variables.

As the hydrodynamic equations cannot be solved analytically, numerical codes are needed to compute the evolution of the gaseous component. Fundamentally, there are two approaches to solve numerically the hydrodynamical equations depending on the definition of the computational elements. The ***Eulerian*** methods employ a spatially static mesh in the simulation volume, where the space is discretized onto individual cells at specific positions. Within each cell, the hydrodynamical equations are solved, while the mass is allowed to flow across the cells. This is the essence of Eulerian methods since the demand of the conservation laws (mass, momentum and energy) across the edges of the cells when they exchange content, enables a precise estimate of the fluxes. In ***Lagrangian*** specification, the mass of the fluid is discretized into sampling particles with a total mass equal to that of the whole fluid. This method implies that the system of reference follows the movement of the particles as they are free to move through space and time, while they enclose the fluid's information.

A widely applied Lagrangian formulation is Smoothed Particle Hydrodynamics (SPH) (Gingold and Monaghan, 1977; Monaghan, 1992; V. Springel, 2010). As stated before, mass particles are used as computational elements, where differences between neighbouring points indicate the fluid's properties, using adaptive smoothing kernel techniques. This leads to adaptive spatial resolution following the properties of the fluid (e.g higher resolution at denser regions), as the kernel involves the smoothening length. Furthermore, the direct implementation of the SPH from the fluid Lagrangian equations ensures the conservation of mass, energy, linear momentum, and angular momentum. However, SPH suffers from a weakness in the modelling of shocks and other contact discontinuities, since it relies on an artificial viscosity term (Dolag et al., 2005). Due to this, SPH appears to have difficulty integrating instabilities in fluids (e.g. Kelvin-Helmholtz instability) and gas mixing at boundaries (Agertz et al., 2007). In contrast, Eulerian uniform cartesian mesh methods such as Adaptive Mesh Refinement (AMR) (Teyssier, 2002) allow the mixing of entropy and other properties on the resolution scale without any viscosity term, and hence intrinsically are more efficient at investigating shocks and surface discontinuities. Moreover, AMR codes offer refinement(de-refinement) opportunities of the mesh enabling the splitting(merging) of cells and improving(reducing) the resolution at important(unnecessary) sub-volumes. However, AMR codes suffer from disadvantages such as the lack of Galilean invariance and instances of over-mixing (Scannapieco and Brüggen, 2008).

2.1.1 AREPO

The cosmological MHD code *AREPO* (Springel, 2010; Weinberger et al., 2020) is presented as a hybrid approach of the Lagrangian and Eulerian methods, that is based on an unstructured moving mesh. It combines the advantages of the Eulerian scheme in capturing shocks and contact discontinuities and the natural flexibility along with the Galilei invariance of the SPH approach, providing a unique frame to study astrophysical flows. This is accomplished due to the unique geometry of *AREPO* that is based on an unstructured moving mesh. In fact, it employs a technique known as Voronoi cell tessellation. Initially, it defines a discrete set of mesh-generating points. A Voronoi cell is formed around a generator point adopting the geometry of the cell points which are closest to that generator point, and eventually defines the volume for the hydrodynamics cell. The mesh geometry is changing continuously over time, as the mesh-generating points can be moved arbitrarily. When the cells move with the velocity of a local flow, a quasi-Lagrangian formulation of continuum hydrodynamics is adopted, offering a fully Galilean invariant frame. While, the freedom of movement of the mesh ensures a continuous spatial resolution adjustment with better numerical convergence than Eulerian codes (Pakmor et al., 2016).

AREPO solve the hyperbolic conservation laws of ideal hydrodynamics with a finite-volume approach on the moving Voronoi mesh, based on a second-order unsplit Godunov scheme with an exact Riemann solver. For the standard hydrodynamical (HD) Euler equations, the conserved quantities are mass, momentum, and energy as described before (Eq. 2.1). In the case of MHD, the magnetic field component has to be added. They can be written in compact form by introducing a state vector $\mathbf{U}$ of conserved quantities describing the fluid and an associated flux function as $\mathbf{F}(\mathbf{U})$:

$$\mathbf{U} = \begin{pmatrix} \rho \\ \rho\mathbf{v} \\ \rho e \\ \mathbf{B} \end{pmatrix} \qquad \mathbf{F}(\mathbf{U}) = \begin{pmatrix} \rho\mathbf{v} \\ \rho\mathbf{v}\mathbf{v}^T + p - \mathbf{B}\mathbf{B}^T \\ \rho e\mathbf{v} + p\mathbf{v} - \mathbf{B}(\mathbf{v}\cdot\mathbf{B}) \\ \mathbf{B}\mathbf{v}^T - \mathbf{v}\mathbf{B}^T \end{pmatrix} \tag{2.4}$$

Where the total gas pressure is $p = p_{\text{gas}} + \frac{1}{2}\mathbf{B}$, the total energy per unit mass is $e = u + \frac{1}{2}\mathbf{v} + \frac{1}{2\rho}\mathbf{B^2}$ and u the thermal energy per unit mass. The Euler equation can be also compactly written as:

$$\frac{\partial\mathbf{U}}{\partial t} + \nabla\cdot\mathbf{F} = 0 \tag{2.5}$$

emphasizing the conservation laws over the Voronoi cells. Each cell is characterized by mass m_i, momentum p_i, energy E_i and magnetic field strength B_i. Following the finite-volume approach, the state of the fluid is obtained after integrating over the volume V_i of a cell i, as averages of the conserved quantities,

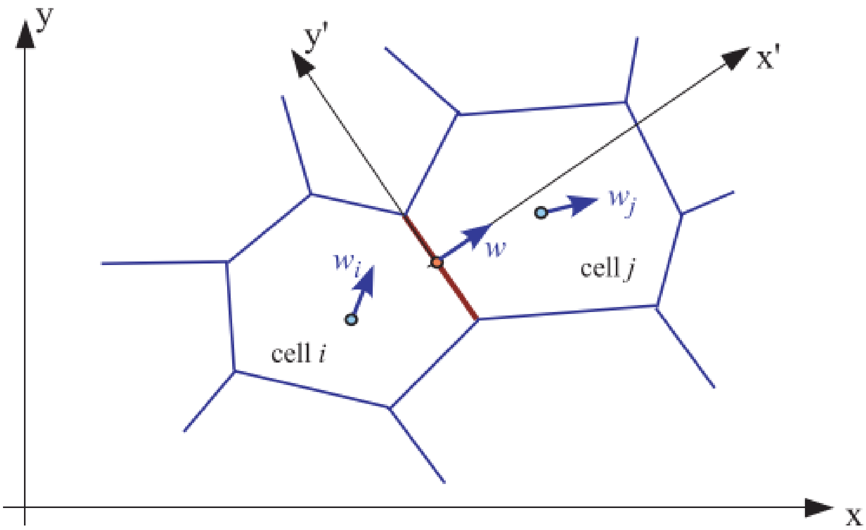

Figure 2.1: Geometry of the flux calculation. An unsplit scheme where the flux across each face is estimated based on a 1D Riemann problem. The fluid state is expressed in a frame which moves with the normal velocity w of the face and is aligned with it. The scheme obtained from (Springel, 2010).

$$Q_i = \int_{V_i} \mathbf{U}\, dV \tag{2.6}$$

where the volume integral can be converted into a surface integral by applying the Gauss theorem:

$$\frac{dQ_i}{dt} = -\int_{V_i} [F(U) - U \otimes w]\, d\mathbf{n} = -\sum_j A_{ij} F_{ij} \tag{2.7}$$

where $\mathbf{n}$ is the outward normal vector of the cell interface and $\mathbf{w}$ is the velocity with which each point of the boundary of the cell moves. Thus, the second term in the integral can be assumed as a movement across the cell boundary due to the mesh motion, and thus has to be subtracted from the flux estimation of each cell since we care only about the relative velocity between Voronoi cells. Finally, adopting the averaged flux across the interface between cells i and j, the relationship can be simplified by introducing A_{ij} as the orientated area of the face between cells i and j. The flux $\mathbf{F}_{ij}$ between the two cells through their common surface is then calculated using the HLLC Riemann solver (Toro, 2009). Given that, the time discretization of (eq 2.7) reveals the time evolution of the fluid through :

$$\mathbf{Q}_i^{(n+1)} = \mathbf{Q}_i^{(n)} - \Delta t \sum_j A_{ij} \hat{\mathbf{F}}_{ij}^{(n+1/2)} \tag{2.8}$$

where $\hat{\mathbf{F}}_{ij}$ stands for the time-averaged approximation to the true flux $\mathbf{F}_{ij}$ across the cell face and the superscript n the time step of the system.

However, a major concern arises during spatial discretisation, as was noticed by Pakmor et al., 2011 how tried to couple the ideal MHD equations on *AREPO*. Generally, the problem in solving the ideal MHD equation is the divergence constraint $\nabla \cdot \mathbf{B} = 0$. While the continuum equations of ideal MHD preserve that in an initially divergence-free field, this is not necessarily the case for discretized versions of the equations. This could eventually lead to large local amplification of the magnetic field and thus unphysical results. To overcome this Pakmor and Springel, 2013 implements the Powell divergence-cleaning approach (Powell et al., 1999). In this scheme, a passive advection term of the flow is added to the Euler equations, counteracting the growth of local $\nabla \cdot \mathbf{B} = 0$ errors. Applying this method to all active cells, the divergence of the magnetic field of an active Voronoi cell is estimated by:

$$\nabla \cdot \mathbf{B}_i = \frac{1}{V_i} \sum_{\text{faces}} \mathbf{B} \cdot \hat{n} \mathbf{A}_\mathbf{i} \tag{2.9}$$

where $\mathbf{B}_{\text{face}}$ is the field strength at the interface between cells, with volume $\mathbf{V}_i$.

2.1.2 Modelling ISM

AREPO provides the backbone for the jellyfish evolution modelling that will be carried out in a wind tunnel experiment. Given this numerical basis, smaller-scale phenomena such as star formation have to be included. However, the spatial(or mass) resolution even in the most modern simulations is larger than the typical scales of the turbulent ISM, where star formation occurs. Therefore sub-grid models have been implemented to describe these baryonic processes. They aim to convert the impact of unresolved physics on scales that are resolved, through the statistical formulation of the ISM with respect to the outcomes of observations.

An effective sub-resolution model able to describe small-scale processes such as star formation and stellar feedback introduced by Springel and Hernquist, 2003. In this model, the computational element ISM is treated as a two-phase medium. Notably, within the gas cells, a hot ambient volume-filling representing the hot phase coexists in pressure equilibrium with the cold phase condensed in clouds. Hence, multiphase gas cells are described by an effective equation of state at densities above the threshold particle density for star formation $\rho_{\rm th} = 0.13{\rm cm}^{-3}$ and become eligible for star formation, whilst below the gas will have cooled down to 10^4K where it becomes neutral.

At densities higher than $\rho_{\rm th}$ the ISM maintains a self-regulated star formation, as various internal processes tend to counterbalance the mass exchange between the two phases. More precisely, the rates at which the mass of the hot and cold phases evolve are given by :

$$\frac{d\rho_{\rm c}}{dt} = -\frac{\rho_{\rm c}}{t_\star} - A\beta\frac{\rho_{\rm c}}{t_\star} + \frac{1-f}{u_h - u_c}\Lambda_{\rm net}(\rho_h, \rho_u) \tag{2.10}$$

$$\frac{d\rho_{\rm h}}{dt} = \beta\frac{\rho_{\rm c}}{t_\star} + A\beta\frac{\rho_{\rm c}}{t_\star} - \frac{1-f}{u_h - u_c}\Lambda_{\rm net}(\rho_h, \rho_u) \tag{2.11}$$

where, $\rho_{\rm c}$ and $\rho_{\rm h}$ indicate the density of the cold and hot phases. The first term in the equation 2.10 denotes that star formation events deplete the reservoir of cold clouds, as star particles are formed according to characteristic timescale $t_\star$. Then, the second term accounts for the evaporation of cold gas due to supernovae, particularly, through thermal conduction. The efficiency A of the evaporation process is a function of the local density and scales as $A \propto \rho^{-4/5}$ (McKee and Ostriker, 1977). While the parameter β is handle the fraction of massive stars into the ISM and is regulated by the chosen IMF. The last term corresponds to the rate at which hot gas cools through thermal instabilities. The cooling function $\Lambda_{\rm net}$ estimated from the radiative processes, assuming a spatially uniform UV background field (Faucher-Giguère et al., 2009), which is further extended by Vogelsberger et al., 2013. The mass exchange regime is denoted by the appearance of the second and third terms in both equations, but with opposite signs. Radiative energy losses by the hot gas will drive a corresponding growth of the clouds at a proportional rate, whilst the evaporation of cold gas will return material from condensed clouds to the ambient gas. The energy feedback is represented by the first term from 2.11, where supernovae instances (SNII) will reheat some of the cold gas, releasing material to the ambient gas.

Star particles are formed stochastically from the reservoir of clouds with a timescale proportional to the local dynamical time $t_\star = t_0^\star \, (\rho/\rho_{th})^{-1/2}$, where the free parameter is calibrated from observational relation as $t_0^\star = 2.27\,\mathrm{Gyr}$, following the Kennicutt-Schmidt law (Kennicutt, 1998). Once the gas density is above the star formation threshold ρ_{th}, the gas cells are governed by equations 2.10 and 2.11 and could potentially lead to collisionless star particles, following a probabilistic description relative to $t_0^\star$. Emerged Stellar particles adopt the properties of the parent gas cell, in particular, position, mass, momentum and metallicity, and represent a single age stellar population (SSP) with a given initial mass function (IMF) from Chabrier, 2003. Throughout the simulation steps, the evolution of the stellar population is expected to inject mass back into the ISM and chemically enrich it through supernovae Ia and II and AGB stars. The mass/metal return is tracked for various elements(H, He, C, N, O, Ne, Mg, Si, Fe), that are distributed to neighbouring cells.

A similar probabilistic frame is also applied for wind particles. Star-forming gas cells may become a site for kinetic feedback from SNII injecting wind particles. They also inherit the properties of the parent gas cells, transferring the mass and metal across the ISM with a velocity proportional to the local one-dimensional dark matter velocity dispersion (Okamoto et al., 2010). In order to ensure the ejection process, the wind particles are temporarily decoupled from the hydrodynamical interactions, adopting a collisionless regime until the internal gas density reaches $\rho < 0.05\,\rho_{th}$ or for large travel time. Once one of these criteria is met (the second is rarer for individual galaxy simulations), the wind particles are recoupled, depositing their mass, metal containments, thermal energy and momentum into the nearest gas cells.

2.2 Simulations

In this section, we introduce the initial conditions of the model galaxies and the numerical recipe to perform a wind tunnel simulation using AREPO.

2.2.1 Initial Conditions

In order to conduct a numerical MHD of an individual galaxy, it is necessary to define the initial conditions. This work aims to reproduce a well-studied instance of ram-pressure stripping, namely the case of JO206 (Müller et al., 2021a), where its observationally determined mass will be used to construct a disc galaxy in equilibrium. To set up a compound galaxy that will later evolve either in isolation or under the influence of ram pressure, it has been used the *MakeNewDisk* software (Springel et al., 2005) which is based on prior work described in Springel and White, 1999.

The galaxy model is based on the design of dark matter halo and stellar discs in dynamical equilibrium through an approximate solution of the Jeans equations. The dark matter distribution is modelled with a Hernquist, 1990 profile truncated for radii larger than R_{200} :

$$\begin{aligned} \rho_{\mathrm{DM}}(r) &\propto \frac{1}{2\pi}\frac{\alpha}{r(r+\alpha)^3}, \qquad && \text{for } r < R_{200} \\ \rho_{\mathrm{DM}} &\to 0 && \text{for } r > R_{200} \end{aligned} \tag{2.12}$$

where α is the scale factor. Following the formulation of Springel et al., 2005, α can be estimated by demanding a corresponding NFW profile (Navarro et al., 1997) with the same dark matter, to present the identical inner density profile. In our work, we truncate the dark matter density profile for radii larger than the R_{200} ensuring that the enclosed density within R_{200} is consistent with the critical density of the Universe. Thereby, it is possible to relate a to the concentration index $c = \frac{r_{200}}{r_s}$, where r_s is the relevant scale radius of the NFW profile by

$$\alpha = \frac{r_{200}}{c}\sqrt{2[\ln(1+c) - c/(1+c)]} \tag{2.13}$$

Given that, we choose a virial velocity of $V_{200} = 178\,\mathrm{km\,s^{-1}}$, yielding a total mass of $M_{\mathrm{total}} = V_{200}^3/(10GH_0) = 2\times10^{12}\mathrm{M}_\odot$ for the system, according to the galaxy J0206 that we persue to

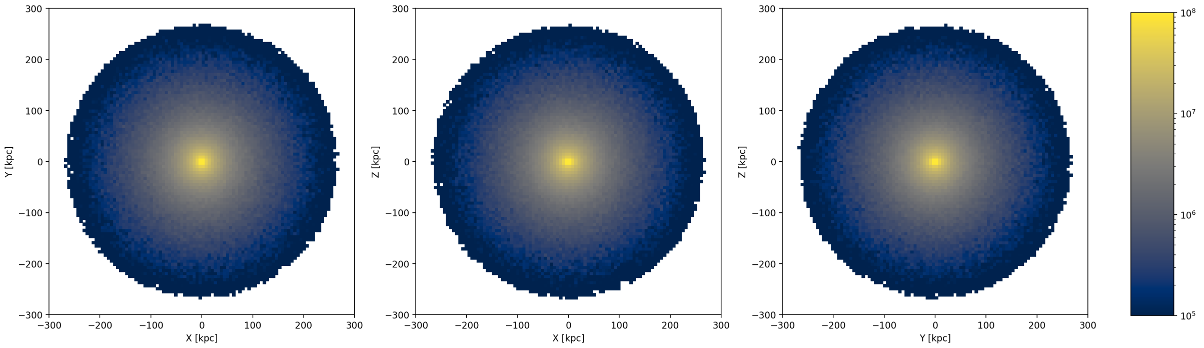

Figure 2.2: The surface gas density as extracted from *MakeNewDisk* in a cubic region of side 600 kpc. At the centre of the box is placed the isolated galaxy, which will provide the initial conditions for the high-resolution simulation runs. The colour represents the surface gas density in units $M_{\odot}\mathrm{kpc}^{-2}$.

simulate. Furthermore, we define the dark matter particles equal to $N_{\mathrm{DM}} = 10^6$ that will lie within the initiated distribution with a concentration index $c = 9$ and the relevant proportion of the disk mass M_{d} which contain a fixed gas mass fraction f_{gas}. For the disc, the baryonic matter is represented by an exponential stellar disc and an exponential gas disc, since our simulations do not include either a stellar bulge or a black hole. Then, the surface density is described by

$$\Sigma_{\mathrm{gas}/\star} = \frac{M_{\mathrm{gas}/\star}}{2\pi h^2}\exp(-r/h), \tag{2.14}$$

where h is the common exponential scale length in the radial direction for both gaseous and stellar components and is correlated with the disc's angular momentum. The vertical structure of the stellar disk follows an isothermal sheet distribution sech^2 with constant scale length. While the vertical profile of the gaseous disc is estimated self-consistently with respect to the sub-resolution effective equation of state to ensure hydrostatic equilibrium. The self-consistent evaluation is implemented as an iterative method starting from an initial potential guess, which finally converges into a self-consistent solution for the vertical gaseous distribution. In addition, it is possible to attach a proportion of the gas to the halo MHG, which is expected to follow a low-density gas distribution close to the virial temperature.

In our default resolution, the total mass is allocated between the dark matter mass M_{DM}, the gas resides in the halo $M_{\mathrm{gas,h}}$ and the gaseous $M_{\mathrm{gas,d}}$ and stellar components $M_\star$ that constitute the disk M_{disk}. The initial parameters and the resulting mass of each component with the relative mass target are encapsulated in table 2.1. The total $M_{\rm disk}$ is estimated as a fraction $m_{\rm d}$ of the total mass, which is further divided into the disc gas according to $f_{\rm gas}$ and to the collisionless stellar particles. We demand the baryonic matter, including the halo gas, to follow the expected cosmological baryon fraction (i.e $\Omega_{\rm b}/\Omega_{\rm m}$), which leads to fraction MHG $= 0.117$. Subsequently, we attribute the rest mass to dark matter and calculate the number of simulation particles for each simulation element with respect to $\Omega_{\rm b}/\Omega_{\rm m}$. Throughout this, we are able to retrieve the target mass particle of each component and the underlying distribution that afterwards will be used as initial conditions to *AREPO*.

(a)

$\rm v_{200}$	[km $\rm s^{-1}$]	179.9
c		9.0
λ		0.0333
$\rm m_{\it d}$		0.041
$\rm f_{gas}$		0.1
MHG		0.117
$\rm m_{BH}$		0
$\rm z_0$		0.2
$\rm M_{200}$	[$\rm M_\odot$]	2.0×10^{12}
$\rm R_{200}$	[kpc]	265
$\rm M_{DM}$	[$\rm M_\odot$]	1.68×10^{12}
$\rm M_{gas,d}$	[$\rm M_\odot$]	8.20×10^{9}
$\rm M_\star$	[$\rm M_\odot$]	8.20×10^{10}
$\rm M_{gas,h}$	[$\rm M_\odot$]	2.34×10^{11}

(b)

$\rm m_{target}$	[$\rm M_\odot$]	3.15×10^{5}
$\rm m_{DM}$	[$\rm M_\odot$]	1.68×10^{6}
$\epsilon_{\rm DM}$	[kpc]	1.06
$\epsilon_{\rm gas}$	[kpc]	0.60

(c)

$\rm t_\star^0$	[Gyr]	2.27
β		0.1
$\rm A_0$		573
$\rm T_{\it SN}$	[K]	5.73×10^{7}
$\rm T_{\it c,\rm clouds}$	[K]	10^{3}

Table 2.1: **Table (a)** contains the parameters that are used at *MakeNewDisk* in order to extract an isolated galaxy with properties that are denoted in the second half of the table. Namely, it is showed the parametrization of virial velocity v_{200}, the concentration parameter c and the spin parameter λ. The mass is distributed according to disk fraction m_d, which contains an initial amount of gas equal to the fraction $f_{\rm gas}$ and is characterized by a Disk height z_0. MHG and $m_{\rm BH}$ represent the proportion of halo gas and the mass of the black hole respectively. **Table (b)** shows the desired resolution for the baryonic and dark matter particles and the underlying softening lengths. **Table (c)** denotes the parameters of the sub-resolution ISM model. The star-formation timescale $t^0_\star$, the selected IMF is regulated from β corresponding to Salpeter, 1955. Then the supernova feedback is regulated by the effective temperature T_{SN} and the evaporation efficiency A_0, whereas we adopt a temperature of cold clouds equal to $T_{c,clouds}$.

The resulting galactic shape based on the above parametrization is presented in Figure 2.2. It directly denotes the output gas density as it is outputted from the *MakeNewDisk*, thereby we would like to investigate quantitatively whether the generated initial conditions mirror the desired setup for *AREPO*. This isolated galaxy is assembled from 10^6 dark matter particles and 259413 baryonic particles with respect to the cosmological baryon fraction, whereas 25941 of them are attributed to the gas. The initial simulation box is cubic with a length equal to 600 kpc, however, later we will elongate it and shift the galaxy within it. Finally, we calculate the softening lengths for the collisionless and baryonic components. According to Power et al., 2003 the softening needed to prevent artificial gravitational effects is $\epsilon_{\mathrm{DM}} = 4R_{200}/\sqrt{N_{\mathrm{DM}}}$, while for gas is followed a recipe similar to Price and Monaghan, 2007.

2.2.2 Galaxy in wind tunnel setup

In order to study the evolution of a galaxy under the influence of ram-pressure stripping, we perform a wind tunnel setup. The experiment involves the interaction of the cold galactic ISM with the spare, hot ICM of the galaxy cluster, as the galaxy infalling with high velocity towards the potential centre of the system. Rather than simulating both environments directly and letting the galaxy fall into the massive cluster, which requires a very high number of particles, instead we prefer to focus the computational effort on the galaxy and the gas interactions. Thereby, we instate the galaxy model into a wind tunnel. The gas stream is prescribed with initial properties (i.e density, temperature) to depict the ICM and velocity relevant to the infall, as one would measure it from the reference system of the galaxy. Following the configuration of Sparre et al., 2019 and Sparre et al., 2020, where the authors investigate the interaction of a cold cloud under the influence of hot magnetized wind, we will attempt to reproduce a similar setup with the difference that we will examine a galaxy extracted from the *MakeNewDisk* instead of a cold cloud.

Notably, we construct a rectangular box geometry with side length $(L_x, L_y, L_z) = (600, 1200, 600)$ kpc to ensure that the jellyfish evolution will not be confined. Then, we fill the box space linearly with gas particles that are characterized by a density equal to $\rho_{\mathrm{ICM}} = 9.5 \times 10^{-28}\,\mathrm{gcm}^{-3}$ and mass resolution as our initial conditions. The galactic structure is introduced to the system, once we ensure that the density boundaries of the background linear particles and galactic ISM are smoothly merged. This condition is satisfied at galactic radius $r_c = 82.4$ kpc, where we can assume that the two elements are described by a unified distribution. The non-baryonic compoments of the galaxy that exceed r_c maintain their initial distribution. Hence, the resulting

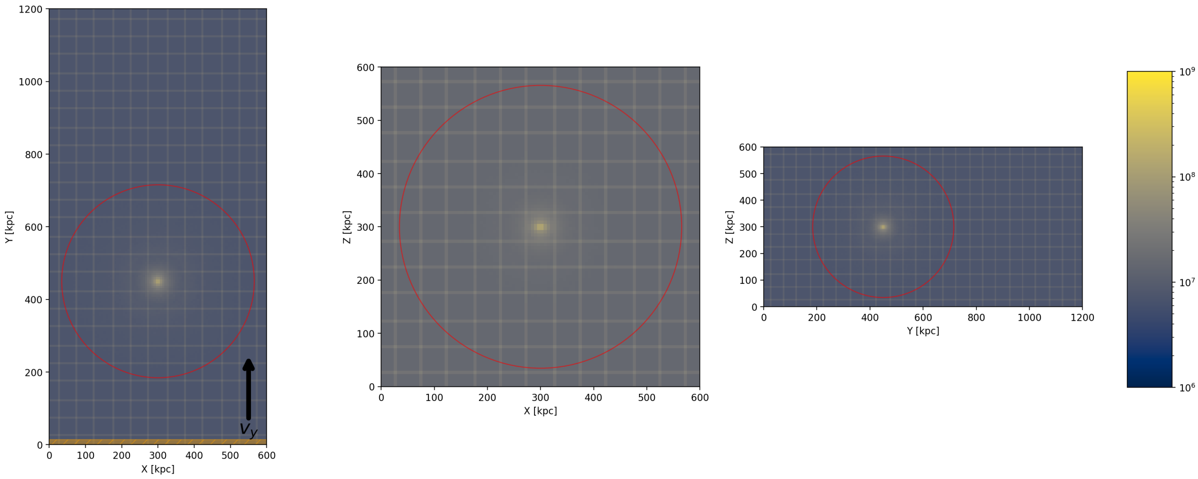

Figure 2.3: The surface gas density in $M_\odot \text{kpc}^{-2}$ units after unification with the linear background density, which corresponds to particles with ρ_{ICM}. The galactic radius where the two distributions are smoothly united is $r_c = 82.4$ kpc, while the R_{200} is indicated with the red circle. The particle distribution outside r_c is completely linear and the "grid" elements consist of visualisation artifacts. The galaxy is placed at $(x, y, z) = (300, 450, 300)$, while the wind is blowing at $\hat{y}$ direction as the black arrow shows. Finally, the orange area near the x-edges denotes the *injection area* .

morphology can be seen in Figure 2.3, as the follow-up to the initial conditions presented in 2.2.

While all the cells in the simulation move with the Lagrangian flow, we define a static volume close to $y = 0$ to remain static with fixed properties. It encloses the first five rows of cells which have a density and temperature equal to the ICM properties (Table 2.2). As the wind blows in the $\hat{y}$ direction, we ensure that new cells are created resembling the hot wind that is propagating with prescribed density, temperature, metallicity, magnetic field and cell volume according to the injection region. Moreover, we impose periodic boundaries at the x and z directions of the simulation volume. Previous wind tunnel setups implement inflow/outflow conditions in the wind propagation direction to remove wind particles that have completed their journey across the box. However, in our case, the injection region condition provides the flexibility to adopt a periodic boundary at the upper y direction, since every newly generated wind particle will be automatically adjusted to our ICM definition.

ρ_{ICM} [g cm^{-3}]	T_{ICM} [K]	$v_{\text{injection}}$ [km s^{-1}]
9.5×10^{-28}	$10^{7.57}$	1190

Table 2.2: The ICM properties that we apply on the wind tunnel setup representing the JO206 jellyfish, derived from Müller et al., 2021a.

Different refinement criteria for the mesh are used to ensure that we resolve the underlying physics in regions that we are interested in and adjust the computation effort more efficiently. When the adopted criteria are met, the mesh cells could either refine themselves by splitting into smaller cells or de-refine by removing the relevant cell, scattering its interior properties (volume and conserved values) into the neighbouring cell or cells. In this setup, we develop the same refinement criteria as Sparre et al., 2019. Firstly, we employ the default mass criterion of *AREPO* (Vogelsberger et al., 2012), which demands the de-refinement of cells once their mass is more than two times smaller than the target mass $m_{\rm target}$. While refinement occurs when the masses of gas cells exceed $2\,m_{\rm target}$. Since the gas resolution is the same for the ISM and the hot wind, this refinement condition results in a higher spatial resolved mesh around the galactic region, where the density is much higher. At the same time, the hot wind particles will be de-refined and modeled coarsely as they will be assumed as lower interest areas. However, we would like to resolve the hydrodynamical processes regarding the interaction of the hot wind with the galaxy, which occurs near the contact boundary upstream of the galaxy. Thereby, we adopt a second criterion to control the volume of a cell with respect to nearby cells. This is called *volume refinement criterion* and ensures that the volume of a cell cannot exceed the volume of its neighbour gas cells by a factor of 8. Invoking both criteria throughout the simulation box, we enforce the mesh to adjust linearly. Therefore, hot wind gas cells will be modeled coarsely once they are injected, and linearly will be refined as they approach the galaxy.

Furthermore, in our simulations, we include a turbulent magnetic field. In this work, we briefly describe how to establish a Gaussian-distributed, turbulent magnetic field similar to Sparre et al., 2020 and for further details about the generation of the setup, we refer to appendencies of Ehlert et al., 2018 and also Ruszkowski et al., 2007. The initial magnetic field $\mathbf{B}$ is generated from a Gaussian random field, which obeys a power spectrum of the form $P_i(k) \propto k^2|\tilde{B}_i(k)|^2$. Each of the three field components $\tilde{B}_i$ follows independently the one-dimensional power spectrum $P_i(k)$ and can be estimated as the absolute square of the Fourier transformation with

$$|\tilde{B}_i(k)|^2 = \begin{cases} A, & \text{if } k < k_{inj} \\ A\left(\frac{k}{k_{inj}}\right)^{-11/3}, & \text{if } k \geq k_{inj} \end{cases} \tag{2.15}$$

where A is a normalization factor, k is the wavenumber $k = 1/\sqrt{x^2 + y^2 + z^2}$ and k_{inj} is the injection scale. The above relation implies that $\mathbf{B}$ follows white noise on the largest scales with a wavenumber smaller than the injection scale, whereas for $k \geq k_{inj}$ we have Kolmogorov turbulence. The normalization factor is decided according to the magnetic field strength $\sqrt{\langle \mathbf{B} \rangle^2}$, which is scaled by the magnetic-to-thermal pressure ratio $\beta = P_{\mathrm{th}}/P_B$. Again, following Sparre et al., 2020 we inject a turbulent magnetic field along the x-axis perpendicular to the wind velocity. We have to set a turbulent cubic box with side length $L_x = 600\,kpc$ and periodic boundary conditions, which defines the injection wavenumber as $k_{inj} = (1/\sqrt{3}L_x)$. This way is ensured that the cells that reside within the *injection region* receive the desired magnetic configuration along the y-axis in the injection region and hence propagate the magnetized wind throughout the rectangular simulation box.

Finally, given the setup described above, we perform three simulation runs. All of them are started from the same initial conditions in order to enable the direct comparison and study of how the ram pressure affects a galactic system and in particular with the presence of a turbulent magnetic field. Hence, we present a simulation run where the hot ICM wind is switched off and the galaxy is evolved in isolation, one instance of hydrodynamical (HD) jellyfish evolution, and finally, a fully MHD treatment of the case including magnetized turbulent wind, where the magnetic-to-thermal pressure ratio is set as $\beta = 50$ and the initial magnetic field of the disc is 20 μG.

Chapter 3

Analysis

Throughout this chapter, we present the analysis of the simulation results which proceed as follows: in section 3.1 discussed the main physical aspects associated with the evolution of jellyfish evolution, in section 3.2 investigated the effects of the ram pressure on the gaseous component and the underlying SFRs during the evolution and finally in section 3.3 examined the tail morphology and the survival regime of the stipped clouds.

3.1 Evolution of the jellyfish galaxy

As we describe in section 1.2, galaxy evolution is associated with morphological transformation, which is regulated by the consumption of star-forming gas. We commented on several internal and external quenching mechanisms able to suppress SFR, and thereby disrupt a blue galaxy from the main sequence. This can happen in different timescales, according to the impact of a quenching event on the ISM. Therefore, the ISM gas reservoir is exhausting in timescales that are linked with the quenching mechanism until the final reach negligible SFR, while any external source of fresh gas has ceased. If the event quenching timescale is short, it might lead to a starburst event, where the vast amount of cold ISM rapidly collapses to stars, letting the galaxy "dry" extremely fast. Once the galaxy ran out of fuel, it starts to diverge from the main sequence and begins its journey across the green valley. In the current work, we reproduce a ram-pressure stripping case of a sufficiently large gas-rich galaxy. We attempted to resemble the infall scenario via a wind-tunnel experiment, where a magnetised wind defined with the underlying ICM features will be blown across the galaxy. The general evolution is described in this section, where we will investigate the physical aspects of the jellyfish evolution for the MHD and HD simulation runs.

The global scheme is generated through the external ram pressure exerted on the disc, driving the removal of the ISM from the galactic structure. The galaxy appears as an obstacle in the high velocity $v \simeq 1200\,\mathrm{km},\,\mathrm{s}^{-1}$ wind with Mach number $M = 1.3$, which causes a bow shock in the upstream region of the galaxy. Hence, hydrodynamic friction at the interface between the cold ISM and the hot ICM would result in the growth of hydrodynamical instabilities in the gas, such as Rayleigh-Taylor (RT) and Kelvin-Helmholtz (KH) instabilities. The RT instabilities tend to tear apart the structure producing a ”finger-like” morphology and are suppressed for the inner gas disk that survives ram pressure stripping (Roediger and Hensler, 2008), due to the gravitational acceleration of the disc. While KH instabilities are induced due to the shear of the velocity flow (the velocity difference between the ISM and ICM) as the wind streams around the galaxy. In this interference region, the formation of KH instabilities, and thus vortices, are able to accelerate the gas stripping process from the galaxy and efficiently mix it with the downstream flow. In our work, we mainly focus on the influence that KH instabilities have on the jellyfish evolution and most importantly how are regulated in presence of a turbulent magnetic field. Generally, KH instabilities act decisively regarding the fate of the stripped gas as they drive it to the downstream region. In that sense, the detached ISM parts from the parent galaxy tend to dissolve faster with the hot ambient wind, in presence of stronger KH instabilities. However, observations (Cramer et al., 2019) depict a long star-forming tail of dense star-forming gas, implying that the ISM gas survives the transferring/stripping process. This could possibly be explained due to a mechanism that is able to suppress the KH instabilities. Indeed, ”cold-cloud” simulations (McCourt et al., 2015) found that magnetic fields are able to suppress the disruption of the clouds, rather than dissolve it in the ambient hot medium, due to *magnetic draping* (Dursi and Pfrommer, 2008). This effect states that as the relative structure moves through the hot gas, it sweeps up magnetic field lines at its leading edge, building a sheath around the cloud. The magnetic field strength in the boundary layer (once a steady state is reached) is a result of a competition between sweeping up and slipping of field lines and is comparable to the ram pressure that the structure experience. It turns out, the formation of a magnetic draping sheath provides enough magnetic tension to the interface instabilities, and hence KH instabilities with a wavelength smaller than one-tenth of the thickness of the draping layer are suppressed (Dursi, 2007). This allows the stripped gas to be transported more effectively with prolonged survival time, as the radiative cooling timescale is shorter than the timescale of hydrodynamical instabilities (Gronke and Oh, 2018). Such as regime implies that stipped clouds can resist evaporation events and maintain their initial properties through the in-situ star formation. Based on that, Sparre et al., 2020 investigate the impact of various magnetic field configurations in the survival scheme of the stripped gas, where in the case of turbulent magnetised wind, the cold stripped clouds reveal great sustainability during the entrainment. In particular, under some specific conditions, the ISM tail gas from the parent structure could be mixed with the hot wind at intermediate temperatures and becomes thermally unstable and eventually cool, setting a growth regime in the stripping tail. Furthermore, the authors commented on the formation of a magnetised dense filamentary gaseous tail due to the ICM condensation, which will be characterized by ordered and aligned magnetic fields across the wind direction. A morphology in agreement with observations (Müller et al., 2021a) and MHD simulations (Ruszkowski et al., 2014; Vijayaraghavan and Ricker, 2017).

The main quantities of our work are encapsulated in Figure 3.1 for the MHD case and Figure 3.2 for HD. These figures illustrate the same quantities from left to right for the projected x - y midplane, the mass density ρ, the temperature T, the thermal pressure P_{th}, the metallicity in solar units and the viscosity magnitude $\omega = |\nabla \times \mathbf{v}|$ of the simulated particles. The total time interval that the system evolved is 4 Gyr equal to the *dynamical timescale* of the "cluster" and the snapshot timestep is 100 Myr. The selected snapshots mainly referred to the earlier times of the simulation, since after 2.5 Gyr most of the ISM gas has been stripped. In figure 3.1, the first row indicates the first encounter of the galaxy with the hot wind at time $t = 0.3$ Gyr. We can directly notice that the exerted ram pressure truncates the initial galactic disc, driving the gas outside of it towards the tail. From the density and temperature, we can identify the stripping radius quantitatively, as there is a jump in the quantities where cold ISM clouds escape the disc. In front of the galaxy, the expected ICM compression becomes clear from the third column, where we can see an enhanced thermal pressure in between the bow shock and the galaxy, constituting the magnetic draping sheath. While the ram pressure cannot move stellar

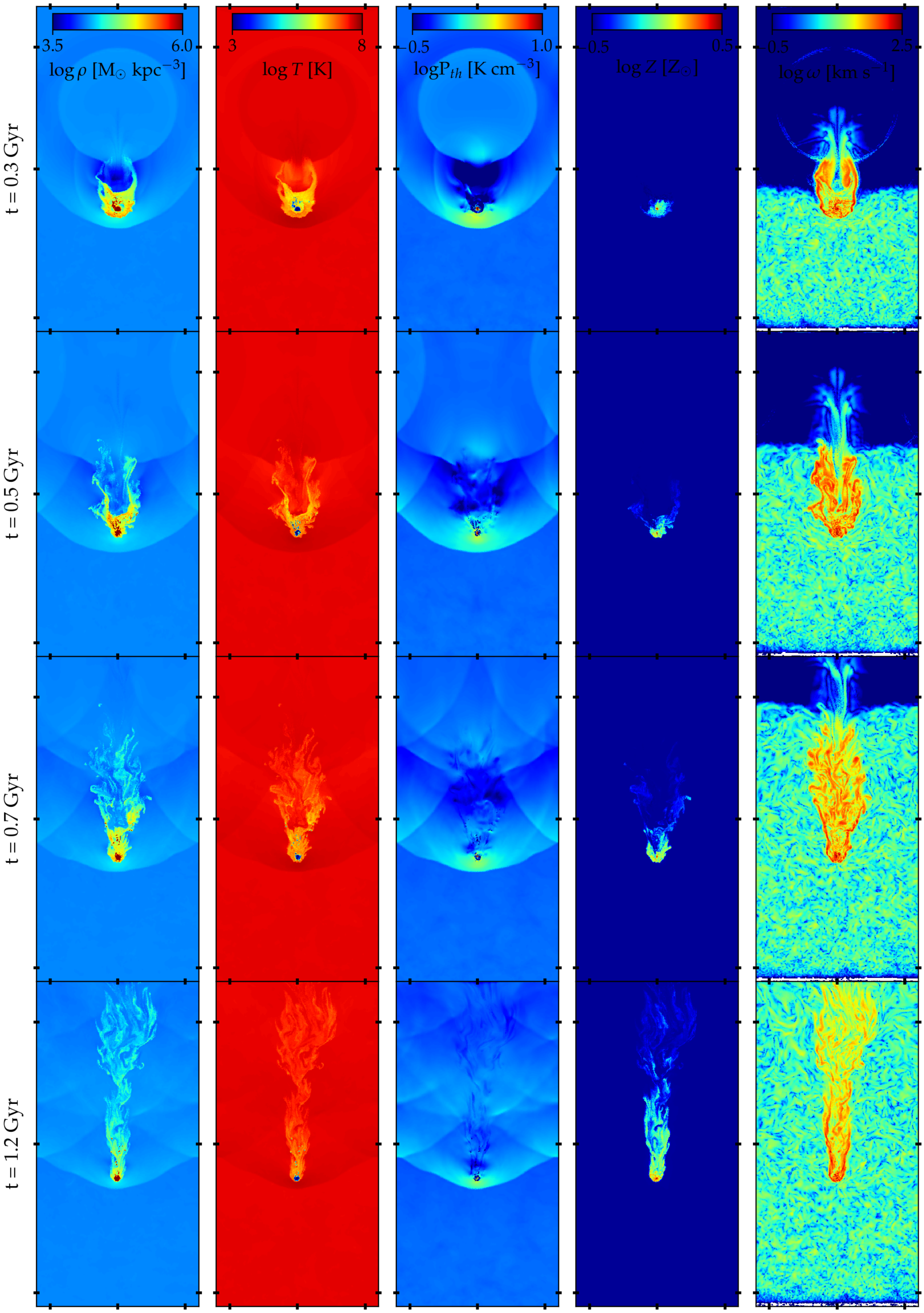
3.5
6.0
log ρ [M$_\odot$ kpc^{-3}]
3
8
log T [K]
−0.5
1.0
logP$_{th}$ [K cm^{-3}]
−0.5
0.5
log Z [Z$_\odot$]
−0.5
2.5
log ω [km s^{-1}]
t = 0.3 Gyr
t = 0.5 Gyr
t = 0.7 Gyr
t = 1.2 Gyr

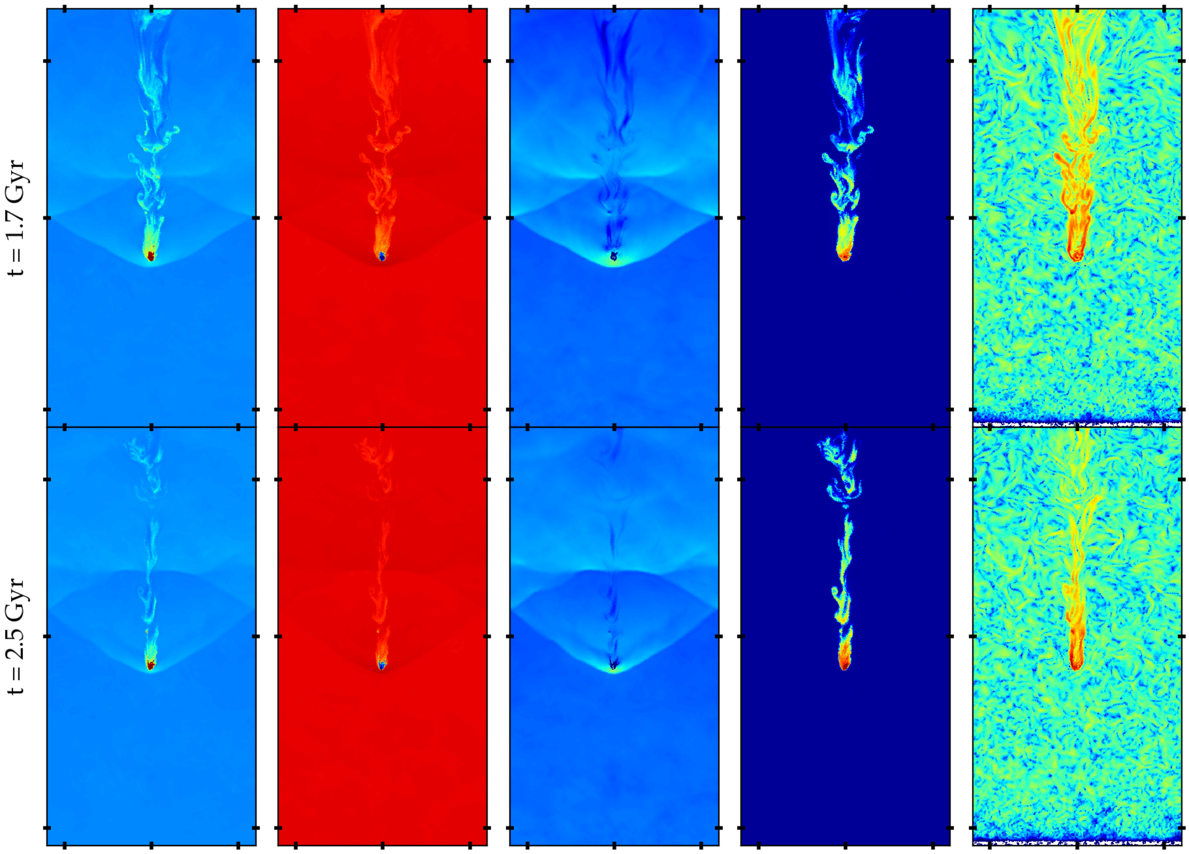

Figure 3.1: The gas structure for the MHD run. The projected slices of $x - y$ show the temperature, density, thermal pressure, metallicity and vorticity of the gas. Each panel has a dimension of 600 kpc × 1200 kpc and shows the average of 14 layers of thickness $dz = 0.03$ kpc around the centre of z axis, while the direction of the wind is aligned with the y axis. The colour scales logarithmically and the colorbar is fixed at all times.

clumps, it can affect the stellar distribution of the galaxy indirectly, as the stripped ISM can form stars. This becomes clear from the gas metallicity panel which presents some delay in comparison to the gas density. The stripped ISM then will condense and mix with the ICM in the tail, thus forming stellar populations outside the galactic plane (in situ), which eventually would chemically enrich the gas cloud in the tail. Moreover, it is possible for those structures (especially the collisionless particles) to eventually fall back on the stellar disc (Vollmer et al., 2001; Steyrleithner et al., 2020), due to the gravitational attraction from the galactic disc. Generally, several observational surveys denote the presence of clouds in the tail that formed within the friction layers, where turbulences and instabilities are quite strong. The generation of vorticity in our simulations, as a result of instabilities, is shown in the last column. Indeed, the vortex field indicates that the gas flow in the tail is strongly influenced by the instabilities.

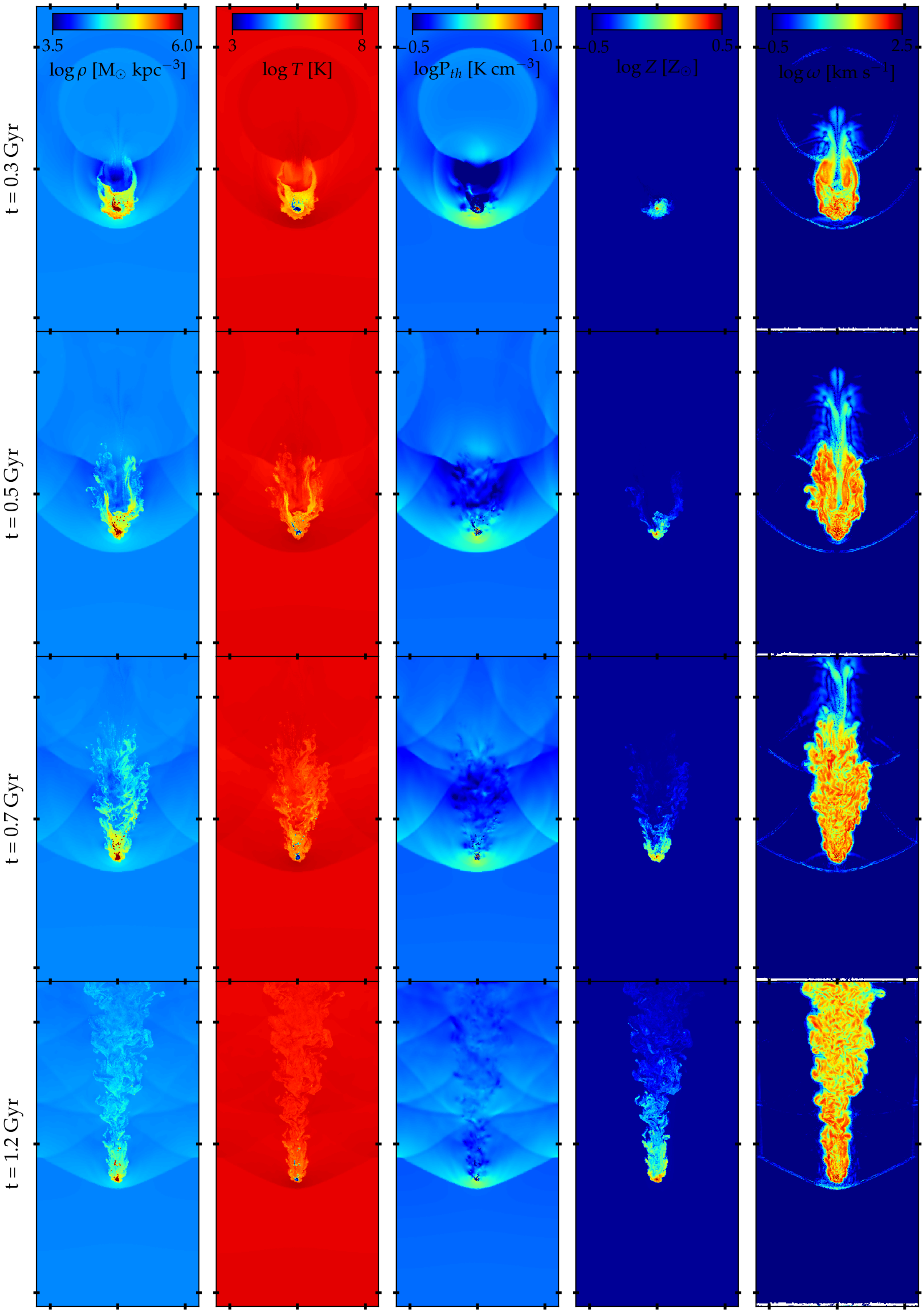
3.5
6.0
log ρ [M⊙ kpc−3]
3
8
log T [K]
−0.5
1.0
logPth [K cm−3]
−0.5
0.5
log Z [Z⊙]
−0.5
2.5
log ω [km s−1]
t = 0.3 Gyr
t = 0.5 Gyr
t = 0.7 Gyr
t = 1.2 Gyr

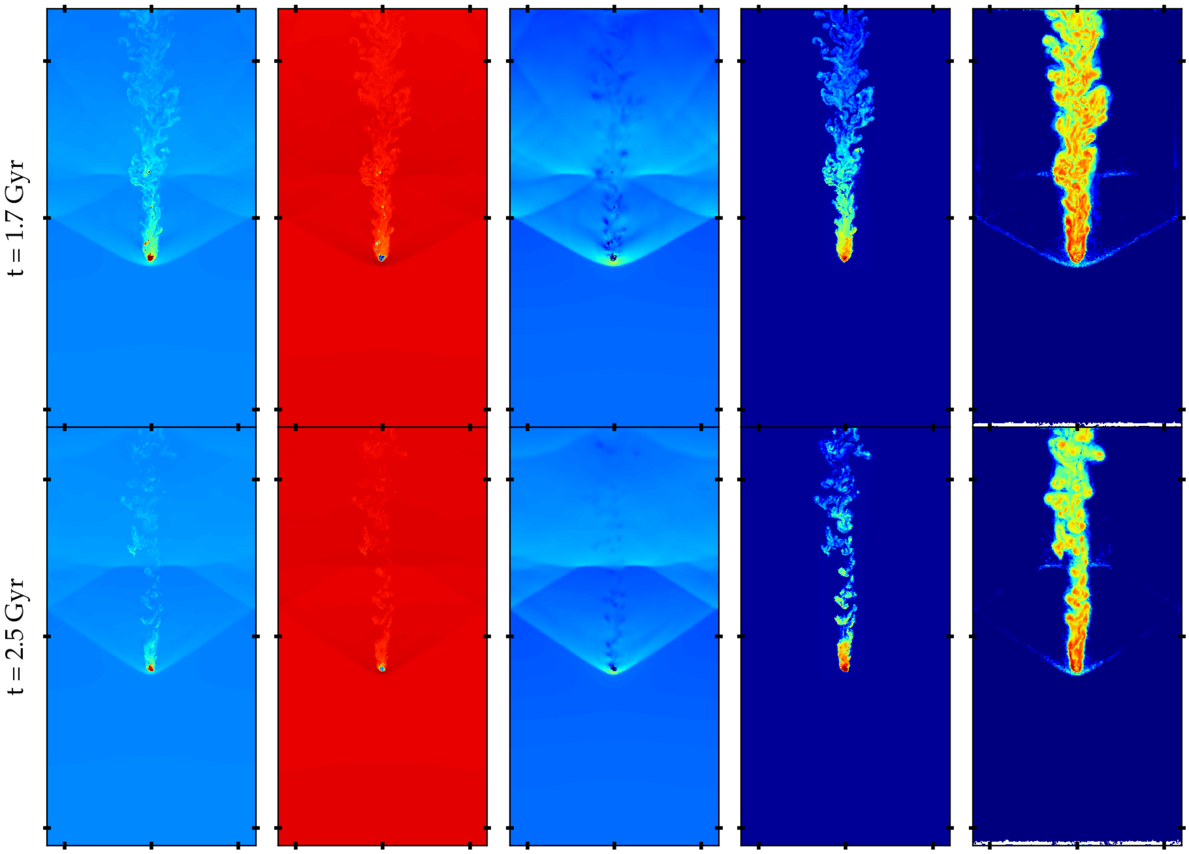

Figure 3.2: Same as the previous panel plot but for the HD simulation run.

Tracking the evolution until 0.7 Gyr there is an intense release of cold ISM gas, that is associated with larger widths for the tail. The existence of cold clumps downstream supports the in-situ star formation in the tail and potentially could reproduce the observational features. Once the tail acquires its final vertical shape at 1.2 Gyr, the stripping becomes significantly weaker and the KH instabilities are mainly limited to the edges of the stripping material. This might be attributed to the absence of fall-back material, as an important fraction of cold dense has already been already stripped, and hence, the vortices are limited to the magnetic draping sheath due to the continuous gas dragging phase. Finally, Figure 3.2 illustrates the same quantities for the HD rum. Generally, it seems that the stripping process follows a similar scheme, however, it is noted significant dispersion on the inner tail small-scale motions. The degree of turbulence and the intensity of vortices in the tail is regulated by the KH instability. The magnetic field strength regulates the vorticity production, as the draped magnetic lines around the galaxy exert magnetic tension, stabilising the small-scale perturbations within the tail structure. In non-magnetic environments the tail is more turbulent, demonstrating that the stripped gas is more prone to mixing events and thus evaporation into the hot ICM wind. From the snapshot 1.2 Gyr is set clear the impact of magnetic fields, as MHD reveals more filamentary morphology in the tail where denser gas resides, whilist the HD gas morphology appeared more diffuse and turbulent. This strengthens the results from Sparre et al., 2020, as a filamentary tail morphology indicates a more isolated evolution of the stripped gas from the ICM.

3.2 The impact of ram pressure stripping on the galaxy

In this section, we investigate gaseous component response due to the exerted ram pressure. In subsection 3.2.1 we employed an instant criterion to separate the ISM galactic gas from the ICM wind based on the temperature-density phase. Through this, we verified that the MHD simulation appears higher ISM masses, especially at later times. In order to perceive a more accurate gas distribution, in section 3.2.2 we estimate the stripping radius and the relative ISM mass content below and above it. Furthermore, based on that in section 3.2.3 we evaluate the underlying SFRs and the quenching path of the evolved galaxy.

3.2.1 Galaxy Properties

As discussed before the exerted ram pressure on the galactic disc will induce dramatic changes in the intrinsic properties and the morphology of the galaxy. An "outside-in" gas stripping is expected, leading to the suppression of the diffuse atomic and molecular gas. The former which constitutes the star-formation reservoir will be directly swept from the interaction, causing a HI deficiency, while the latter is deeply embedded in the gravitational potential and will be either affected indirectly by the lack of star-forming gas or stripped away once the stripping radius decreases and the molecular clumps are exposed to the ICM wind (Tonnesen and Bryan, 2009). Subsequently, the star formation activity of the perturbed galaxies decreases, due to the steep decline of the available gas, forming truncated gas discs whose radial extension is relative to HI-deficiency (Roediger et al., 2006). However, the galaxy might experience a short starburst phase before starting the evolutionary path across the green valley (see section 1.2.4). The origin of the burst can be due to the inclination angle of the infalling galaxy. In our configuration the inclination is edge-on, suggesting that most of the stripped gas has to cross the stellar disc as moving towards the tail, favouring gas collapse and star formation due to the rise of instabilities (Lee et al., 2020).

Before we proceed to the detailed analysis regarding the evolution of galactic compoments, we describe how we separate the gas particles residing in the ISM and the ICM wind within the simulation volume. As described in section 2.2.2, the infalling scenario is simulated by ICM gas particles as they flow periodically across the $\hat{y}$ axis, where their intrinsic properties are

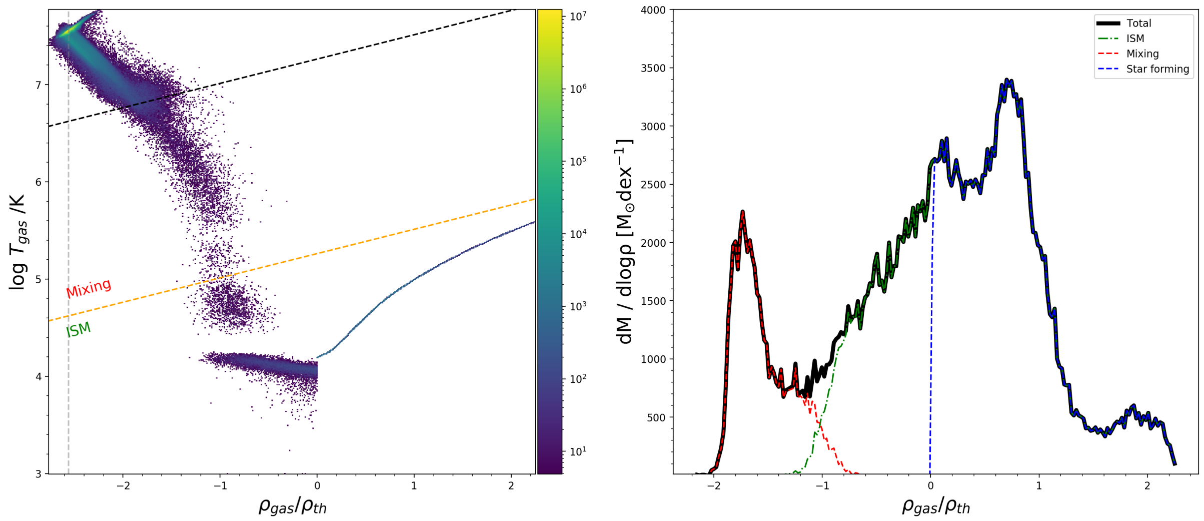

Figure 3.3: *Left figure:* the gas density–temperature phase diagram logarithmically scaled according to the amount of mass in each cell of the two-dimensional histogram for $t = 1.3$Gyr. The orange line distinguishes the ISM gas cells (below) from the hotter gas phase (above) according to Torrey et al., 2012. The one -dimensional curve starting from $\rho_{\rm th}$ presents the star-forming gas. It is also included an elevated form (black line), where we assume that a mixing phase of gas located. The injection density of the ICM wind is denoted from the vertical grey line. The *right figure* shows the differential gas mass for the corresponding regions of the $\rho - \rm T$ diagram.

redefined once they pass from the *injection region*. The initial state of the galaxy before the stripping process is described by a cold ISM embedded into a hotter halo gas. However, the ram pressure stripping will rapidly alter this morphology with an "outside-in" tendency. In order to distinguish these two phases we employ a density–temperature diagram as can be seen in Figure 3.3. The position of a gas cell within this two-dimensional histogram reveals the gas origins and phase, while the colorbar is assigned according to the relative mass logarithmically scaled within each bin for all the gas (ISM + ICM) inside the simulation volume. Generally, the behaviour of the gas in this diagram is closely related to the galaxy formation model described in subsection 2.1.2. The framework of our subgrid star formation model involves a star formation threshold $\rho_{\rm th}$, where gas cells with higher densities are described by an effective equation of state and constitute the star-forming gas. The grey line vertical lines indicate the prefixed density of the ICM wind, where the hot wind is located. To separate the ISM phase from the hot gas, we use the same $T - \rho$ cut as was initially employed by Torrey et al., 2012 :

$$\log\left(\frac{T}{[K]}\right) = 6 + 0.25\log\left(\frac{\rho}{10^{10}[\mathrm{M_\odot h^2 kpc^{-3}}]}\right) \ , \tag{3.1}$$

using $h = 0.7$, which takes the form of the orange line. Every gas cell below this line will be considered as the ISM with M_{ISM}. Moreover, we introduced an elevated form of the cut (black line) including gas with maximum temperature 10^7K, covering a region where the mixing processes occurred as a result of either the ICM compression or the dissolution of the galactic gas. A more quantitive perspective of the adopted ISM separation is shown in the right figure. Notably, a double peak morphology describing the ISM and ICM mass contribution of the cells below the black line. The low mass fraction between the peaks might occur due to the short cooling times that are associated with the enclosed temperature range.

Given that, the top panel in Figure 3.4 shows the evolution of the ISM gas during the simulation. As expected the isolated galaxy maintains an almost constant gas mass profile. The slight gas losses and gains could be attributed to the galactic baryon cycle e.g internal feedback mechanisms that gradually exhausts the star-forming gas and are counterbalanced by external supply processes. On the other hand, we can distinguish two phases for the mass evolution of the HD and MHD cases. An early stage where both runs reveal nearly the same profile until $t = 1$ Gyr and a second stage where the contained mass shows a discrepancy in favour of the MHD run. Generally, the stripping process can be subdivided into two classes, the ram pressure pushing according to Gunn and Gott, 1972 and a continuous gas dragging due to KH instabilities Nulsen, 1982 proportional to stripping radius (since in our case, the ICM density and velocity remain constant). The impact of magnetic fields seems to be weak during the first $t = 1$ Gyr, as the relative ratio of the stipped material is almost identical for unmagnetised and magnetised galaxies (Tonnesen and Stone, 2014). Interestingly, the second phase appears that magnetic fields are indeed associated with higher mass fractions. This outcome could be interpreted as a result of the suppression of KH instabilities. This way, the ISM gas is effectively shielded retaining its internal properties against the ICM wind, whilst in the HD case, the ISM gas clouds are shattered faster and eventually mixed and dissolved in the hot wind. Thereby, magnetic fields support the tail clouds against KH instabilities, leading to larger unmixed structures in the tail, as those observed in J0206 and other jellyfish galaxies (Cramer et al., 2019).

The second panel in Figure 3.4 shows the cumulative stellar mass that was formed during the

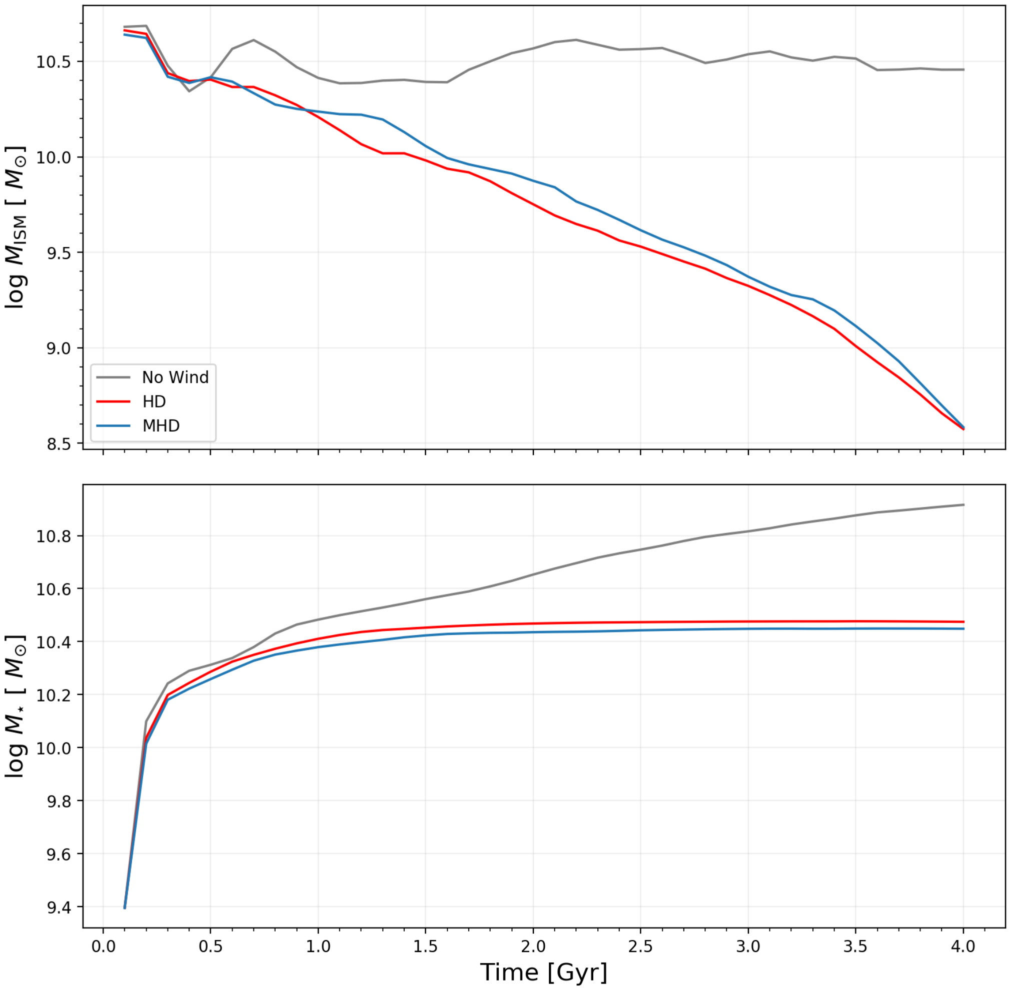

Figure 3.4: *Top figure:* the evolution of ISM gas during the simulation. While the no wind case appears with small deviations during the simulation, the HD and MHD reveal two stages during the ram pressure. Below $t = 1$ Gyr the system experience nearly the same gas stripping regardless of the presence of magnetic fields. For later times the MHD description preserves larger quantities of gas, indicating the effective suppression of KH instabilities and hence the unmixed morphology of ISM clouds.*Bottom figure:* the cumulative stellar mass that formed during the simulation runs. Generally, MHD and HD runs halt the star producing indicating a quenched galactic profile. Both profiles generated most of the stars until $t = 1$ Gyr and after that maintain a passive shape.

three simulation runs. In this plot, the quenched profile of HD and MHD runs becomes clear, as the no-wind galaxy maintains a constant producing rate, in comparison to the ram pressure galaxy that after 1 Gyr adopt an extremely passive profile. More specifically, both ram pressure cases produced approximately 10^9 $M_\odot$ after that time, an order of magnitude less than the pre-existed stars. These results are in agreement with previous simulations, that showed strong ICM winds are decreasing the stellar mass formed during the simulation (Lee et al., 2020).

The constant offset between HD and MHD might be occurred due to the more intense SFRs, foreshadowing that the gas for the HD case is more unstable than MHD gas.

3.2.2 Stripping radius

After discussing the effects of ram pressure stripping on the gaseous and stellar compoments, it would valuable to investigate how the initial galactic disc evolves during the interaction. Initially, we calculate the stellar half-mass radius $R_{1/2}$, speculating that the stellar disc is confined at $2R_{1/2}$. Then, based on Gunn and Gott, 1972 criterion, according to which galaxies lose material if the force due to ram-pressure stripping exceeds the restoring gravitational force of the galaxy, we estimate whether the stellar disc is stripped. This implies the existence of a stripping radius, where the galactic gravitational potential cannot prevent the ISM from being stripped. Given that, the radii at which a disc galaxy will be truncated for face-on inclination can be found from :

$$P_{\mathrm{ram}} \geq 2\pi G \Sigma_{\star}(r_{\mathrm{str}}) \Sigma_{\mathrm{ISM}}(r_{\mathrm{str}}), \tag{3.2}$$

with ram-pressure $P_{\mathrm{ram}} = \rho_{\mathrm{ICM}} v_{gal}^2$ and $\Sigma_{\star}$, Σ_{ISM} the surface density of the stars and gas respectively. Typically, P_{ram} is a function of time as a jellyfish is in an eccentric orbit, causing the ICM density and the galactic velocity to change. However, as discussed in section 2.2.2, in the current wind-tunnel experiment we adopt constant $P_{\mathrm{ram}} \simeq 1.3 \times 10^{-11}\ \mathrm{gcm^{-1}s^{-2}}$, according to the measured speed of sound and Mach number of J0206 (Müller et al., 2021a). The above criterion provides an effective upper approximation for the stripping radius, assuming that the infalling inclination angle is face-on. In our case the inclination is edge-on, leading to a significant deviation from the real stripping radius, as the interference area is limited to the leading front region of the galaxy. Previous works employed different ways to carry out this calculation, based on the above criterion. In particular, Domainko et al., 2006 analytically determine by parametrizing the stripping radius over the initial disk scale length and in some cases authors approximate it through the total gravitational potential (Roediger and Brüggen, 2007). In our analysis, we investigate the Gunn & Gott criterion via the gas pressure within the galactic disc. When a satellite galaxy enters the hot ICM, it encounters the ram pressure and thermal pressure of the ICM, and thus the galactic gas is stripped whether $\rho_{\mathrm{ICM}} c_s^2 (1 + \mathrm{M}^2) \geq P_{\mathrm{gas}}$ is satisfied. The gas pressure is measured in spherical coordinates around the centre of the galactic disc,

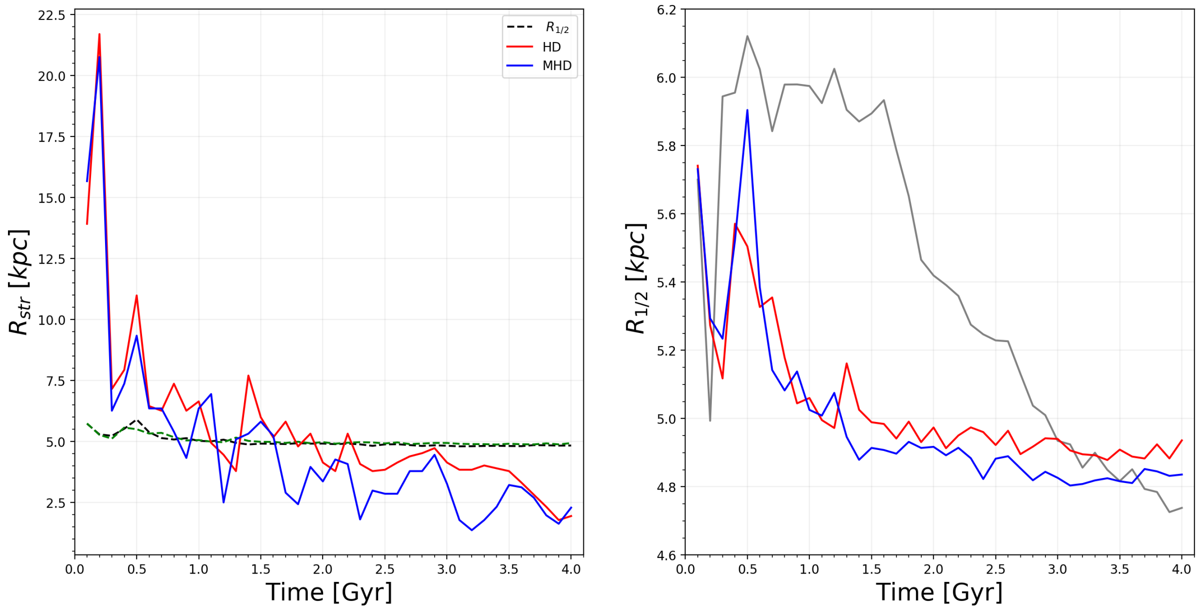

Figure 3.5: Time series of the stellar half-mass radius (*right figure*) and the stripping radius (*left figure*) for our simulation runs. The outside-in stripping leads to significant shrinkage of the stripping radius below the inner stellar disc. The stripping radius for both cases presents an oscillating profile due to the fallback instances.

from gas located within spherical shells $[r_{\rm str}, r_{\rm str} + \Delta r]$. This way we avoid the encounter of measuring the surface densities with inclination correction terms and parametrizations sensitive to the evolving disc lengths.

In figure 3.5, is presented the resulting stripping radius and the stellar half-mass radius for the simulation runs. While the ram pressure stripping acts only on the gaseous component, the radial deviation of $R_{1/2}$ extent has occurred as an indirect effect of the gas removal. Generally, a decrease is expected as the initiated disc galaxy contains significant amounts of star-forming gas, which gradually will be converted to stars and thus increase the binding energy constituting a more compact disc (grey line). On the other hand, the ram pressure stripping cases denote much more sharp shrinkage because the gas removal has a radical impact on the baryonic cycle and the final stellar distributions. Both runs reveal similar profiles of $R_{1/2}$, with the HD case to note slightly higher values for later times, which can be justified if we consider the higher amount of generated star mass (see Figure 3.4). The left figure shows the stripping radius estimated according to the criterion discussed previously and the underlying $R_{1/2}$. Throughout the interaction, the stripping radius shrinks efficiently after some Myr resembling the "outside-in" stripping scheme. As the gas surface density constantly reduces due to the stripping, the equilibrium between internal and external forces is satisfied for radii closer to the galactic centre. This phenomenon would occur at distances smaller than $R_{1/2}$ at $t \sim 0.9$ Gyr and $t \sim 1.1$ Gyr for the MHD and HD case respectively, providing us with an idea regarding the ram-pressure stripping time-scales. Yet, both cases present some oscillation behaviour around the $R_{1/2}$, demonstrating a "fallback cycle" of the stripped gas. That means as the gas is drawn away from the parent galaxy causes the stripping radius to expand to larger radii in order to be achieved an equilibrium between internal and external forces. However, a significant fraction of stripped gas could remain bound to the galaxy and fall back, inducing consequential variations in the stripping radius. So, a hypothetic ram pressure stipping event without accounting for the fallback case would imply a constant decrement of the stripping radius, instead of the current oscillating profile. Finally, the extracted stripping time-scales are quite difficult to validate precisely, as previous tuned simulations include homogeneous gas phase leading to underestimation of ram pressure stripping (Tonnesen and Bryan, 2009), different galaxy types (and thus potential wells) and ICM parameters, varying from several Myr to ~ 1 Gyr (Lotz et al., 2019).

In order to validate whether the adopted radii could be used to separate the tail gas from the stripped disc we inspect the galactic region from a different perspective. Initially, the geometry of the problem indicates that the optimum coordinate system to evaluate the evolution of the tail properties is cylindrical. For this reason, we employed a cylinder of $r = 30$ kpc aligned with the wind direction including all the simulation particles (ISM + ICM) along the line of sight. The projected range captures a narrow region around the stripped galaxy, where at $y = 0$ is located the potential minimum of the galactic disc. For illustration purposes, Figure 3.6 shows the basic gas properties for an intermediate MHD snapshot at time 1.2 Gyr with the stripping radius $R_{\rm str}$ and the stellar radius $2\,R_{1/2}$ that obtained as discussed in the previous paragraphs. Initially, as discussed in subsection 2.2.2 the injection region refines the thermal properties of the turbulent magnetised wind, driving a constant hot-dilute wind onto the galaxy. As the wind approaches the galaxy, it is noted a jump in all properties at nearly $y = -40\,\text{kpc}$ from the galactic centre. We identify this region as the bow shock due to the exerted compression from the wind ram pressure. The shock compressed density, temperature and thermal pressure are

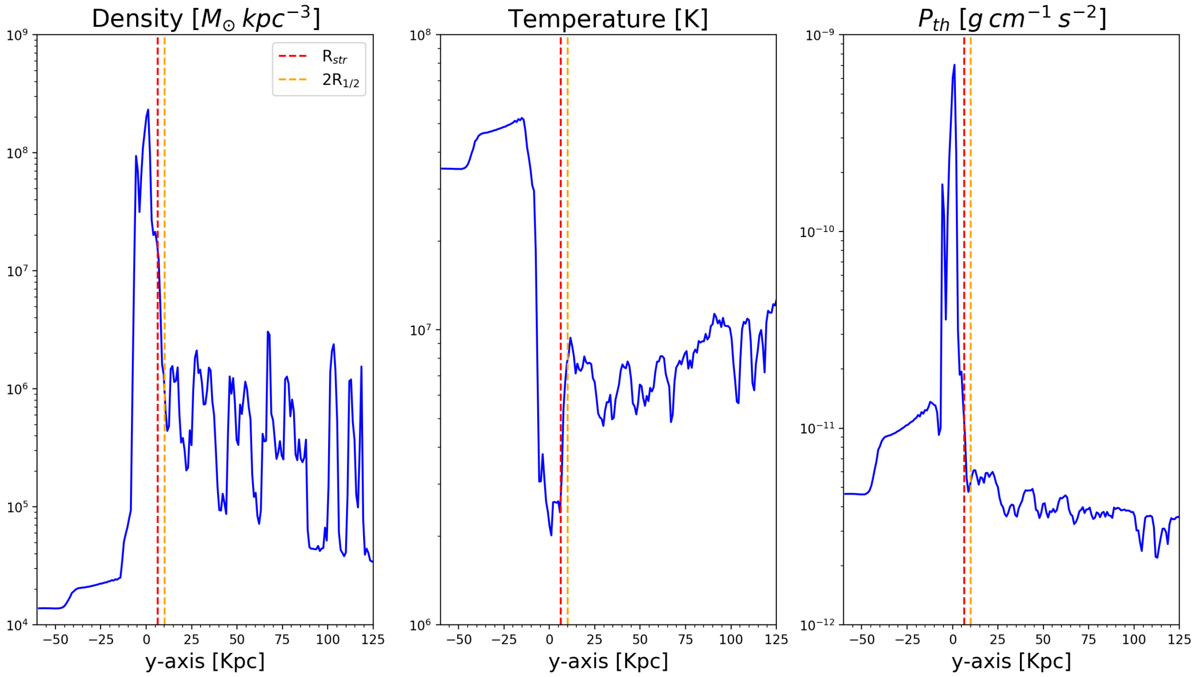

Figure 3.6: The mass density, temperature and thermal pressure of gas for all the simulation particles within a cylinder of radius $r = 30$ kpc oriented along the wind direction. The selected MHD snapshot represents the gaseous state at time 1.2 Gyr. The location of the bow shock is identified at $y = -40$ kpc, where Rankine Hugoniot jump conditions are verified according to the injection properties. Downstream the galaxy is apparent a rich morphology of stripped gas, which resides well above the stellar radius.

found in agreement with the Rankine Hugoniot jump conditions for a shock with Mach number $M = 1.3$ and adiabatic index of 5/3 in the post-shock region. Downstream the galaxy, it is evident that has released a significant amount of gas. The sharp spikes especially in the first two figures denote that the tail includes small dense-cold clouds, strengthening the scenario for in-situ star formation. Overall, our simple pressure equilibrium assumption seems to well capture the gas disc range (we neglect the magnetic pressure in the MHD case since it does not dramatically affect the total pressure budget in the disc in the current simulation). However, it is essential to mention that the gas state around the disc is quite turbulent, as gas is stripped and infall to the disc at the same time. Given that, for the rest of the thesis, we will adopt a more stable separation condition for the tail boundaries based on the range of the stellar disc, i.e $2\, R_{1/2}$.

With these factors in mind, Figure 3.7 shows the ISM mass (see subsection 3.2.1) for the radius below and above the stellar disc $2R_{1/2}$. Once again, we confirm that the presence of magnetic

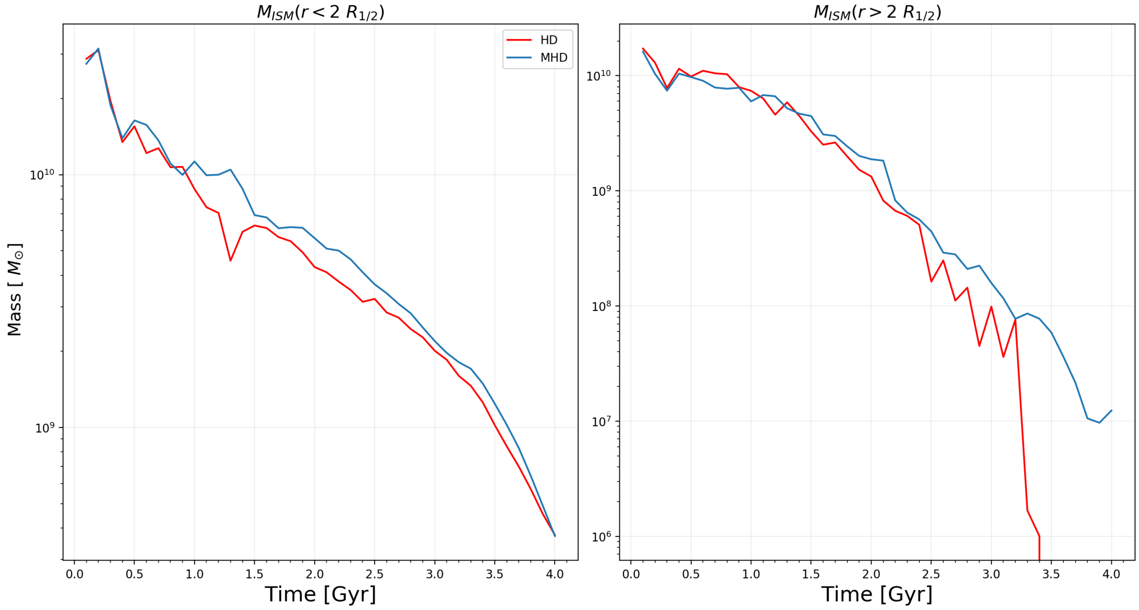

Figure 3.7: The enclosed ISM mass below the stellar disc *left figure* and the tail *right figure*. In both cases, the magnetic fields are linked with the sustainability of the ISM. clearly, at later times the tail indicates the effective suppression of KH instabilities resulting in higher ISM mass.

fields is linked with a higher amount of ISM gas across the jellyfish galaxy. Particularly, this becomes evident after $t \sim 0.9$ Gyr for the inner part, whereas the tail appears some delay. In later times, the $M_{\rm ISM}$ in the tail has declined over 3 orders of magnitude, as most of the gas has already been stripped, however, the effective suppression of the KH instabilities in MHD case supports the sustainability of the cold ISM clouds in comparison to HD. In the left figure, the mass peaks within $2R_{1/2}$ coincide with the radius stripping minima in Figure 3.5, as the stripping radius shrinking is associated with the new galactic material releasement from the galaxy. Nonetheless, the selected spherical region not only tracks the ejections but also the fallback instances.

An interesting behaviour takes place at time $t \sim 1.3$ Gyr. While the MHD follows the scheme that we described before, the HD presents an important decrement, which might be attributed to a strong tidal interaction of stripped as it infalls back to the galaxy (see Figure 3.12), driving material from the wake to the leading edge of the galaxy. This outcome is extremely interesting as the MHD treatment is not only able to provide magnetic shielding of the ISM clouds against the KH instabilities in the tail (right figure) but also to confine the fall-back stripped material within the galactic disc due to draping of ”ICM” magnetic field around the galaxy, which forms a protective layer with magnetic pressure relative to the ram pressure.

3.2.3 Star formation rate

After discussing the spatial distribution of the ISM mass within the simulation volume, it would natural extension to investigate the associated star formation events. Adopting the same separation for the disc and tail, Figure 3.8 is presented the star formation rate of the whole jellyfish system and the tail structure, which lies above $2R_{1/2}$. Inspecting the figure, we see a common evolution for the three simulations until the ICM wind eventually reaches the galaxy at $t = 0.3$ Gyr. At $t = 0.2$ Gyr a simultaneous transient growth is noted due to the relaxation of the galaxy from an approximate equilibrium to a self-consistent system. The first deviations appear at times $t = 0.5$ Gyr, where in particular is reported an enhanced SFR relative to the no wind counterpart. The origin of this burst emerged from the edge-on inclination of the infalling galaxy. Similar simulations have commented on this behaviour, as most of the perturbed gas has to cross the stellar disc and interact with the rest of the ISM before eventually being removed from the galaxy (Lee et al., 2020), in line with observations (Boselli et al., 2021). Throughout the rest of the evolution, the MHD and HD implementations present nearly identical declines in comparison to the isolated case, corresponding to the ISM contents.

The impact of the MHD physics seems more clear in the tail, where during the whole interaction the star formation rate is associated with smaller values. Combing this evidence with the higher fraction of $M_{\rm ISM}$, as is shown in Figure 3.7, we can confirm that the magnetic fields effectively affect the sustainability of the ISM in the tail. The cold clouds are resistant to mixing and dissolution to the ICM, as the magnetic draping protects the tail material against KH instabilities and thus confines the relatively cold ISM in filamentary clumps. Additionally to that, a tiny star-forming event at late times indicates that yet some eligible material is still located there. Nevertheless, the content of the star-forming gas at those times is approaching the same order of magnitude of the resolution level ($\sim 3 \times 10^5 M_\odot$), enabling us only to record this SF spike. We predict an unresolved continuous SFR profile for the MHD, whereas the HD case ceased any star-forming event due to the lack of available material (Figure 3.7). In general, comparing our results with the GASP survey (Poggianti et al., 2019a), which has gathered

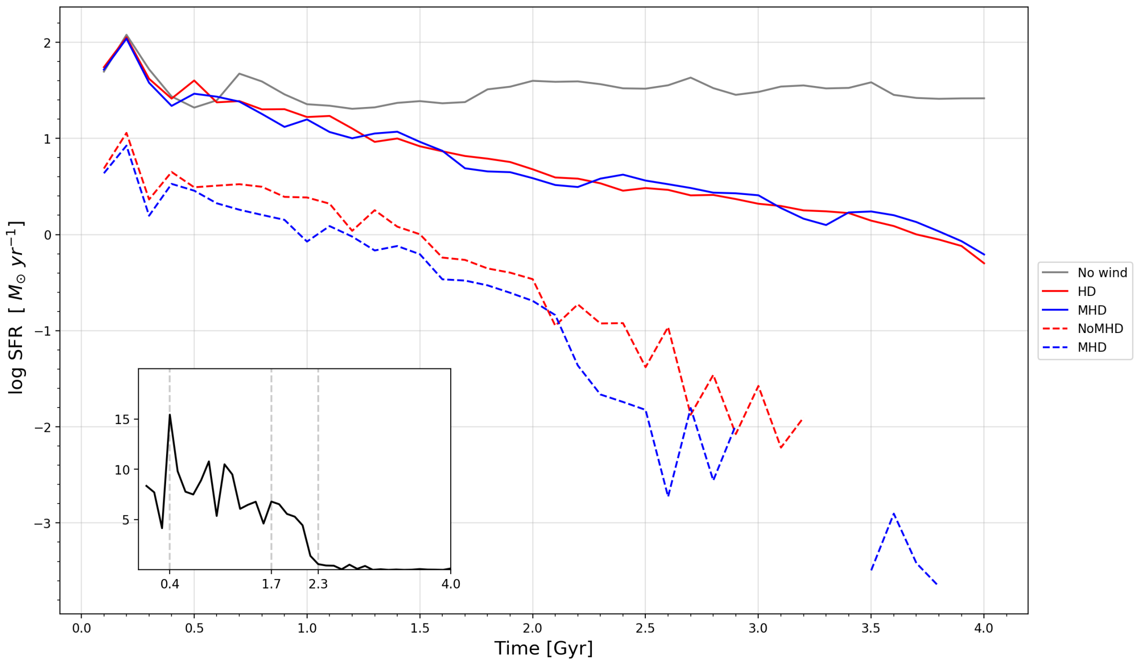

Figure 3.8: The star formation rates for the total system i.e disc + tail (solid lines) and the tail (dashed lines) for HD and MHD physics. The exerted ram pressure effectively suppresses the SFRs regardless of the presence of magnetic fields. After the encounter with the hot ICM, the galaxies present a short starburst phase which is followed by constant decline. In contrast, the magnetic fields moderate the SFR in tail as the HD run is prone to mixing events. The highest fraction of M_{ISM} and lower SFRs for the MHD physics ensure that the sustainability of the ISM clumps in the tail due to the suppression of KH instabilities. Finally, the secondary plot indicates the percentage (%) of SFR in the tail.

prominent observations of jellyfish galaxies we indeed find some similarities. The authors state that their samples with the most extended tails present 10 to 20 % of the SFR occurs in the tail. In particular, our novel example J0206 is characterized by a total SFR 5.32 $M_{\odot}\mathrm{yr}^{-1}$ with 10% contribution from the tail. We confirm this behaviour for simulation times around $t \sim 1.2$ Gyr. As the secondary figure in 3.8 demonstrates our simulation covers a range of SFR tail contributions up to 15%. This specific peak occurs corresponds to times when a global starburst occurred and is followed by a phase with a median value of 9%. The sudden drop that is noted is due to the fallback of the star-forming gas below the $2R_{1/2}$. Then, the tail SFRs fall to a secondary plateau and eventually after $t = 1.7$ Gyr adopts a passive phase which is completed at 2.3 Gyr.

As discussed in subsections 1.2.3 and 1.2.4 the ram-pressure stripping consists of a major channel of galactic quenching. The underlying quenching timescales are associated with the required

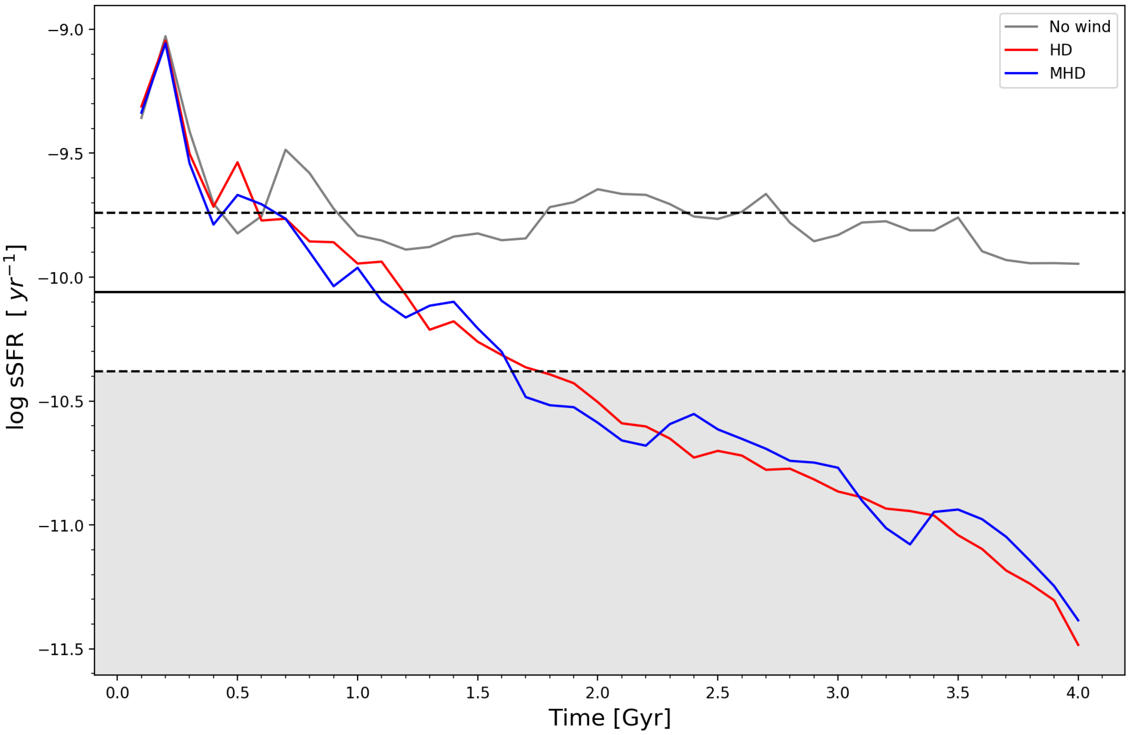

Figure 3.9: Evolution of sSFR of the three simulation runs. The value of the star-formation main sequence (black solid line) and the relative scatter (black solid line) emerged from Behroozi et al., 2013. The grey shaded area below the main sequence demonstrates the green valley galactic population. After the initial relaxation starburst signature, the no-wind case adopts an evolutionary track as a highly star-forming main sequence galaxy, whilst the ram pressure effectively drives the galaxy towards the green valley. We identify that the entrance of HD and MHD physics samples in the main sequence is associated with a short starburst event able to bring them above the main sequence.

time for a galaxy to migrate from the main sequence towards the passive green valley. This eventually will exhaust most of the star-forming gas placing the quenched galaxy on the red sequence. For this reason, we reproduce the specific star formation rate sSFR $\equiv$ SFR$M_\star^{-1}$, as a measure of the star-formation main sequence and how our simulation output deviates from it. The value of the main sequence and 0.3 dex scatter according to the initial stellar mass is obtained from Sparre et al., 2015, where authors investigate the correlation of the star formation main sequence between observational data (Behroozi et al., 2013) and Illustris simulation. Figure 3.9 shows the evolution of the sSFR for our three simulation runs and the main sequence with the relative scatter is presented with the horizontal black solid and dashed lines, respectively. The grey-shaded area below the main sequence indicates the green valley transition population (Schawinski et al., 2014). Once again, we can distinguish the influence of the ram-pressure stripping after the initial relaxation starburst at 0.3 Gyr. The no-wind galaxy preserves a nearly constant evolution at the edge of the main sequence as a highly star-forming galaxy due to initial gas fraction. For the ram-pressure cases, it seems that the SFR enhancement at 0.5 Gyr that discusses previously is quite intense, bringing the galaxies above the main sequence. Afterwards, the gas deficiency forces both cases to eventually leave the main sequence almost simultaneously at 1.7 Gyr. This quenching timescale coincides with the last significant SFRs in the tail, as we can see from Figure 3.8. Once the galaxy is established in the green valley, the tail fraction seems to decline as the refreshment of the star-forming gas is interrupted. Hence, it would be required another 0.5 Gyr to consume the remaining tail gas, until the tail reaches neglectable SFRs. Subsequently, at 2.3 Gyr the tail feature seems to fade out and most of the initial ISM gas has already been stripped and converted to stars, driving the galaxy towards the passive red sequence.

To this end, in Appendix A.1 we present the SFR evolution as a function of resolution for the MHD simulation. We compare the current high-resolution run with a nearly 17 times lower resolution counterpart. As we can see, the generalisation of low resolution leads to significantly lower SFR rates, especially when small structures account for star-forming events. This is denoted from the tail SFR profile. After $t \sim 1.0$ Gyr emerged almost an order of magnitude difference and any star-forming event ceased 1 Gyr earlier. In addition, the global SFR reveals an almost smooth decrement in comparison to the more oscillating high-resolution. This implies, that the fallback events, which naturally are small-scale instances, are not able to resolve when low-resolution simulations are employed. Subsequently, we denote the resolution importance in order to properly resolve the fragmentation processes and the cloud survival regime in the tail.

3.3 Tail evolution

In this section, we investigate the morphology and the survival scheme of the stripped gas for our simulations. In subsection 3.3.1, we find that the jellyfish tail presents long and filamentary magnetic fields aligned with the direction. Moreover given that, magnetic field morphology, we discuss how the stabilisation of KH instabilities occurs and how this is associated with magnetised gas filaments that propagate unmixed into the ICM. In subsection 3.3.2, we compare the tail surface densities for our simulations, where we find that the inclusion of MHD physics effectively modifies the survival scheme of the stripped ISM gas and the underlying fallback instances. In particular, we find that the magnetic fields facilitate the formation of a long and filamentary tail of dense ISM gas. In subsection 3.3.3, we performed a *friends-of-friends* analysis on the stripped ISM gas for our simulations. We conclude that the addition of MHD physics results in a significant acceleration of the stripped ISM clouds at greater distances and a higher degree of fragmentation, whilst the HD clouds are confined closer to the galactic disc constituting a more clumpy tail morphology.

3.3.1 Magnetic fields

In section 3.1 we briefly discussed the physical aspects associated with magnetic fields when ram-pressure stipping simulations are performed. The resulting morphology of the stripped gas is strongly affected when accounting for magnetic fields. As it is noted in Figure 3.1, the generated vortices are efficiently suppressed, when we initiate turbulent magnetised with $\beta = 50$. At this point, we will present the main physical aspects of the magnetic field, as our rich-gas galaxy experiences ram-pressure stripping at a constant rate. For the rest of this section, we mainly based on Dursi, 2007 and Dursi and Pfrommer, 2008 where the authors describe in detail the *magnetic draping* effect.

Our initial setup was constructed in such a way as to resemble the super-Alfevenic motion of the galaxy towards the potential centre of the galaxy cluster. During the infall, the galaxy sweeps up the ambient ICM magnetic field lines, constituting a magnetic layer which eventually is draped over the object. This accumulating effect occurs at the so-called *stagnation point*, which is located in front of the object along the wind direction and at which the stream lines separate. Once a steady state is reached a dynamically important sheath forms around the obstacle. The layer's strength is set by the magnetic pressure of the draping region which pushes ICM field lines downstream the galaxy at rates proportional to the accumulation of new ICM field lines in the draping layer. Hence, the magnetic energy density in the draping layer is comparable to the exerted ram pressure of the incoming wind and given by $\epsilon_B \simeq \alpha \rho_{\rm wind}^2 v_{\rm wind}^2$ with $\alpha \simeq 2$ (Dursi and Pfrommer, 2008) and completely independent of the strength of the ambient magnetic fields. In order to derive the total energy of the draping layer, we assume a sphere with radius R and volume V, which is wrapped into a draping layer of constant thickness $\ell_{\rm drape} = R/(6\alpha M_A^2)$, where M_A is the Alfevenic Mach number, over the half-sphere $A = 2\pi R^2$. Thereby, the estimated magnetic energy of the draping layer is given by:

$$E_{B,{\rm drape}} = \frac{B_{\rm drape}^2}{8\pi} \, A \; \ell_{\rm drape} = \frac{1}{2} \epsilon_{B,{\rm wind}} \; V \ ,$$

proportional to the energy density of the ambient cluster field and the volume of the obstacle or in our case the galaxy. This derivation is the"Archimedes principle of magnetic draping". As the magnetic layer is thin, the steady state is generally achieved fast with a timescale proportional to the crossing time of the half-sphere.

Once a steady state has reached, a thin draping layer of thickness $\ell_{\rm drape} \simeq 15$ pc is formed. The magnetic field lines that constitute this magnetic layer are initially in a narrow tube of radius proportional to the $p_{\rm crit} = R/(2M_A)$ from the stagnation line, while the rest of stream lines are deflected away from the galaxy. This way, the magnetic draping layer acquires a steady shape around the jellyfish, as the relative timescale for magnetic lines that enter the layer is nearly ten orders of the galactic crossing time. It turns out, that the thin magnetic draping layer could provide an efficient "magnetic shielding" on the galactic stipped from the ICM. As discussed in subsection 3.2.1 the two gas phases present a temperature difference over three orders of magnitude, which portends that the evaporation events would significantly affect the survival timescale of the stripped clouds. However, the impact of the draping layer could modify this scheme, in favour of ISM clouds survival. This is due to the exerted magnetic tension from the magnetic draping layer on the moving substructures, which stabilizes the surface modes of the

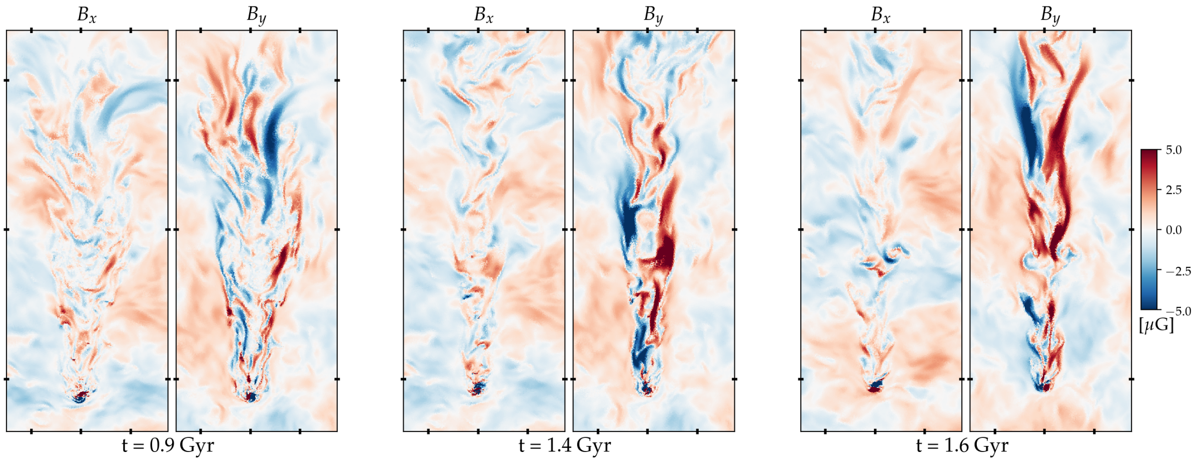

Figure 3.10: The gas magnetic field B_x and B_y projected on the $x-y$ midplace. Each panel shows the average of 14 layers of thickness $dz = 0.03$ kpc around the centre of z axis. The magnetic field morphology reveals filamentary magnetic tails, aligned with the direction of the wind. The B_y amplification occurred due to the stretching of the draped magnetic lines and the stripping of magnetised galactic material. Overall, such configuration exerts significant magnetic tension in the tail and therefore suppresses small-scale hydrodynamical instabilities (more significantly KH) parallel to the magnetic field.

KH instabilities. Modes with wavelength $\lambda \leqslant 10\ \ell_{\text{drape}}$ are stabilised against KH instabilities, implying that weaker ICM winds stabilise smaller scale modes, whilst larger modes can still be unstable in line with prior theoretical work (Chandrasekhar, 1961). This allows the extension of the survival time of the cold gas clouds, as the radiative cooling could overcome the instabilities (Gronke and Oh, 2018; Sparre et al., 2020). Supplementary to that scheme, we refer the reader for further details on how the provided magnetic tension regulates the hydrodynamical instabilities to Berlok and Pfrommer, 2019, where the authors investigate the impact of high β magnetic fields on the cylindrical cold streams.

Considering these factors, Figure 3.10 presents the projection slices of the $x-y$ midplane showing B_x and B_y. The representative projection times are selected after the magnetised wind passage across the y axis of the simulation volume. As discussed in subsection 3.2.1 the outside-in gas stripping from the galaxy is occurred due to the ram-pressure (where we identify a timescale 0.9 Gyr) and continuous gas dragging due to KH instabilities proportional to the stripping radius. Once, the ISM is detached from the disc, KH instabilities act on the boundary layers between the substructures and the ambient gas, triggering an erosion of the stripped ISM clouds. The magnetic morphology in our simulations reveals a more enhanced B_y value in the wake of the jellyfish than the toroidal component (we confirm that the B_z presents similar values to B_x) as draped field lines are stretched along the wind direction. It is clear a tendency of magnetic filaments formation, which become even more evident, especially after the stripping timescale (middle and right panels). Such a magnetic field morphology inhibits the growth of KH instabilities parallel to the field via magnetic tension. This has an essential impact on the tail vortices (Figures 3.1 and 3.2) and the subsequent mixing events of the gas clouds with the ambient gas. As pointed out by Tonnesen and Stone, 2014 gas within the magnetised filaments is propagated unmixed to larger distances from the disc. Moreover, similar to Ruszkowski et al., 2014, we also confirm the presence of double magnetic morphology, as the tail magnetic field is seeded from the draping of the ICM wind and the magnetised disc material which stripped containing the galactic spin vector. This is quite an interesting aspect, as the authors did not include galactic magnetic fields, justifying the enhanced B_y in our simulations. Those magnetic filaments appeared aligned with the wind flow, in line with radio emission observations of J0206 (Müller et al., 2021a) and JW100 (Ignesti et al., 2022).

3.3.2 Surface density

In the previous section, we explored the spatial reallocation and the underlying star formation activity of the ISM gas due to the ram-pressure stripping. In addition, we denoted the importance of MHD physics, which provides shielding for the stripped gas against KH instabilities and hence evaporation into the hot ICM. This implies the formation of a long gas tail structure downstream of the galaxy, where especially in the MHD physics case stars continue to form at a significant rate. Typically, the accurate tracking of the multi-phase stripped gas is a quite complicated task, as the thermal evolution of the detached clouds is subject to mixing and dissolving with hot ICM. The exact survival scheme of the stripped is strongly affected by the ambient environment properties, since if certain conditions are met is possible the tail clouds to experience a growth regime due to the net accretion of hot gas to the cold tail (Sparre et al., 2020). In the current subsection, we will focus on the tail gas morphology and how the presence of magnetic fields modifies it. Moreover, we maintain the same separation criteria for the ISM gas based on the temperature-density cut as described in subsection 3.2.1 and we assume that every ISM gas particle outside $2R_{1/2}$ is part of the tail (see subsection 3.2.2).

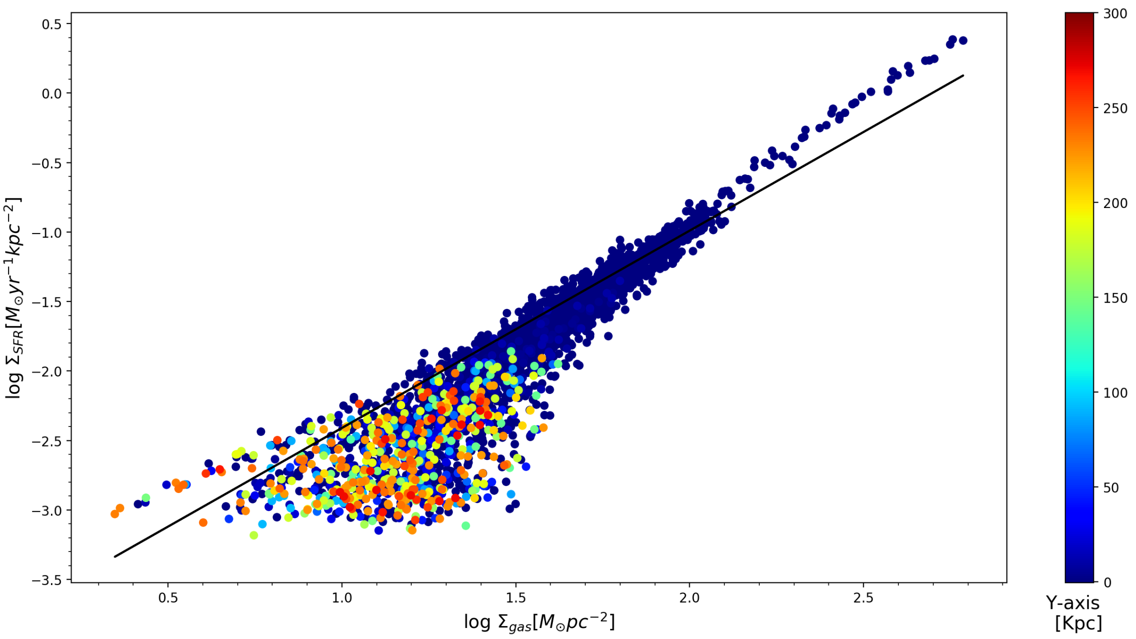

Figure 3.11: The Kennicutt-Schmidt phase diagram for the entire jellyfish galaxy at 1.3 Gyr. The black line represents the observational relation obtained from Daddi et al., 2010 and the color of each point corresponds to the distance from the galactic center in the $y - axis$. The inner disc clouds follow the tight star formation relation, while the tail clouds reside in the wider less SFR-efficient ”cluster”. The difference in surface densities between the disc and tail gas clouds follows their underlying SFR fraction.

Before we proceed to the surface density of the tail region, a global picture of the entire jellyfish galaxy is shown in Figure 3.11. This is a typical Kennicutt-Schmidt phase diagram (Schmidt, 1959; Kennicutt, 1989), which was initially used to establish the empirical power law between the SFR surface density and total gas surface density. The figure presents the jellyfish state at $t = 1.3$ Gyr, as at those times our simulation properties resemble the observables of JO206 as discussed in subsection 3.2.3. The surface densities are obtained through bin analysis of spherical slices with thickness 200 pc on the $x - y$ plane and afterwards coloured according to their position on the $y - axis$, which is the direction of the wind. The solid black line follows the observational Kennicutt-Schmidt relation for a variety of observational targets including spiral and starburst galaxies, as reported from Daddi et al., 2010. It is not a surprise that the majority of the inner gas disc regions are located in the upper right area of the plot, since the mean SFR of the disc is over an order of magnitude greater than the tail’s (Figure 3.8). Most of the stripped gas clouds cover a range of an order of magnitude for both surface densities, without following any particular distance correlation. However, it is noticeable that some of them are identified as highly star-forming, over the Kennicutt-Schmidt relationship. Generally, the same distinction feature between the inner and outer regions is observed for typical main sequence spirals, but with the latter to be associated with smaller SFR surface density (Bigiel et al., 2008). In our case, the stripped gas in the wake of the galaxy still follows the star-formation law, indicating that indeed the galactic ISM almost maintain its internal properties. The direct comparison with the observational results of JO206 is not quite reliable, as both our simulations and the observations are sensitive to the resolution of the acquired data. Nevertheless, H_I observations (Ramatsoku et al., 2019) reveal similar distribution across the phase diagram and most important the same order of magnitude difference between the disc and tail gas.

Figure 3.11 offers only a static glimpse into the spatial distribution of the SFR surface density. The chosen time (1.3 Gyr) coincidences with the passage from the main sequence (as it can be seen in Figure 3.9). Either earlier or later times would alter the distribution with the phase plot according to the starburst or quenched counterparts. To perceive the actual evolution of the tail we present Figure 3.12. At each panel of this plot is shown a 2-D histogram of $\Sigma_{\rm SFR}$ on the $x - y$ *axis* for the entire jellyfish up to 350 kpc and the underlying 1-D SFR only for the tail gas ($r > 2R_{1/2}$) across the wind direction, ensuring that the bin size is equal. Currently, we are restricted to this range in order to highlight the propagation of star-forming gas towards the tail, which significantly weakens after 350 kpc. The four rows illustrate a continuous time evolution from 1.0 to 1.3 Gyr for the MHD and HD implementations in the first and second columns respectively.

From a dynamic point of view, the selected snapshots represent an intermediate evolution of the jellyfish, as a significant amount of ISM gas has already been stripped by 1.0 Gyr. It is evident that some of the tail material is gravitationally bound to the parent galaxy inducing a fallback cycle of star-forming gas. Inspecting the spatial evolution of the star-forming gas for both cases, we could identify that clouds located below roughly 100 kpc are accelerated towards the galaxy. Once these clouds would approach the galactic disc at a later time, that is, $t = 1.3$ Gyr, some further extrinsic pressure is exerted on the pre-located disc gas. This would cause the stripping radius to experience a short decrement phase (see Figure 3.5 at $t = 1.3$ Gyr), in order for the

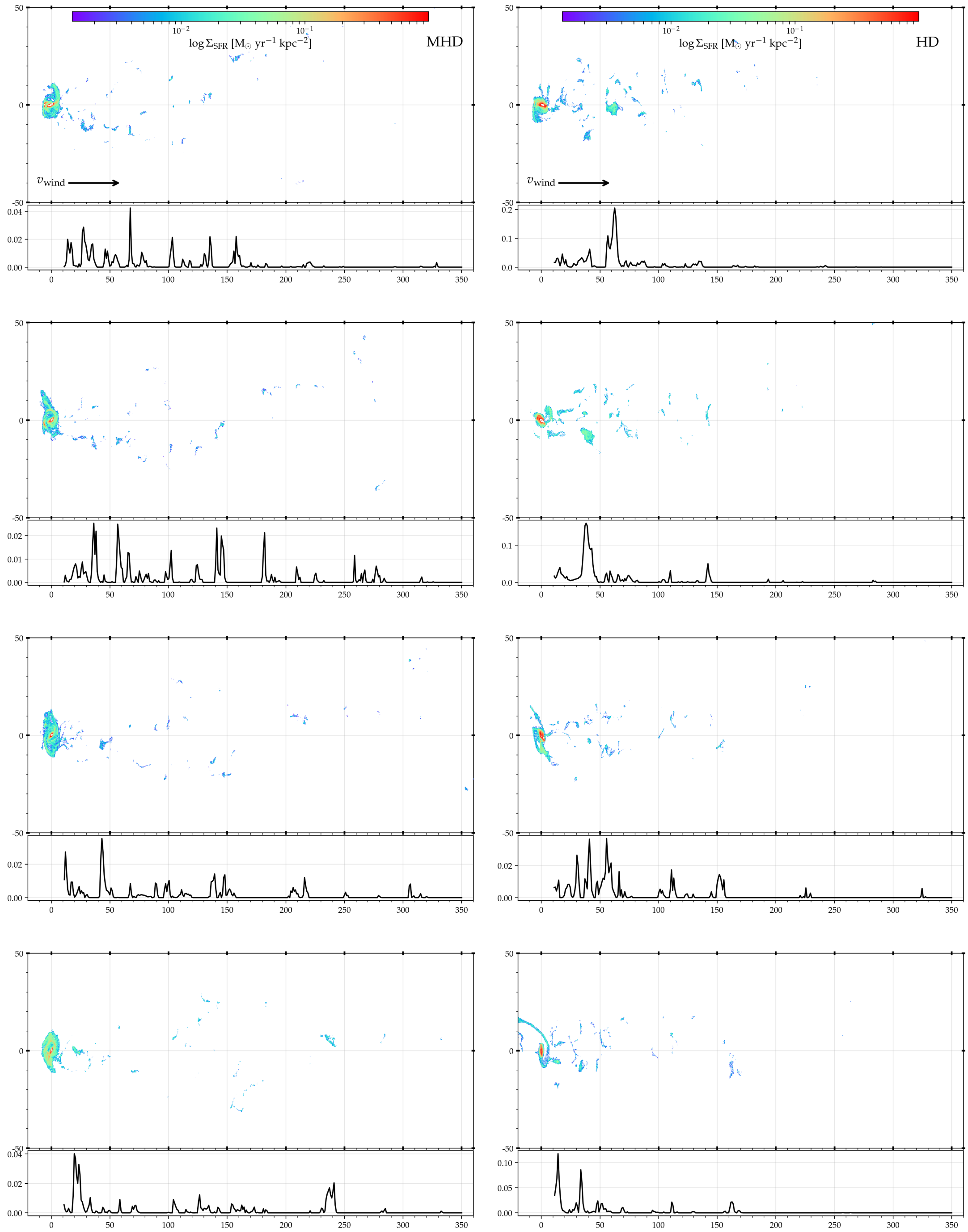

Figure 3.12: The surface density of SFR projections up to 350 kpc and the underlying tail gas SFRs of each bin across the y axis. Each column presents the MHD and HD implementations, while the rows cover a time range from 1.0 to 1.3 Gyr. The MHD stripped gas is associated with larger dispersion along the wind direction and a higher rate of fragmentation. While in the case of HD, the stripped gas is more prone to aggregation, driving larger-scale clouds to fall back into the disc. The impact of the fallback cycle seems to be regulated by the presence of the magnetic sheath, as the magnetic pressure stabilises the infalls, condensing the disc gas and thus increasing the disc's SFRs.

pressure equilibrium to be satisfied. In its turn, the $R_{\rm str}$ shrinkage would drive a new, however weaker fallback cycle, as new gas disc gas is exposed to the wind. These fallback cycles seem to be strongly correlated with the presence of magnetic fields. Probably, this is happening as the magnetised wind is draped around the galactic front. The magnetic sheath around the galaxy provides magnetic pressure proportional to the ram pressure on the infalling material and hence confines it closer to the galactic centre. This becomes clear if we visually compare the HD gas movement in the second column of the plot. We can see that a large star-forming cloud is in collision orbit, which eventually falls within the galaxy at 1.3 Gyr. The results of the crush are quite intense for the disc, which is heavily disrupted and even produce tidal torque morphology able to move a significant amount of ISM gas in front of the galaxy (Figure 3.7). While in the case of MHD, the spatial limitation which emerged from the magnetic tension of the draped sheath is related to the compression of star-forming gas and thus higher SFRs. This can be seen at $t = 1.3$ Gyr (e.g when the fallback cycle is completed), where the colour gradient indicates higher SFR surface density. Moreover, this signature is apparent in the general SFR evolution (Figure 3.8) every time a fallback cycle took place.

Generally, the gas in the HD run seems to be more prone to the induced vortices from KH instability, mixing and eventually evaporation in the hot ICM. The physical aspect that regulates the survival of the cold clouds as they accelerated from the hot wind is the cooling time. In particular, when the radiative cooling timescale is sufficiently short in comparison to the time scale of hydrodynamical instabilities (most notably the KH instability), the clouds could propagate and thus accelerate across the tail direction (Gronke and Oh, 2018; Sparre et al., 2020). Back to figure 3.12, the HD physics implementation is not only associated with larger scale fragments but also with a more restricted radial distribution. This becomes clear from the SFRs as a location proxy of the ISM gas, where most of the clouds are evaporated at roughly 150 kpc. On the other hand, a more extended scheme is evident when a magnetic field is included. The ISM clouds reveal an isolated evolution from their environment, which is defined as long and less star-forming (Figure 3.8), favouring the sustainability of the stripped clouds.

3.3.3 Tail clumps morphology

In the previous subsection, we found that magnetic fields are able to alter the physical properties of the jellyfish tails. As already commented in subsection 3.2.1 the MHD indeed presents a higher mass fraction in the wake at later times, however, within the ram-pressure timescale the ISM stripping rate is almost identical for the MHD and HD cases. Hence, the exact tracking of the ISM material after detached from the galaxy could provide an alternative perspective. Nevertheless, it is a quite challenging task because the evolution of ISM clumps is far from linear. In the early phase, the clumps are stripped massively and thereafter they are shattered into substructures due to the encounter with the ambient ICM. This implies that the intrinsic properties of those clouds continuously change, which makes any density or mass tracking criterion unstable.

For this reason, we employed a friends-of-friends (FoF) algorithm (Huchra and Geller, 1982; Davis et al., 1985), which is a distance-oriented criterion for tracking particles with similar properties. Typically, these types of algorithms are widely used in dark matter simulation for identifying haloes. In our case, we will attempt to apply an FoF analysis on the ISM gas particles located in the tail, according to the adopted criteria for the ISM gas as described in subsection 3.2.1. Based on that, the FoF algorithm will identify a specific number of group particles, namely the ISM clouds, which lie in the wake of the galaxy throughout the jellyfish evolution. However, the algorithm contains a free parameter the *linking length*. We can perceive the linking length as the mean interparticle distance that is allowed for a given particle group. Larger linking lengths are associated with fewer FoF groups with a higher number of particles. Figure 3.13 illustrates this behaviour, where we can directly see the correlation between the FoF groups and their underlying mean cloud mass for a different selection of the linking length parameter. A similar FoF analysis has also been conducted at Sparre et al., 2019 to investigate the small-scale multi-phage gas structures in the wake of the stripped clouds. The authors adopted a parametrization of the linking length based on a density threshold of the connected cells. Inspired by that, in the current work we initialize the FoF analysis only for the cold ISM gas and maintain a constant linking length during the simulation. Generally, observational surveys of J0206 suggest that the typical mean mass of the clouds in the tail is approximately $4 \times 10^4 M_\odot$

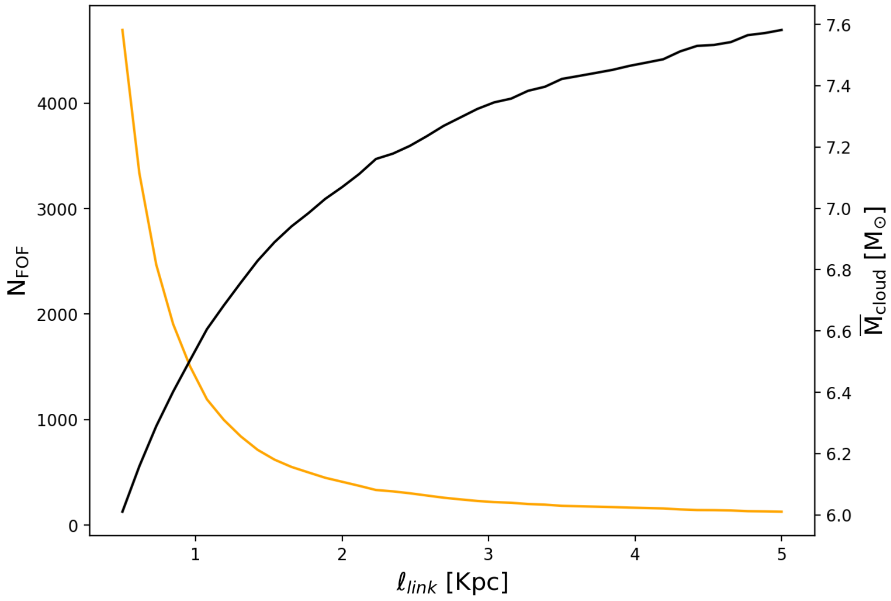

Figure 3.13: The correlation for the number of FoF groups and the mean mass of each group for different values of the free parameter i.e *linking length*. The FoF analysis is performed only on the cold ISM clouds in the wake of the galaxy. We perform FoF evolution of the MHD and HD simulation runs in order to compare the influence of the magnetic fields in the survival scheme of the clouds, maintaining the same linking length throughout the simulation. For the rest of the analysis is adopted $\ell_{\rm link} \sim 2$ Kpc. In Appendix A.2 we show that our results are insensitive to the exact value of this parameter.

(Poggianti et al., 2019a), which is almost an order of magnitude below the resolution level of the current simulation. Thereby, the specific analysis is limited to comparing the influence of MHD physics on tail substructures with the relative HD case. Therefore, the exact number of the free parameter has a small impact on the results, as long as we don't select excessively small or large values. For the rest of the analysis, we adopted $\ell_{\rm link} \sim 1.2$ kpc, however, in Appendix A.2 we include the below results with smaller/larger values that reveal very similar behaviour.

With the FoF analysis, we will attempt to investigate the evolution of cold clouds until 2.1 Gyr for the MHD and HD physics cases. By then, the tail gas has reached very close to the edges of the simulation volume, causing some non-physical decrement in the distributions. The main aspects of FoF analysis can be seen in Figure 3.14. The adopted notation stands for the mean values with the lines for each simulation time step and the $5^{\rm th}$ to $95^{\rm th}$ percentiles with the dashed regions. The *first row* presents a quantification test of the FoF algorithm on the grouping process of the stripped ISM clouds. We note that spatial distribution and the enclosed mean mass of each FoF group are directly correlated with the initial free parameter of the algorithm since the

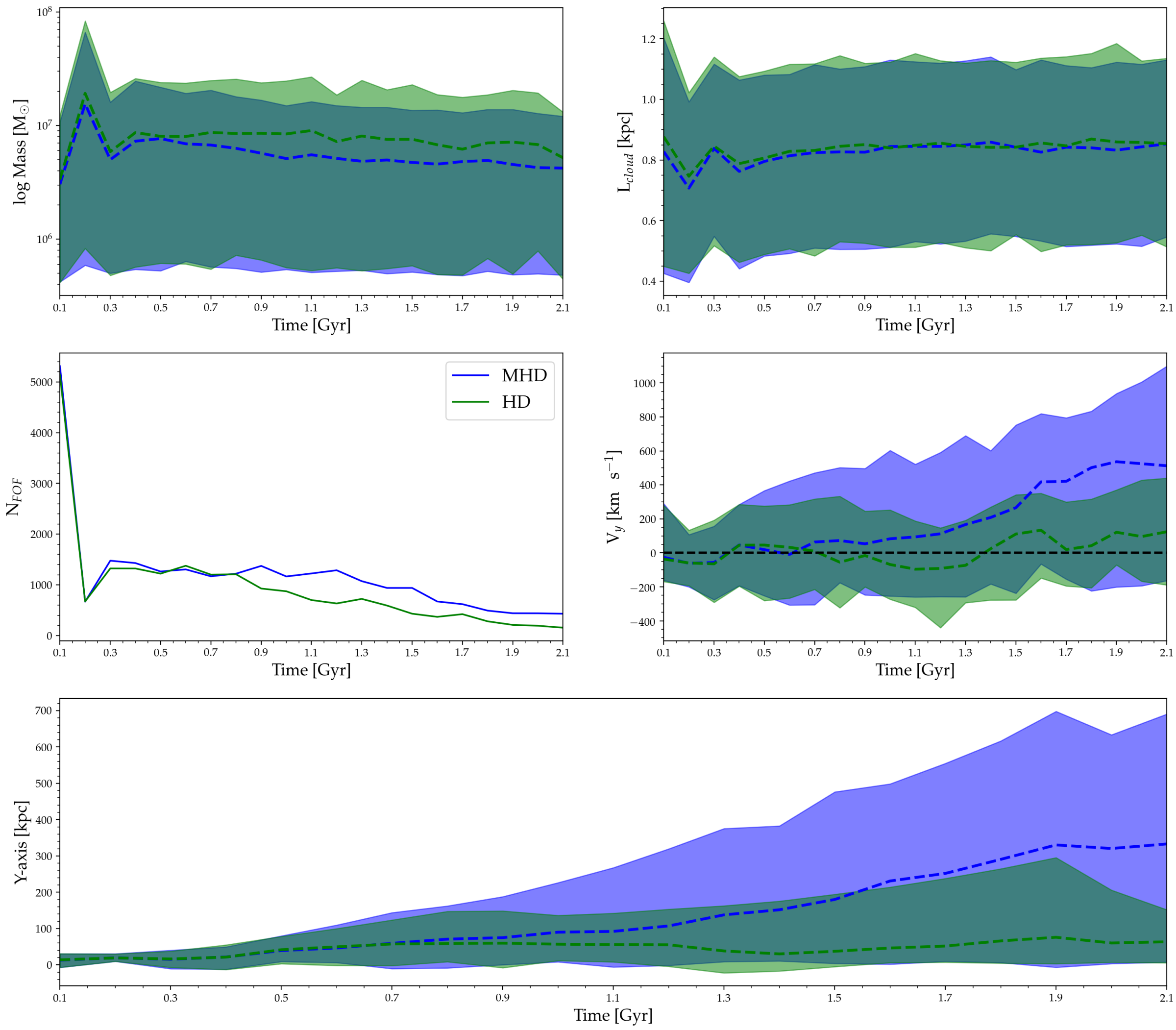

Figure 3.14: FoF analysis of the stipped ISM clouds in the tail. At each panel, the line indicates the mean values at given times and the shaded region stands for the $5^{\text{th}} - 95^{\text{th}}$ percentiles. The panels present the mean mass and size of the clouds, relative to adopted linking length $\ell_{\text{link}} \sim 1.2$ Kpc(top row). The number of employed FoF groups or equivalently the cold-dense clouds and the velocity in the wind direction (middle row) and the distance from the disc (bottom), which is the main outcome. The MHD tail clumps transferred at greater distances due to the magnetic draping of the magnetic field lines of the wind. The exerted magnetic tension in those clouds supports the survival regime, whilst in absence of magnetic fields the clouds evaporate in shorter timescales and tend to collapse each other producing more intense fall-back instances.

adopted linking length regulates the separation degree of the stripped clouds. This is clear from the constant evolutionary behaviour of the mean length of the clouds which is calculated from $L_{\text{cloud}} = (3V/4\pi)^{1/3}$, with V is the cell's volume that constitutes the FoF cloud. The relatively constant cloud size and the fact that MHD clouds are described by smaller mean mass imply that MHD tail clouds are associated with more intense fragmentation. This signature is even more evident from the number of employed FoF groups throughout the simulation. The number of cold clumps in the tail follows a similar evolution until the times of stripping timescale and thereafter it seems that the HD clouds are evaporated and dissolved faster into the hot ICM wind. On the other hand, when a magnetised turbulent wind is included the number of ISM clouds is preserved more efficiently before eventually mixed into the wind. This occurs as the ICM magnetic field lines are wrapped around the galaxy and stretched along the $y-axis$. In subsection 3.3.1, we identify the impact of the long filamentary magnetic tail on the survival scheme of the stripped clouds, as the exerted magnetic tension of those filaments effectively suppresses the KH instabilities. The resulting cloud fragmentation resembles the recorded ISM mass in the tail, as seen in Figure 3.7. ISM mass in the tail is attributed to smaller-scale clouds that are resistant to mixing with the hot ICM, as the magnetic shielding enables a more isolated evolution in terms of gas diffusion.

The general conclusion of how the exerted magnetic tension affects the tail clumps evolution is summarized in the travelled distance along the wind direction panel of Figure 3.14. It is clearly illustrated the sustainability of the stripped clouds under the presence of magnetic fields, as the ISM gas has transported to greater distances in comparison to the HD analogue. At earlier times, below the stripping timescale, both cases indicate similar extending in the $y-axis$. This profile is radically changed at later times. While most of the HD gas is tracked at closer distances to the galaxy as it is heavily affected by evaporation, the MHD clouds record significantly wider entrainment to greater distances. In fact, the differentiation is so intense that the maximum scatter of HD clouds goes below the mean value of MHD. This leads naturally to a notable increase in the velocity due to momentum transfer from the surrounding ICM wind. These findings are in agreement with prior works, where the authors commented on the acceleration of the stipped cloudlets when magnetic fields are included (Gronke and Oh, 2018; Sparre et al., 2020; Cottle et al., 2020). Those clouds are stretched along the magnetic field lines, which facilitates the formation of a long filamentary tail composed of cold star-forming gas in the wake of the galaxy.

Furthermore, a secondary effect is displayed in the velocity panel of Figure 3.14. While both

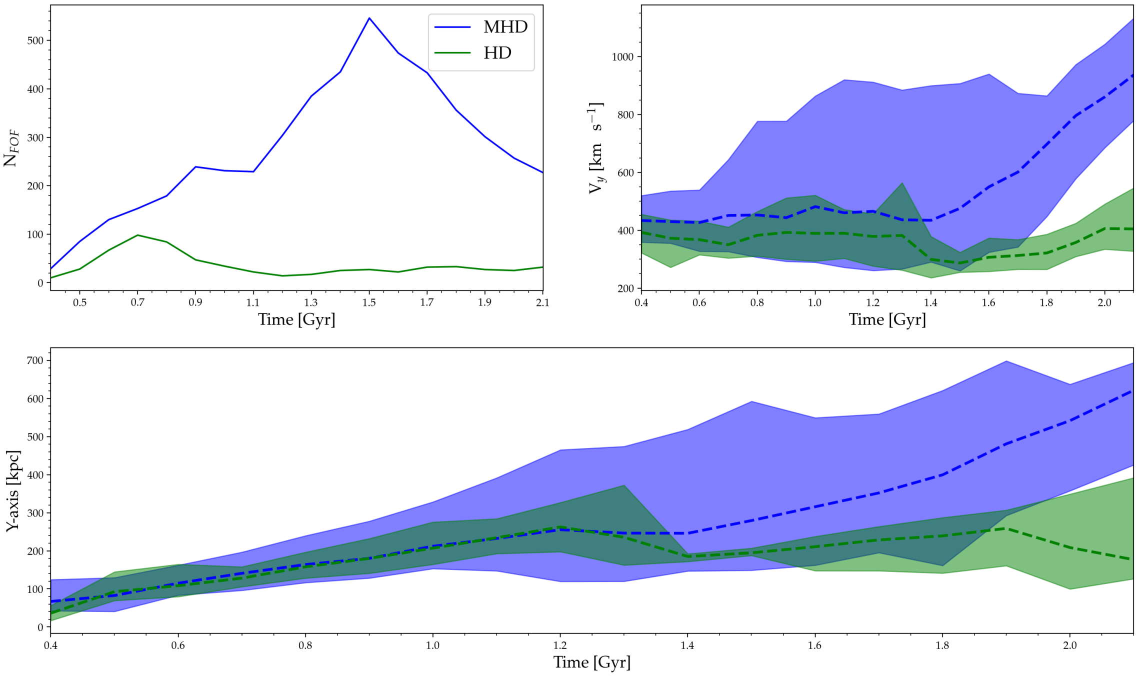

Figure 3.15: An analogue of 3.14 for ISM clouds that are not bound to the potential of the galaxy. When the fall-back cases are neglected the survival scheme becomes even more clear, as the unbound magnetised clouds accelerated close to the wind speed.

cases denote clouds that move with negative velocities, this effect presented much more enhanced for the HD tail, which appears mean values very close to zero or even below it. The oscillation profile is attributed to fall-back cases, where the minimum scatter is recorded just before the most intense fallback instance $t \sim 1.3$ Gyr. As Figure 3.12 demonstrates such instances are occurred due to massive HD tail clumps that were formed from smaller stripped fragments. Notably, it is important to not confuse these "back-and-forth" movements with higher mass feeding of the disc, as thereafter the stripping timescale, the MHD disc always maintains larger $M_{\rm ISM}$ (Figure 3.7), highlighting the importance of the evaporation. As also noticed in Tonnesen and Stone, 2014 the inclusion of magnetic fields causes a higher mass of stripped gas to fall back into the disc. Generally, this phenomenon reveals that HD gas clouds are prone to aggregation, whilst in the case of MHD the exerted magnetic tension fragment the clumps into smaller sub-clouds, that are efficiently accelerated. A more theoretical view of this effect is presented in Ji et al., 2018, where the authors conclude that the magnetic pressure can also alter the dynamics of shattering by suppressing the internal gravity waves on an overdense filament.

Finally, in Figure 3.15 we show an analogue of the survival scheme, neglecting the fall-back cases and focusing only on ISM gas that is bound to the galactic potential. Indeed, the unbound gas highlights the survival scheme of the MHD gas. As discussed previously, the addition of magnetic fields is associated with a higher degree of cloud fragmentation, defining a more unmixed evolution. Moreover, the magnetic tension efficiently suppresses the KH instabilities, enabling the clumps to travel at greater distances with velocities close to the co-moving speed of the wind. The spatial difference between the two cases is remarkable, as the unbound MHD gas is able to survive until eventually reaches the simulation volume edge. On the other hand, the KH instabilities dissolve the ISM clouds into the ICM wind. The tail morphology when magnetic fields are not included is much more spatial limited, and more clumpy driving larger-scale stripped gas clouds to fall back in the disc.

Chapter 4

Discussion

Ram pressure stripping offers a unique physical window to study the quenching scope of galactic evolution and the involved smaller-scale hydrodynamical physics effects that lead to the gas reservoir exhaustion. Observational surveys, part of the GASP mission (Poggianti et al., 2019a and Poggianti et al., 2019b and references therein) reveal rich morphological properties of jellyfish galaxies with multi-wavelength signatures, providing several star-formation traces for the stripped gas. In particular, the jellyfish tails are composed of an extended spatial distribution of neutral gas where within are embedded star-forming clouds. The gas clouds present a variety of CO, UV and H_α emissivities reflecting the evolutionary sequence of star-forming regions, as these clouds are associated with emission combinations as a function of their distance from the disc. Local post-starburst signatures suggest that the gas stripping occurs outside-in (Vulcani et al., 2020), which in total results in the observed jellyfish tails that cover distances nearly to 100 kpc.

We find good agreement between our simulations and observational features. While the employed subgrid ISM model does not allow to explore whether the tail substructures contain molecular gas, however, we clearly show that the tail structure is indeed associated with in-situ star formation events. The spatial distribution of the star-forming clouds even exceeds the 100 kpc and the recorded SFR tail fractions match the observations. We also indicated the impact of the magnetic fields, as the magnetised tails favour the survival scheme of the stripped ISM clouds. In this regime, stripped ISM gas seems to be resistant to mixing events, facilitating the formation of a long filamentary tail. Recent radio observations (Müller et al., 2021a; Ignesti et al., 2022) claim that such configuration is necessary for the holistic view of the evolution of galaxies experiencing ram-pressure stripping. Based on that, in the following paragraphs, we mention some future extensions of the current simulations that might offer more insights into jellyfish evolution.

Inclusion of a black hole : Our simulations predict that a large amount of the stripped gas remains gravitationally bound to the galaxy, driving fallback episodes. The magnetic pressure from the magnetic sheath at the leading edge seems to confine the resettling of the fallback gas within the disc and further compress the pre-located galactic gas. This phenomenon was also confirmed by other MHD simulations (Tonnesen and Stone, 2014; Ramos-Martınez et al., 2018), where the authors also found an enhanced ISM gas presence around the disc due to the fallback funnelling. We conjecture that this feature is linked with the final burst of star formation in SOs galaxies observed in the central regions (Johnston et al., 2014) and the higher bulge-to-disc ratios, as the stripped gas requires some Myr to complete a fallback cycle.

A natural question which arises is how the presence of a central black hole would respond to the simultaneous stripping and fallback cycle. Large observational surveys (Schawinski et al., 2014) based on color phase diagrams demonstrate that green-valley galaxies are associated with higher AGN activity which is triggered as an after-effect of quenching. Similar results were also released from the GASP mission (Poggianti et al., 2017b), finding that the great majority of ram-pressure stripped galaxies host an AGN (Seyfert 2). This could provide another source of feedback, suggesting that ram pressure is not only stipping the outskirts of the disc but also is associated with significant gas accretion able to ignite an AGN. The authors speculated that the angular momentum losses of the disc gas due to interaction with the non-rotating ICM might be responsible for gas inflows, however more research is needed. On the other hand, magnetic fields indicate that efficiently protect the stripped gas from evaporation into ICM, which thereafter a significant amount is funnelled back to the disc. In that sense, the accretion rate towards the galactic centre could trigger the AGN, enabling a second quenching channel. To date, no jellyfish simulation with a central black hole has been conducted. Hence, it would be quite essential for the field to simulate such a scenario.

Dynamic wind model : Our simulation setup is based on a static wind model with constant properties similar to ICM of JO206 (see section 2.2.2 for more details). However, a more accurate simulation of a satellite galaxy should account for a time dependent ram pressure, according to the galactic orbit within the cluster. As Tonnesen, 2019 noted, a wind strength varying with time could exert less dramatic results in the stripping process in comparison to the continuous case. Our simulation architecture provides the flexibility to include a dynamic wind, as a modification in the injection region properties according to the cluster mass density distribution and the underlying galaxy velocity would mimic a more realistic ram pressure.

Mock Observations : While the current simulations reproduce the main physical aspects that emerged from radio observations of J0206 (Müller et al., 2021a), it still remains some research to be done. In particular, the authors presented measurements for the spectral index α and the fractional polarisation for the disc and the tail regions. They found that the spectral index within the disc (≈ -0.7) is slightly steeper than the expected values of star-forming regions, in comparison to the tail profile (≈ -2.0). In the tail, the spectral index steepens with distance from the disc of the galaxy, implying significant radiative ageing of electrons that were initially produced in high energetic phenomena such as SNs. The fractional polarisation, which indicates a measure for the uniformity of the magnetic field (or equivalently the suppression of turbulent motions), reveals an ordered tail magnetic field aligned with the infall direction with a fraction around 55%. Further study on the radio observables was conducted by Müller et al., 2021b showed that the observed fractional polarisation plateaus along the tail are correlated with turbulent re-acceleration of the electrons that were initially accelerated by the central AGN. Hence, it would be valuable to further investigate the radio emission from jellyfish galaxies by reproducing radio mock observations. In addition, there is a growing body of literature regarding the nonthermal pressure contribution to the formation and evolution of galaxies (Pfrommer et al., 2017; Pfrommer et al., 2022). Cosmic rays in isolated galaxy models exert an important pressure component to the ISM, shaping an increased vertical scale height of disc galaxies and counteracting the condensation of gas to star-forming densities and hence suppressing the global SFRs. Farber et al., 2022 investigate the case and found that cosmic rays modify the gas phase distribution, supporting the presence of cold-dense gas. Moreover, it was noted that the number density of cosmic rays and the magnetic fields appeared more enhanced in jellyfish galaxies compared to the isolated counterpart, indicating elevated radio emission as observations suggest.

Chapter 5

Conclusions

In this thesis, we have investigated the impact of ram pressure stripping on a galaxy as infalls into a galaxy cluster. We have employed high-resolution wind tunnel experiments using the moving-mesh code AREPO combined with a special refinement strategy, according to the observables of jellyfish galaxy JO206. Through this setup, we performed a magnetohydrodynamic run where a magnetised turbulent wind is injected into a magnetised galaxy, a hydrodynamic counterpart and finally an isolated case without wind. All simulation runs emerged from identical initial conditions, particularly a gas-rich multi-phase galaxy with edge-on orientation along the direction of the wind. Throughout the thesis, we analysed how magnetic fields affected the ram pressure stripping process and the underlying response of the stripped gas. Our main conclusions are listed below:

- In general, the stripping process can be subdivided into two classes, the ram pressure pushing and the continuous gas dragging from the outskirts of a disc due to KH instabilities. Both simulations show an "outside-in" stripping, leading to a stripping radius below the half-mass stellar disc at nearly 1 Gyr, in agreement with prior considerations of the intermediate ram-pressure timescales. During this time, the ISM mass losses from the parent disc are estimated to be 60% of the initial ISM mass and present a similar decrease, regardless of the presence of magnetic fields, implying a weak impact on the stripping process. However, at later times the jellyfish galaxy reveals higher ISM gas within the stellar disc and in the tail.

- The edge-on orientation indicates a short SFR starburst phase 0.2 Gyr after the wind encounter. This incident is able to disrupt the quenching evolutionary track, temporarily bringing the galaxy above the main sequence. This would further exhaust the star-forming gas, leading the galaxy towards the green valley at 1.7 Gyr. The transition to the green valley population coincides with the last significant tail/disc SFRs fractions, indicating a global quenching of the system.
- During entrainment, the MHD stipped gas reveals great sustainability, as the magnetised tail is associated with higher ISM mass and lower SFRs in comparison to the HD analogue. This is due to the magnetic draping of the ICM over the galaxy. The magnetic field lines aligned with the direction of the wind exert magnetic tension on the tail gas clouds, thus stabilizing small-scale turbulent motions such as KH instabilities. Hence, the stipped ISM gas is effectively shielded against the hot ambient wind, inhibiting mixing events and dissolution of the cold tail clouds.
- The remaining perturbed disc experiences significant ”fallback cycles”, as gravitational potential pulls back the stripped ISM gas to the disc. The signatures of this process are evident in the amplifications of the stripping radius and resulting mass contained within the galactic disc. Overall, the spatial limitation of the inflows within the stellar disc emerged from the magnetic pressure of the draped sheath front, further compressing the pre-located star-forming gas and triggering small-scale star formation bursts. In the absence of magnetic fields, the stipped gas accumulated in larger-scale clouds in the tail, leading to tidal torque morphology in front of the disc.
- The addition of magnetic fields changes the morphology and survival scheme of the stripped ISM clouds. In contrast to the hydrodynamic analogue, the MHD tail gas is more prone to fragmentation constituting smaller-scale clouds, which however maintain their intrinsic star-forming morphology. These clouds are accelerated to greater distances, leading to the formation of an elongated, long-lived filamentary tail.

References

Abazajian, Kevork N. et al. (2009). The Seventh Data Release of the Sloan Digital Sky Survey. 182, p. 543. arXiv: 0812.0649 [astro-ph].

Agertz, Oscar et al. (2007). Fundamental differences between SPH and grid methods. 380, p. 963. arXiv: astro-ph/0610051 [astro-ph].

Alatalo, Katherine et al. (2015). Suppression of Star Formation in NGC 1266. 798, 31, p. 31. arXiv: 1410.4556 [astro-ph.GA].

Athanassoula, E. (1992). Morphology of bar orbits. 259, p. 328.

Baldry, Ivan K. et al. (2004). Quantifying the Bimodal Color-Magnitude Distribution of Galaxies. 600, p. 681. arXiv: astro-ph/0309710 [astro-ph].

Barnes, Josh and Hut, Piet (1986). A hierarchical O(N log N) force-calculation algorithm. 324, p. 446.

Behroozi, Peter S. et al. (2013). The Average Star Formation Histories of Galaxies in Dark Matter Halos from z = 0-8. 770, 57, p. 57. arXiv: 1207.6105 [astro-ph.CO].

Bekki, Kenji (2009). Ram-pressure stripping of halo gas in disc galaxies: implications for galactic star formation in different environments. 399, p. 2221. arXiv: 0907.4409 [astro-ph.CO].

Berlok, Thomas and Pfrommer (2019). The impact of magnetic fields on cold streams feeding galaxies. 489, p. 3368. arXiv: 1904.02167 [astro-ph.GA].

Bigiel, F. et al. (2008). The Star Formation Law in Nearby Galaxies on Sub-Kpc Scales. 136, p. 2846. arXiv: 0810.2541 [astro-ph].

Blumenthal, G. R. et al. (1984). Formation of galaxies and large-scale structure with cold dark matter. 311, p. 517.

Bode, Paul et al. (2001). Halo Formation in Warm Dark Matter Models. 556, p. 93. arXiv: astro-ph/0010389 [astro-ph].

Bond, J. Richard et al. (1996). How filaments of galaxies are woven into the cosmic web. 380, p. 603. arXiv: astro-ph/9512141 [astro-ph].

Boselli and Gavazzi, Giuseppe (2006). Environmental Effects on Late-Type Galaxies in Nearby Clusters. 118, p. 517. arXiv: astro-ph/0601108 [astro-ph].

Boselli et al. (2021). A Virgo Environmental Survey Tracing Ionised Gas Emission (VESTIGE). IX. The effects of ram pressure stripping down to the scale of individual HII regions in the dwarf galaxy IC 3476. 646, A139, A139. arXiv: 2012.07377 [astro-ph.GA].

Bower, R. G. et al. (2006a). Breaking the hierarchy of galaxy formation. 370, p. 645. arXiv: astro-ph/0511338 [astro-ph].

– (2006b). Breaking the hierarchy of galaxy formation. *Monthly Notices of the Royal Astronomical Society* 370, p. 645. ISSN: 0035-8711. eprint: https://academic.oup.com/mnras/article-pdf/370/2/645/2898993/mnras0370-0645.pdf.

Boylan-Kolchin, Michael et al. (2009). Resolving cosmic structure formation with the Millennium-II Simulation. 398, p. 1150. arXiv: 0903.3041 [astro-ph.CO].

Butcher, H. and Oemler A., Jr. (1978). The evolution of galaxies in clusters. I. ISIT photometry of Cl 0024+1654 and 3C 295. 219, p. 18.

– (1984). The evolution of galaxies in clusters. V. A study of populations since Z 0.5. 285, p. 426.

Byrd, Gene and Valtonen, Mauri (1990). Tidal Generation of Active Spirals and S0 Galaxies by Rich Clusters. 350, p. 89.

Cappellari, Michele et al. (2011). The ATLAS^{3D} project - VII. A new look at the morphology of nearby galaxies: the kinematic morphology-density relation. 416, p. 1680. arXiv: 1104.3545 [astro-ph.CO].

Carroll, Sean M. (2001). The Cosmological Constant. *Living Reviews in Relativity* 4, 1, p. 1. arXiv: astro-ph/0004075 [astro-ph].

Catinella, Barbara et al. (2013). The GALEX Arecibo SDSS Survey - VIII. Final data release. The effect of group environment on the gas content of massive galaxies. 436, p. 34. arXiv: 1308.1676 [astro-ph.CO].

Chabrier, Gilles (2003). Galactic Stellar and Substellar Initial Mass Function. 115, p. 763. arXiv: astro-ph/0304382 [astro-ph].

Chandrasekhar (1943). Dynamical Friction. I. General Considerations: the Coefficient of Dynamical Friction. 97, p. 255.

– (1961). *Hydrodynamic and hydromagnetic stability.*

Chung, Aeree et al. (2007). Virgo Galaxies with Long One-sided H scpi/scp Tails. *The Astrophysical Journal* 659, p. L115.

Clowe, Douglas et al. (2006). A Direct Empirical Proof of the Existence of Dark Matter. 648, p. L109. arXiv: astro-ph/0608407 [astro-ph].

Colless, Matthew et al. (2001). The 2dF Galaxy Redshift Survey: spectra and redshifts. 328, p. 1039. arXiv: `astro-ph/0106498 [astro-ph]`.

Cottle, J'Neil et al. (2020). The Launching of Cold Clouds by Galaxy Outflows. III. The Influence of Magnetic Fields. 892, 59, p. 59. arXiv: `2002.07804 [astro-ph.GA]`.

Cowie, L. L. and Songaila, A. (1977). Thermal evaporation of gas within galaxies by a hot intergalactic medium. 266, p. 501.

Cox, T. J. et al. (2006). The Kinematic Structure of Merger Remnants. 650, p. 791. arXiv: `astro-ph/0607446 [astro-ph]`.

Cramer, W. J. et al. (2019). Spectacular Hubble Space Telescope Observations of the Coma Galaxy D100 and Star Formation in Its Ram Pressure-stripped Tail. 870, 63, p. 63. arXiv: `1811.04916 [astro-ph.GA]`.

Croton, Darren J. et al. (2006). The many lives of active galactic nuclei: cooling flows, black holes and the luminosities and colours of galaxies. 365, p. 11. arXiv: `astro-ph/0508046 [astro-ph]`.

Daddi, E. et al. (2010). Different Star Formation Laws for Disks Versus Starbursts at Low and High Redshifts. 714, p. L118. arXiv: `1003.3889 [astro-ph.CO]`.

Darvish, Behnam et al. (2016). The Effects of the Local Environment and Stellar Mass on Galaxy Quenching to z $\sim$ 3. 825, 113, p. 113. arXiv: `1605.03182 [astro-ph.GA]`.

Davis et al. (1985). The evolution of large-scale structure in a universe dominated by cold dark matter. 292, p. 371.

Davis et al. (2011). The ATLAS3D project – X. On the origin of the molecular and ionized gas in early-type galaxies. *Monthly Notices of the Royal Astronomical Society* 417, p. 882. ISSN: 0035-8711. eprint: `https://academic.oup.com/mnras/article-pdf/417/2/882/3058967/mnras0417-0882.pdf`.

de Vaucouleurs (1948). Recherches sur les Nebuleuses Extragalactiques. *Annales d'Astrophysique* 11, p. 247.

– (1956). Luminosity Functions and Population Subtypes in the Magellanic Clouds. *Irish Astronomical Journal* 4, p. 13.

Dekel and Birnboim (2006). Galaxy bimodality due to cold flows and shock heating. 368, p. 2. arXiv: `astro-ph/0412300 [astro-ph]`.

Dekel et al. (2009). Cold streams in early massive hot haloes as the main mode of galaxy formation. 457, p. 451. arXiv: `0808.0553 [astro-ph]`.

Di Matteo, Tiziana et al. (2005). Energy input from quasars regulates the growth and activity of black holes and their host galaxies. 433, p. 604. arXiv: `astro-ph/0502199 [astro-ph]`.

Dodelson, Scott and Widrow, Lawrence M. (1994). Sterile neutrinos as dark matter. 72, p. 17. arXiv: `hep-ph/9303287 [hep-ph]`.

Dolag, K. et al. (2005). Turbulent gas motions in galaxy cluster simulations: the role of smoothed particle hydrodynamics viscosity. 364, p. 753. arXiv: astro-ph/0507480 [astro-ph].

Domainko, W. et al. (2006). Enrichment of the ICM of galaxy clusters due to ram-pressure stripping. 452, p. 795. arXiv: astro-ph/0507605 [astro-ph].

Donnari, Martina et al. (2021). Quenched fractions in the IllustrisTNG simulations: the roles of AGN feedback, environment, and pre-processing. 500, p. 4004. arXiv: 2008.00005 [astro-ph.GA].

Dressler (1980). Galaxy morphology in rich clusters: implications for the formation and evolution of galaxies. 236, p. 351.

Dressler et al. (1997). Evolution since z = 0.5 of the Morphology-Density Relation for Clusters of Galaxies. 490, p. 577. arXiv: astro-ph/9707232 [astro-ph].

Dursi, L. J. (2007). Bubble Wrap for Bullets: The Stability Imparted by a Thin Magnetic Layer. 670, p. 221. arXiv: 0706.3216 [astro-ph].

Dursi, L. J. and Pfrommer (2008). Draping of Cluster Magnetic Fields over Bullets and Bubbles—Morphology and Dynamic Effects. 677, p. 993. arXiv: 0711.0213 [astro-ph].

Ebeling, H. et al. (2014). JELLYFISH: EVIDENCE OF EXTREME RAM-PRESSURE STRIPPING IN MASSIVE GALAXY CLUSTERS. *The Astrophysical Journal* 781, p. L40.

Efstathiou, G. et al. (1990). The cosmological constant and cold dark matter. 348, p. 705.

Ehlert, K. et al. (2018). Simulations of the dynamics of magnetized jets and cosmic rays in galaxy clusters. 481, p. 2878. arXiv: 1806.05679 [astro-ph.CO].

Eke, V. R. et al. (2005). Where are the stars? 362, p. 1233. arXiv: astro-ph/0412049 [astro-ph].

Faber, S. M. and Jackson, R. E. (1976). Velocity dispersions and mass-to-light ratios for elliptical galaxies. 204, p. 668.

Fabian, A. C. (2012). Observational Evidence of Active Galactic Nuclei Feedback. 50, p. 455. arXiv: 1204.4114 [astro-ph.CO].

Fakhouri, Onsi and Ma, Chung-Pei (2009). Environmental dependence of dark matter halo growth - I. Halo merger rates. 394, p. 1825. arXiv: 0808.2471 [astro-ph].

Fall, S. M. and Efstathiou, G. (1980). Formation and rotation of disc galaxies with haloes. 193, p. 189.

Fang, Jerome J. et al. (2018). Demographics of Star-forming Galaxies since z $\sim$ 2.5. I. The UVJ Diagram in CANDELS. 858, 100, p. 100. arXiv: 1710.05489 [astro-ph.GA].

Farber, Ryan J. et al. (2022). Stress-testing cosmic ray physics: the impact of cosmic rays on the surviving disc of ram-pressure-stripped galaxies. 512, p. 5927. arXiv: 2201.04203 [astro-ph.GA].

Faucher-Giguère, Claude-André et al. (2009). A New Calculation of the Ionizing Background Spectrum and the Effects of He II Reionization. 703, p. 1416. arXiv: 0901.4554 [astro-ph.CO].

Feng, Jonathan L. (2010). Dark Matter Candidates from Particle Physics and Methods of Detection. 48, p. 495. arXiv: 1003.0904 [astro-ph.CO].

Fossati et al. (2016). MUSE sneaks a peek at extreme ram-pressure stripping events - II. The physical properties of the gas tail of ESO137-001. 455, p. 2028. arXiv: 1510.04283 [astro-ph.GA].

Fossati et al. (2018). A Virgo Environmental Survey Tracing Ionised Gas Emission (VESTIGE). II. Constraining the quenching time in the stripped galaxy NGC 4330. 614, A57, A57. arXiv: 1801.09685 [astro-ph.GA].

Friedmann, A. (1922). Über die Krümmung des Raumes. *Zeitschrift fur Physik* 10, p. 377.

Fujita, Yutaka (2004). Pre-Processing of Galaxies before Entering a Cluster. 56, p. 29. arXiv: astro-ph/0311193 [astro-ph].

Gamow, G. (1946). Expanding Universe and the Origin of Elements. *Physical Review* 70, p. 572.

Genel, Shy et al. (2010). The Growth of Dark Matter Halos: Evidence for Significant Smooth Accretion. 719, p. 229. arXiv: 1005.4058 [astro-ph.CO].

Gingold, R. A. and Monaghan, J. J. (1977). Smoothed particle hydrodynamics: theory and application to non-spherical stars. 181, p. 375.

Gnat, Orly and Sternberg, Amiel (2007). Time-dependent Ionization in Radiatively Cooling Gas. 168, p. 213. arXiv: astro-ph/0608181 [astro-ph].

Gnedin, Oleg Y. (2003). Dynamical Evolution of Galaxies in Clusters. 589, p. 752. arXiv: astro-ph/0302498 [astro-ph].

Gómez, Percy L. et al. (2003). Galaxy Star Formation as a Function of Environment in the Early Data Release of the Sloan Digital Sky Survey. 584, p. 210. arXiv: astro-ph/0210193 [astro-ph].

Gronke, Max and Oh, S. Peng (2018). The growth and entrainment of cold gas in a hot wind. 480, p. L111. arXiv: 1806.02728 [astro-ph.GA].

Gunn, James E. and Gott J. Richard, III (1972). On the Infall of Matter Into Clusters of Galaxies and Some Effects on Their Evolution. 176, p. 1.

Guo, Qi et al. (2010). How do galaxies populate dark matter haloes? 404, p. 1111. arXiv: 0909.4305 [astro-ph.CO].

Häring, Nadine and Rix, Hans-Walter (2004). On the Black Hole Mass-Bulge Mass Relation. 604, p. L89. arXiv: astro-ph/0402376 [astro-ph].

Harrison, C. M. (2017). Impact of supermassive black hole growth on star formation. *Nature Astronomy* 1, 0165, p. 0165. arXiv: 1703.06889 [astro-ph.GA].

Hausman, M. A. and Ostriker, J. P. (1978). Galactic cannibalism. III. The morphological evolution of galaxies and clusters. 224, p. 320.

Haynes, M. P. and Giovanelli, R. (1984). Neutral hydrogen in isolated galaxies. IV. Results for the Arecibo sample. 89, p. 758.

Heckman, Timothy M. and Best, Philip N. (2014). The Coevolution of Galaxies and Supermassive Black Holes: Insights from Surveys of the Contemporary Universe. 52, p. 589. arXiv: `1403.4620 [astro-ph.GA]`.

Hernquist (1990). An Analytical Model for Spherical Galaxies and Bulges. 356, p. 359.

Hernquist, Lars (1992). Structure of Merger Remnants. I. Bulgeless Progenitors. 400, p. 460.

Heß, Steffen and Springel, Volker (2012). Gas stripping and mixing in galaxy clusters: a numerical comparison study. 426, p. 3112. arXiv: `1208.0351 [astro-ph.CO]`.

Hockney, R. W. and Eastwood, J. W. (1988). *Computer simulation using particles.*

Hopkins, Philip F. et al. (2008). A Cosmological Framework for the Co-Evolution of Quasars, Supermassive Black Holes, and Elliptical Galaxies. I. Galaxy Mergers and Quasar Activity. 175, p. 356. arXiv: `0706.1243 [astro-ph]`.

Hopkins, Philip F. et al. (2012). Stellar feedback in galaxies and the origin of galaxy-scale winds. 421, p. 3522. arXiv: `1110.4638 [astro-ph.CO]`.

Hubble (1926). Extragalactic nebulae. 64, p. 321.

– (1927). The classification of spiral nebulae. *The Observatory* 50, p. 276.

– (1936). *Realm of the Nebulae.*

Hubble and Humason, Milton L. (1931). The Velocity-Distance Relation among Extra-Galactic Nebulae. 74, p. 43.

Huchra, J. P. and Geller, M. J. (1982). Groups of Galaxies. I. Nearby groups. 257, p. 423.

Ignesti, Alessandro et al. (2022). GASP XXXVIII: The LOFAR-MeerKAT-VLA View on the Nonthermal Side of a Jellyfish Galaxy. 924, 64, p. 64. arXiv: `2110.12719 [astro-ph.GA]`.

Ishibashi, W. and Fabian, A. C. (2012). Active galactic nucleus feedback and triggering of star formation in galaxies. *Monthly Notices of the Royal Astronomical Society* 427, p. 2998. eprint: `https://academic.oup.com/mnras/article-pdf/427/4/2998/2937417/427-4-2998.pdf`.

Jáchym, Pavel et al. (2017). Molecular Gas Dominated 50 kpc Ram Pressure Stripped Tail of the Coma Galaxy D100. 839, 114, p. 114. arXiv: `1704.00824 [astro-ph.GA]`.

Jaffé, Yara L. et al. (2015). BUDHIES II: a phase-space view of H I gas stripping and star formation quenching in cluster galaxies. 448, p. 1715. arXiv: `1501.03819 [astro-ph.GA]`.

Jeans, J. H. (1902). The Stability of a Spherical Nebula. *Philosophical Transactions of the Royal Society of London Series A* 199, p. 1.

Ji, Suoqing et al. (2018). The impact of magnetic fields on thermal instability. 476, p. 852. arXiv: `1710.00822 [astro-ph.GA]`.

Jian, Hung-Yu et al. (2018). First results on the cluster galaxy population from the Subaru Hyper Suprime-Cam survey. I. The role of group or cluster environment in star formation quenching from z = 0.2 to 1.1. 70, S23, S23. arXiv: 1704.06219 [astro-ph.GA].

Johnston, Evelyn J. et al. (2014). The origin of S0s in clusters: evidence from the bulge and disc star formation histories. 441, p. 333. arXiv: 1403.5561 [astro-ph.GA].

Kauffmann, Guinevere et al. (2004). The environmental dependence of the relations between stellar mass, structure, star formation and nuclear activity in galaxies. 353, p. 713. arXiv: astro-ph/0402030 [astro-ph].

Kenney, Jeffrey D. P. et al. (2004). VLA H I Observations of Gas Stripping in the Virgo Cluster Spiral NGC 4522. 127, p. 3361. arXiv: astro-ph/0403103 [astro-ph].

Kennicutt, Jr. (1998). The Global Schmidt Law in Star-forming Galaxies. *The Astrophysical Journal* 498, p. 541.

Kennicutt R. C., Jr. (1983). On the evolution of the spiral galaxies in the Virgo cluster. 88, p. 483.

Kennicutt Robert C., Jr. (1989). The Star Formation Law in Galactic Disks. 344, p. 685.

Kereš, Dušan et al. (2005). How do galaxies get their gas? 363, p. 2. arXiv: astro-ph/0407095 [astro-ph].

Khoperskov, S. et al. (2018). Bar quenching in gas-rich galaxies. 609, A60, A60. arXiv: 1709.03604 [astro-ph.GA].

Klypin, Anatoly A. et al. (2011). Dark Matter Halos in the Standard Cosmological Model: Results from the Bolshoi Simulation. 740, 102, p. 102. arXiv: 1002.3660 [astro-ph.CO].

Komatsu, E. et al. (2011). Seven-year Wilkinson Microwave Anisotropy Probe (WMAP) Observations: Cosmological Interpretation. 192, 18, p. 18. arXiv: 1001.4538 [astro-ph.CO].

Kormendy, John and Ho, Luis C. (2013). Coevolution (Or Not) of Supermassive Black Holes and Host Galaxies. 51, p. 511. arXiv: 1304.7762 [astro-ph.CO].

Larson (1974). Effects of supernovae on the early evolution of galaxies. 169, p. 229.

Larson et al. (1980). The evolution of disk galaxies and the origin of S0 galaxies. 237, p. 692.

Lee, Jaehyun et al. (2020). Dual Effects of Ram Pressure on Star Formation in Multiphase Disk Galaxies with Strong Stellar Feedback. 905, 31, p. 31. arXiv: 2010.11028 [astro-ph.GA].

Li, Zhihui et al. (2020). On the survival of cool clouds in the circumgalactic medium. 492, p. 1841. arXiv: 1909.02632 [astro-ph.GA].

Liddle, Andrew R. and Lyth, David H. (1993). The cold dark matter density perturbation. 231, p. 1. arXiv: astro-ph/9303019 [astro-ph].

Lotz, Marcel et al. (2019). Gone after one orbit: How cluster environments quench galaxies. 488, p. 5370. arXiv: 1810.02382 [astro-ph.GA].

Madau, Piero and Dickinson, Mark (2014). Cosmic Star-Formation History. 52, p. 415. arXiv: 1403.0007 [astro-ph.CO].

Magorrian, John et al. (1998). The Demography of Massive Dark Objects in Galaxy Centers. 115, p. 2285. arXiv: astro-ph/9708072 [astro-ph].

Marinova, Irina and Jogee, Shardha (2007). Characterizing Bars at z ~0 in the Optical and NIR: Implications for the Evolution of Barred Disks with Redshift. 659, p. 1176. arXiv: astro-ph/0608039 [astro-ph].

Markevitch, Maxim and Vikhlinin, Alexey (2007). Shocks and cold fronts in galaxy clusters. 443, p. 1. arXiv: astro-ph/0701821 [astro-ph].

Martig, Marie et al. (2009). Morphological Quenching of Star Formation: Making Early-Type Galaxies Red. 707, p. 250. arXiv: 0905.4669 [astro-ph.CO].

Martin, D. Christopher et al. (2007). The UV-Optical Galaxy Color-Magnitude Diagram. III. Constraints on Evolution from the Blue to the Red Sequence. 173, p. 342. arXiv: astro-ph/0703281 [astro-ph].

Martini, Paul et al. (2009). The Evolution of Active Galactic Nuclei in Clusters of Galaxies to Redshift 1.3. 701, p. 66. arXiv: 0906.1843 [astro-ph.CO].

McCourt, Michael et al. (2015). Magnetized gas clouds can survive acceleration by a hot wind. 449, p. 2. arXiv: 1409.6719 [astro-ph.GA].

McKee and Ostriker (1977). A theory of the interstellar medium: three components regulated by supernova explosions in an inhomogeneous substrate. 218, p. 148.

McKee and Tan, Jonathan C. (2008). The Formation of the First Stars. II. Radiative Feedback Processes and Implications for the Initial Mass Function. 681, p. 771. arXiv: 0711.1377 [astro-ph].

Merritt, D. (1983). Relaxation and tidal stripping in rich clusters of galaxies. I. Evolution of the mass distribution. 264, p. 24.

Mihos, J. Christopher and Hernquist, Lars (1996). Gasdynamics and Starbursts in Major Mergers. 464, p. 641. arXiv: astro-ph/9512099 [astro-ph].

Mihos, J. Christopher et al. (2013). The Extended Optical Disk of M101. 762, 82, p. 82. arXiv: 1211.3095 [astro-ph.CO].

Mo, Houjun et al. (2010). *Galaxy Formation and Evolution.*

Monaghan, J. J. (1992). Smoothed particle hydrodynamics. 30, p. 543.

Moore, Ben et al. (1996). Galaxy harassment and the evolution of clusters of galaxies. 379, p. 613. arXiv: astro-ph/9510034 [astro-ph].

Moore, Ben et al. (1998). Morphological Transformation from Galaxy Harassment. 495, p. 139. arXiv: astro-ph/9701211 [astro-ph].

Moore, Ben et al. (1999a). Dark Matter Substructure within Galactic Halos. 524, p. L19. arXiv: astro-ph/9907411 [astro-ph].

Moore, Ben et al. (1999b). On the survival and destruction of spiral galaxies in clusters. 304, p. 465. arXiv: astro-ph/9811127 [astro-ph].

Moster, Benjamin P. et al. (2013). Galactic star formation and accretion histories from matching galaxies to dark matter haloes. 428, p. 3121. arXiv: 1205.5807 [astro-ph.CO].

Müller, Ancla et al. (2021a). Highly ordered magnetic fields in the tail of the jellyfish galaxy JO206. *Nature Astronomy* 5, p. 159. arXiv: 2009.13287 [astro-ph.GA].

Müller, Ancla et al. (2021b). Two striking head-tail galaxies in the galaxy cluster IIZW108: insights into transition to turbulence, magnetic fields, and particle re-acceleration. 508, p. 5326. arXiv: 2110.03705 [astro-ph.GA].

Murphy, E. J. et al. (2009). Environmental Effects in Clusters: Modified Far-Infrared-Radio Relations within Virgo Cluster Galaxies. 694, p. 1435. arXiv: 0812.2922 [astro-ph].

Murray, Norman et al. (2005). On the Maximum Luminosity of Galaxies and Their Central Black Holes: Feedback from Momentum-driven Winds. 618, p. 569. arXiv: astro-ph/0406070 [astro-ph].

Navarro, Julio F. et al. (1996). The Structure of Cold Dark Matter Halos. 462, p. 563. arXiv: astro-ph/9508025 [astro-ph].

– (1997). A Universal Density Profile from Hierarchical Clustering. 490, p. 493. arXiv: astro-ph/9611107 [astro-ph].

Nelson, Dylan et al. (2013). Moving mesh cosmology: tracing cosmological gas accretion. 429, p. 3353. arXiv: 1301.6753 [astro-ph.CO].

Noeske, K. G. et al. (2007). Star Formation in AEGIS Field Galaxies since z=1.1: The Dominance of Gradually Declining Star Formation, and the Main Sequence of Star-forming Galaxies. 660, p. L43. arXiv: astro-ph/0701924 [astro-ph].

Nulsen, P. E. J. (1982). Transport processes and the stripping of cluster galaxies. 198, p. 1007.

O'Sullivan, E. et al. (2015). Cold gas in group-dominant elliptical galaxies. 573, A111, A111. arXiv: 1408.7106 [astro-ph.GA].

Oemler A., Jr. (1976). The structure of elliptical and cD galaxies. 209, p. 693.

Oemler Augustus, Jr. (1974). The Systematic Properties of Clusters of Galaxies. Photometry of 15 Clusters. 194, p. 1.

Ohkubo, Takuya et al. (2009). Evolution of Very Massive Population III Stars with Mass Accretion from Pre-main Sequence to Collapse. 706, p. 1184. arXiv: 0902.4573 [astro-ph.SR].

Okamoto, Takashi et al. (2010). The properties of satellite galaxies in simulations of galaxy formation. 406, p. 208. arXiv: 0909.0265 [astro-ph.CO].

Pakmor and Springel (2013). Simulations of magnetic fields in isolated disc galaxies. 432, p. 176. arXiv: 1212.1452 [astro-ph.CO].

Pakmor et al. (2011). Magnetohydrodynamics on an unstructured moving grid. 418, p. 1392. arXiv: 1108.1792 [astro-ph.IM].

Pakmor et al. (2016). Improving the convergence properties of the moving-mesh code AREPO. 455, p. 1134. arXiv: 1503.00562 [astro-ph.GA].

Peebles, P. J. E. (1965). The Black-Body Radiation Content of the Universe and the Formation of Galaxies. 142, p. 1317.

Peng et al. (2010). Mass and Environment as Drivers of Galaxy Evolution in SDSS and zCOSMOS and the Origin of the Schechter Function. 721, p. 193. arXiv: 1003.4747 [astro-ph.CO].

Peng et al. (2015). Strangulation as the primary mechanism for shutting down star formation in galaxies. 521, p. 192. arXiv: 1505.03143 [astro-ph.GA].

Penzias, A. A. and Wilson, R. W. (1965). A Measurement of Excess Antenna Temperature at 4080 Mc/s. 142, p. 419.

Pfrommer, Christoph (2022). *The Physics of Galaxy Clusters.*

Pfrommer et al. (2017). Simulating cosmic ray physics on a moving mesh. 465, p. 4500. arXiv: 1604.07399 [astro-ph.GA].

Pfrommer et al. (2022). Simulating radio synchrotron emission in star-forming galaxies: small-scale magnetic dynamo and the origin of the far-infrared-radio correlation. 515, p. 4229. arXiv: 2105.12132 [astro-ph.GA].

Planck Collaboration (2020). Planck 2018 results. VI. Cosmological parameters. 641, A6, A6. arXiv: 1807.06209 [astro-ph.CO].

Planck Collaboration et al. (2014). Planck 2013 results. I. Overview of products and scientific results. 571, A1, A1. arXiv: 1303.5062 [astro-ph.CO].

Planelles, S. et al. (2015). Large-Scale Structure Formation: From the First Non-linear Objects to Massive Galaxy Clusters. 188, p. 93. arXiv: 1404.3956 [astro-ph.CO].

Plummer, H. C. (1911). On the problem of distribution in globular star clusters. 71, p. 460.

Poggianti, Bianca M. et al. (1999). The Star Formation Histories of Galaxies in Distant Clusters. 518, p. 576. arXiv: astro-ph/9901264 [astro-ph].

Poggianti, Bianca M. et al. (2017a). GASP. I. Gas Stripping Phenomena in Galaxies with MUSE. 844, 48, p. 48. arXiv: 1704.05086 [astro-ph.GA].

Poggianti, Bianca M. et al. (2017b). Ram-pressure feeding of supermassive black holes. 548, p. 304. arXiv: 1708.09036 [astro-ph.GA].

Poggianti, Bianca M. et al. (2019a). GASP XIII. Star formation in gas outside galaxies. 482, p. 4466. arXiv: 1811.00823 [astro-ph.GA].

Poggianti, Bianca M. et al. (2019b). GASP XXIII: A Jellyfish Galaxy as an Astrophysical Laboratory of the Baryonic Cycle. 887, 155, p. 155. arXiv: 1910.11622 [astro-ph.GA].

Pontzen, Andrew et al. (2017). How to quench a galaxy. 465, p. 547. arXiv: 1607.02507 [astro-ph.GA].

Powell, Kenneth G. et al. (1999). A Solution-Adaptive Upwind Scheme for Ideal Magnetohydrodynamics. *Journal of Computational Physics* 154, p. 284.

Power, C. et al. (2003). The inner structure of ΛCDM haloes - I. A numerical convergence study. 338, p. 14. arXiv: astro-ph/0201544 [astro-ph].

Price, D. J. and Monaghan, J. J. (2007). An energy-conserving formalism for adaptive gravitational force softening in smoothed particle hydrodynamics and N-body codes. 374, p. 1347. arXiv: astro-ph/0610872 [astro-ph].

Quilis, Vicent et al. (2000). Gone with the Wind: The Origin of S0 Galaxies in Clusters. *Science* 288, p. 1617. arXiv: astro-ph/0006031 [astro-ph].

Ramatsoku, M. et al. (2019). GASP - XVII. H I imaging of the jellyfish galaxy JO206: gas stripping and enhanced star formation. 487, p. 4580. arXiv: 1906.03686 [astro-ph.GA].

Ramos-Martınez, Mariana et al. (2018). MHD simulations of ram pressure stripping of a disc galaxy. 476, p. 3781. arXiv: 1711.01252 [astro-ph.GA].

Randall, S. et al. (2008). Chandra's View of the Ram Pressure Stripped Galaxy M86. 688, p. 208. arXiv: 0806.0866 [astro-ph].

Rees and Ostriker, J. P. (1977). Cooling, dynamics and fragmentation of massive gas clouds: clues to the masses and radii of galaxies and clusters. 179, p. 541.

Renzini, Alvio and Peng (2015). An Objective Definition for the Main Sequence of Star-forming Galaxies. 801, L29, p. L29. arXiv: 1502.01027 [astro-ph.GA].

Riess, Adam G. et al. (1998). Observational Evidence from Supernovae for an Accelerating Universe and a Cosmological Constant. 116, p. 1009. arXiv: astro-ph/9805201 [astro-ph].

Robertson, Brant et al. (2006). A Merger-driven Scenario for Cosmological Disk Galaxy Formation. 645, p. 986. arXiv: astro-ph/0503369 [astro-ph].

Roediger and Brüggen, Marcus (2007). Ram pressure stripping of disc galaxies orbiting in clusters - I. Mass and radius of the remaining gas disc. 380, p. 1399. arXiv: 0707.2698 [astro-ph].

Roediger and Hensler, G. (2008). The role of the Rayleigh-Taylor instability in ram pressure stripped disk galaxies. 483, p. 121. arXiv: 0803.1047 [astro-ph].

Roediger et al. (2006). Wakes of ram-pressure-stripped disc galaxies. 371, p. 609. arXiv: astro-ph/0603565 [astro-ph].

Rubin, Vera C. and Ford W. Kent, Jr. (1970). Rotation of the Andromeda Nebula from a Spectroscopic Survey of Emission Regions. 159, p. 379.

Ruszkowski, M. et al. (2007). Impact of tangled magnetic fields on fossil radio bubbles. 378, p. 662. arXiv: `astro-ph/0703801 [astro-ph]`.

Ruszkowski, M. et al. (2014). Impact of Magnetic Fields on Ram Pressure Stripping in Disk Galaxies. 784, 75, p. 75. arXiv: `1203.1343 [astro-ph.CO]`.

Salim (2014). Green Valley Galaxies. *Serbian Astronomical Journal* 189, p. 1. arXiv: `1501.01963 [astro-ph.GA]`.

Salim et al. (2007). UV Star Formation Rates in the Local Universe. 173, p. 267. arXiv: `0704.3611 [astro-ph]`.

Salpeter, Edwin E. (1955). The Luminosity Function and Stellar Evolution. 121, p. 161.

Sarazin, Craig L. (1986). X-ray emission from clusters of galaxies. *Rev. Mod. Phys.* 58 (1), p. 1.

Sarkar, Prakash et al. (2009). The scale of homogeneity of the galaxy distribution in SDSS DR6. 399, p. L128. arXiv: `0906.3431 [astro-ph.CO]`.

Scannapieco, Evan and Brüggen, Marcus (2008). Subgrid Modeling of AGN-driven Turbulence in Galaxy Clusters. 686, p. 927. arXiv: `0806.3268 [astro-ph]`.

Schawinski, Kevin et al. (2010). Galaxy Zoo: The Fundamentally Different Co-Evolution of Supermassive Black Holes and Their Early- and Late-Type Host Galaxies. 711, p. 284. arXiv: `1001.3141 [astro-ph.CO]`.

Schawinski, Kevin et al. (2014). The green valley is a red herring: Galaxy Zoo reveals two evolutionary pathways towards quenching of star formation in early- and late-type galaxies. 440, p. 889. arXiv: `1402.4814 [astro-ph.GA]`.

Schmidt, Maarten (1959). The Rate of Star Formation. 129, p. 243.

Sérsic, J. L. (1963). Influence of the atmospheric and instrumental dispersion on the brightness distribution in a galaxy. *Boletin de la Asociacion Argentina de Astronomia La Plata Argentina* 6, p. 41.

Silk Rees, Martin J. (1998). Quasars and galaxy formation. 331, p. L1. arXiv: `astro-ph/9801013 [astro-ph]`.

Silverman, J. D. et al. (2008). The Evolution of AGN Host Galaxies: From Blue to Red and the Influence of Large-Scale Structures. 675, p. 1025. arXiv: `0709.3455 [astro-ph]`.

Smethurst, R. J. et al. (2015). Galaxy Zoo: evidence for diverse star formation histories through the green valley. 450, p. 435. arXiv: `1501.05955 [astro-ph.GA]`.

Solway, Michael et al. (2012). Radial migration in galactic thick discs. 422, p. 1363. arXiv: `1202.1418 [astro-ph.GA]`.

Somerville, Rachel S. and Davé, Romeel (2015). Physical Models of Galaxy Formation in a Cosmological Framework. 53, p. 51. arXiv: 1412.2712 [astro-ph.GA].

Somerville, Rachel S. et al. (2008). A semi-analytic model for the co-evolution of galaxies, black holes and active galactic nuclei. *Monthly Notices of the Royal Astronomical Society* 391, p. 481. ISSN: 0035-8711. eprint: https://academic.oup.com/mnras/article-pdf/391/2/481/5764146/mnras0391-0481.pdf.

Sparre, Martin and Springel, Volker (2016). Zooming in on major mergers: dense, starbursting gas in cosmological simulations. 462, p. 2418. arXiv: 1604.08205 [astro-ph.GA].

– (2017). The unorthodox evolution of major merger remnants into star-forming spiral galaxies. 470, p. 3946. arXiv: 1610.03850 [astro-ph.GA].

Sparre, Martin et al. (2015). The star formation main sequence and stellar mass assembly of galaxies in the Illustris simulation. 447, p. 3548. arXiv: 1409.0009 [astro-ph.GA].

Sparre, Martin et al. (2019). The physics of multiphase gas flows: fragmentation of a radiatively cooling gas cloud in a hot wind. 482, p. 5401. arXiv: 1807.07971 [astro-ph.GA].

Sparre, Martin et al. (2020). Interaction of a cold cloud with a hot wind: the regimes of cloud growth and destruction and the impact of magnetic fields. 499, p. 4261. arXiv: 2008.09118 [astro-ph.GA].

Speagle, J. S. et al. (2014). A Highly Consistent Framework for the Evolution of the Star-Forming "Main Sequence" from z ~0-6. 214, 15, p. 15. arXiv: 1405.2041 [astro-ph.GA].

Spergel, D. N. et al. (2007). Three-Year Wilkinson Microwave Anisotropy Probe (WMAP) Observations: Implications for Cosmology. 170, p. 377. arXiv: astro-ph/0603449 [astro-ph].

Springel (2010). E pur si muove: Galilean-invariant cosmological hydrodynamical simulations on a moving mesh. 401, p. 791. arXiv: 0901.4107 [astro-ph.CO].

Springel and Hernquist (2003). Cosmological smoothed particle hydrodynamics simulations: a hybrid multiphase model for star formation. 339, p. 289. arXiv: astro-ph/0206393 [astro-ph].

Springel, Volker (2010). Smoothed Particle Hydrodynamics in Astrophysics. 48, p. 391. arXiv: 1109.2219 [astro-ph.CO].

Springel, Volker and Hernquist, Lars (2005). Formation of a Spiral Galaxy in a Major Merger. 622, p. L9. arXiv: astro-ph/0411379 [astro-ph].

Springel, Volker et al. (2005a). Black Holes in Galaxy Mergers: The Formation of Red Elliptical Galaxies. 620, p. L79. arXiv: astro-ph/0409436 [astro-ph].

Springel, Volker et al. (2005b). Simulations of the formation, evolution and clustering of galaxies and quasars. 435, p. 629. arXiv: astro-ph/0504097 [astro-ph].

Springel and White (1999). Tidal tails in cold dark matter cosmologies. 307, p. 162. arXiv: astro-ph/9807320 [astro-ph].

Springel et al. (2005). Modelling feedback from stars and black holes in galaxy mergers. 361, p. 776. arXiv: astro-ph/0411108 [astro-ph].

Steinhauser, Dominik et al. (2016). Simulations of ram-pressure stripping in galaxy-cluster interactions. 591, A51, A51. arXiv: 1604.05193 [astro-ph.GA].

Steyrleithner, P. et al. (2020). The effect of ram-pressure stripping on dwarf galaxies. 494, p. 1114. arXiv: 2003.09591 [astro-ph.GA].

Strateva, Iskra et al. (2001). Color Separation of Galaxy Types in the Sloan Digital Sky Survey Imaging Data. 122, p. 1861. arXiv: astro-ph/0107201 [astro-ph].

Su, Yuanyuan et al. (2017). Deep Chandra Observations of NGC 1404: Cluster Plasma Physics Revealed by an Infalling Early-type Galaxy. 834, 74, p. 74. arXiv: 1612.00535 [astro-ph.HE].

Suresh, Joshua et al. (2019). Zooming in on accretion - II. Cold circumgalactic gas simulated with a super-Lagrangian refinement scheme. 483, p. 4040. arXiv: 1811.01949 [astro-ph.GA].

Teyssier, R. (2002). Cosmological hydrodynamics with adaptive mesh refinement. A new high resolution code called RAMSES. 385, p. 337. arXiv: astro-ph/0111367 [astro-ph].

Tonnesen, Stephanie (2019). The Journey Counts: The Importance of Including Orbits when Simulating Ram Pressure Stripping. 874, 161, p. 161. arXiv: 1903.08178 [astro-ph.GA].

Tonnesen, Stephanie and Bryan, Greg L. (2009). Gas Stripping in Simulated Galaxies with a Multiphase Interstellar Medium. 694, p. 789. arXiv: 0901.2115 [astro-ph.GA].

– (2010). The Tail of the Stripped Gas that Cooled: H I, Hα, and X-ray Observational Signatures of Ram Pressure Stripping. 709, p. 1203. arXiv: 0909.3097 [astro-ph.CO].

– (2012). Star formation in ram pressure stripped galactic tails. 422, p. 1609. arXiv: 1203.0308 [astro-ph.CO].

Tonnesen, Stephanie and Stone, James (2014). The Ties that Bind? Galactic Magnetic Fields and Ram Pressure Stripping. 795, 148, p. 148. arXiv: 1408.4521 [astro-ph.GA].

Toomre (1972). Galactic Bridges and Tails. 178, p. 623.

– (1977). "Mergers and Some Consequences". *Evolution of Galaxies and Stellar Populations*. Ed. by Beatrice M. Tinsley and D. Campbell Larson Richard B. Gehret, p. 401.

Toro, E.F. (2009). *Riemann Solvers and Numerical Methods for Fluid Dynamics: A Practical Introduction*. Springer. ISBN: 9783540252023.

Torrey, Paul et al. (2012). Moving-mesh cosmology: properties of gas discs. 427, p. 2224. arXiv: 1110.5635 [astro-ph.CO].

Tumlinson, Jason et al. (2017). The Circumgalactic Medium. 55, p. 389. arXiv: 1709.09180 [astro-ph.GA].

Vijayaraghavan, Rukmani and Ricker, Paul M. (2017). The Co-evolution of a Magnetized Intracluster Medium and Hot Galactic Coronae: Magnetic Field Amplification and Turbulence Generation. 841, 38, p. 38. arXiv: 1702.06138 [astro-ph.HE].

Vogelsberger, Mark et al. (2012). Moving mesh cosmology: numerical techniques and global statistics. 425, p. 3024. arXiv: 1109.1281 [astro-ph.CO].

Vogelsberger, Mark et al. (2013). A model for cosmological simulations of galaxy formation physics. 436, p. 3031. arXiv: 1305.2913 [astro-ph.CO].

Voit, G. Mark (2005). Tracing cosmic evolution with clusters of galaxies. *Reviews of Modern Physics* 77, p. 207. arXiv: astro-ph/0410173 [astro-ph].

Vollmer, B. et al. (1999). Kinematics of the anemic cluster galaxy NGC 4548. Is stripping still active? 349, p. 411. arXiv: astro-ph/9907351 [astro-ph].

Vollmer, B. et al. (2001). Ram Pressure Stripping and Galaxy Orbits: The Case of the Virgo Cluster. 561, p. 708. arXiv: astro-ph/0107237 [astro-ph].

Vulcani, Benedetta et al. (2020). GASP XXIV. The History of Abruptly Quenched Galaxies in Clusters. 892, 146, p. 146. arXiv: 2003.02274 [astro-ph.GA].

Wang, J. et al. (2011). Assembly history and structure of galactic cold dark matter haloes. 413, p. 1373. arXiv: 1008.5114 [astro-ph.CO].

Weinberger, Rainer et al. (2020). The AREPO Public Code Release. 248, 32, p. 32. arXiv: 1909.04667 [astro-ph.IM].

White (1984). Angular momentum growth in protogalaxies. 286, p. 38.

White and Rees (1978). Core condensation in heavy halos: a two-stage theory for galaxy formation and clustering. 183, p. 341.

Wiersma, Robert P. C. et al. (2009). The effect of photoionization on the cooling rates of enriched, astrophysical plasmas. 393, p. 99. arXiv: 0807.3748 [astro-ph].

Wise, John H. (2012). First Light: A Brief Review. *arXiv e-prints*, arXiv:1201.4820, arXiv:1201.4820. arXiv: 1201.4820 [astro-ph.CO].

Yagi, Masafumi et al. (2010). A DOZEN NEW GALAXIES CAUGHT IN THE ACT: GAS STRIPPING AND EXTENDED EMISSION LINE REGIONS IN THE COMA CLUSTER. *The Astronomical Journal* 140, p. 1814.

Yamagami, Takahiro and Fujita, Yutaka (2011). Star Formation in the Cometary Tails Associated with Cluster Galaxies. *Publications of the Astronomical Society of Japan* 63, p. 1165. ISSN: 0004-6264. eprint: https://academic.oup.com/pasj/article-pdf/63/6/1165/6115938/pasj63-1165.pdf.

Yoshida, Michitoshi et al. (2002). Discovery of a Very Extended Emission-Line Region around the Seyfert 2 Galaxy NGC 4388. 567, p. 118. arXiv: astro-ph/0110473 [astro-ph].

Zel'dovich, Ya. B. (1970). Gravitational instability: An approximate theory for large density perturbations. 5, p. 84.

Zwicky, F. (1937). On the Masses of Nebulae and of Clusters of Nebulae. 86, p. 217.

Appendix A

Appendix Chapter

A.1 Resolution test

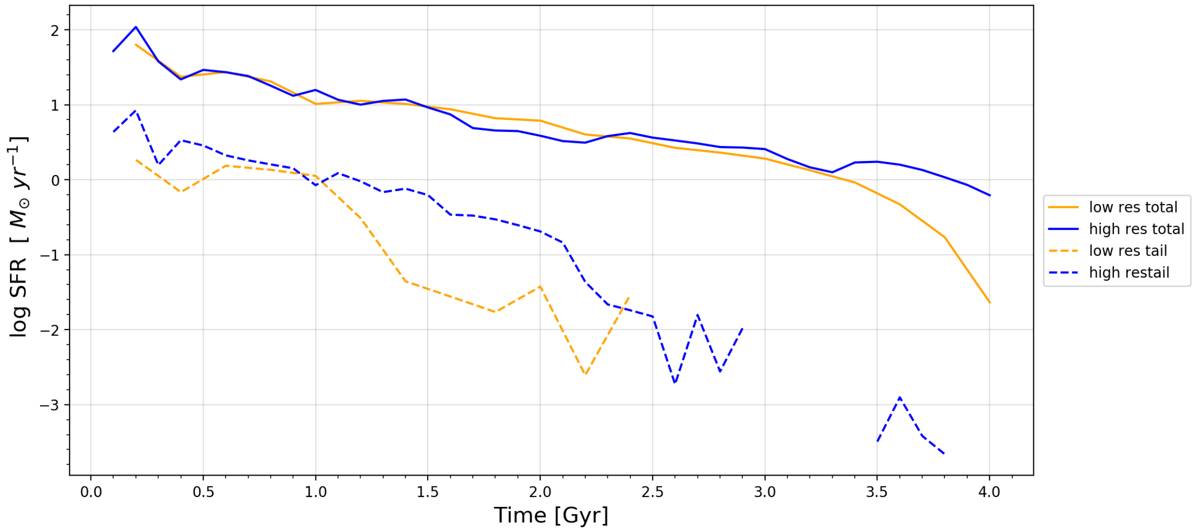

Figure A.1: The star formation rate as a function of resolution for the MHD run. The compared low-resolution accounts for nearly 17 times higher mass per gas particle.

Table 2.1, shows the adopted initial parameters which result in $3.15 \times 10^5 \mathrm{M}_\odot$ per simulated gas particle. Here we perform a resolution test of the SFR evolution during the MHD simulation, comparing our high-resolution run with a simulation counterpart with 17 times higher per particle, i.e $5.30 \times 10^6 \mathrm{M}_\odot$. The global SFR of the jellyfish reveals nearly identical until 3.5 Gyr, denoting the importance of high-resolution simulation in order to capture small-scale phenomena. This becomes even more evident in the tail comparison, as the generalisation that emerged from the low-resolution run is not able to account for the survival scheme of the isolated stripped clouds that essentially contributes to the tail's SFR. Furthermore, the smooth decline of the global SFR, implies that small-scale feedback is not captured, in comparison to the oscillating profile of the high-resolution.

A.2 Supplamentary FoF

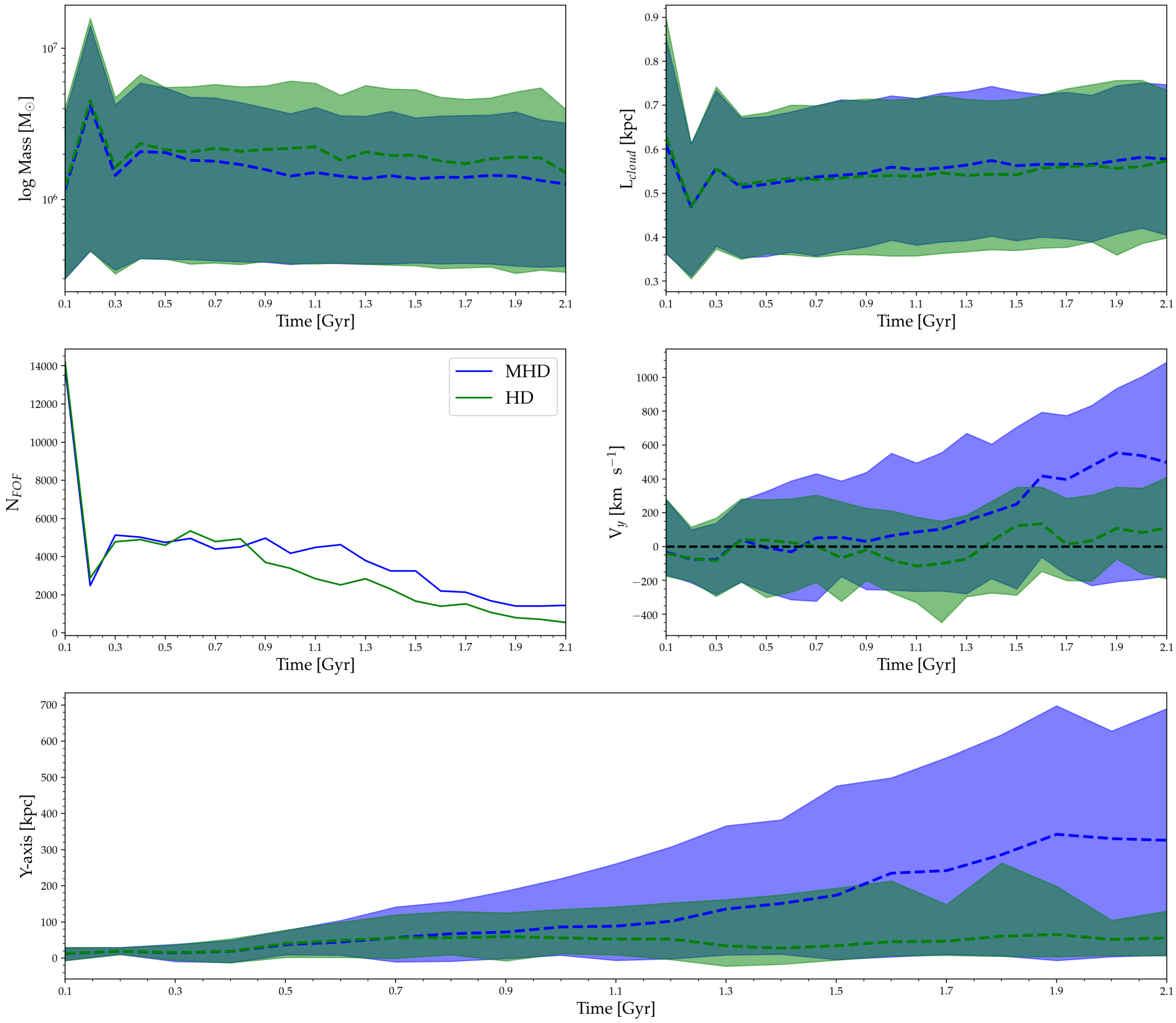

Figure A.2: FoF analysis for linking length $\ell_{\text{link}} = 0.6$

For completeness, in this section, we include the resulting ISM cloud morphology in the tail for different linking lengths. While larger values imply a larger group of ISM gas, the general characteristics regarding the survival scheme of MHD clouds remain the same. The presented figures employed $\ell_{\text{link}} = 0.6$ and $\ell_{\text{link}} = 2.0$.

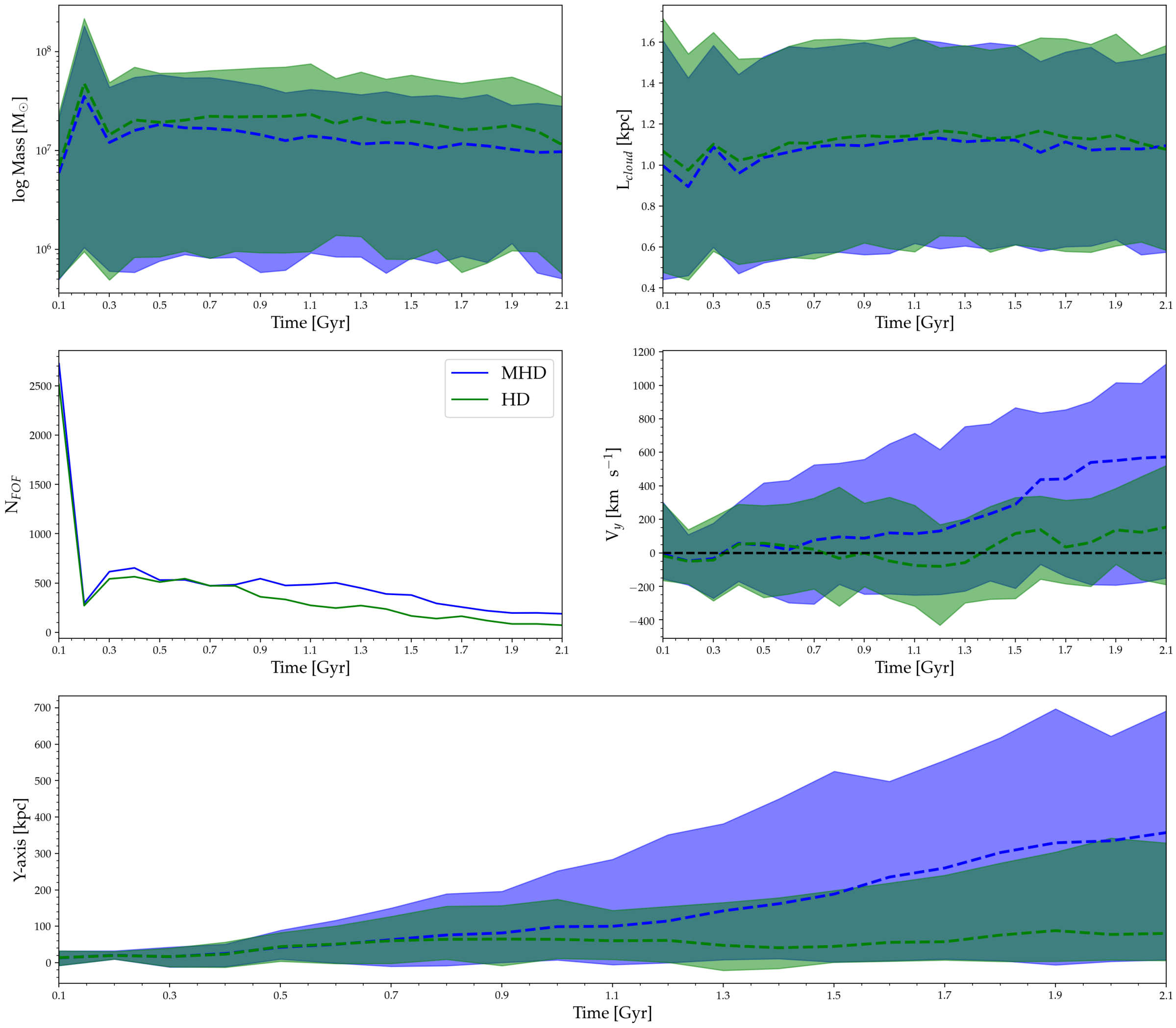

Figure A.3: FoF analysis for linking length $\ell_{\text{link}} = 2.0$